BUNDESREPUBLIK
DEUTSCHLAND

Bundesanstalt für
Geowissenschaften
und Rohstoffe (BGR)

Hannover

PEOPLE'S REPUBLIC
OF BANGLADESH

Geological Survey
of Bangladesh (GSB)

Dhaka

Geo-Information for Urban Planning and Adaptation to Climate Change (GPAC)

Remote Sensing Information for Urban Planning of Faridpur Town and Surroundings

Lukas Wimmer
Nicolas Wagener
Remote Sensing Working Group BGR

Hannover, March 2021

Remote Sensing Information for Urban Planning of Faridpur Town and Surroundings

Authors:	Lukas Wimmer (BGR), Chapter 2.1-2.3 Nicolas Wagener (BGR), Chapter 1, Chapter 2.4

Commissioned by:	Federal Ministry for Economic Cooperation and Development (Bundesministerium für wirtschaftliche Zusammenarbeit und Entwicklung, BMZ)
Project:	Geo-Information for Urban Planning and Adaptation to Climate Change (GPAC)
Project Number:	2016.2062.4
BGR Number:	05-2394
ELVIS Number:	B80136-01_06 05-2394 TZ Bangladesch-III
Project Partner:	Geological Survey of Bangladesh (GSB)

Pages:	114
Place and date of issuance:	Hannover, March 2021

To be cited as:

Wimmer, L. and Wagener, N. (2021): Remote Sensing Information for Urban Planning of Faridpur Town and Surroundings, BGR Project Number: 05-2394.

Table of Contents

List of Figures

Annexure A

List of Tables

List of Abbreviations

ASF	Alaska Satellite Facility
BBD	Bodenbewegungsdienst Deutschland (German Ground Motion Service)
BGR	Bundesanstalt für Geowissenschaften und Rohstoffe (Federal Institute for Geosciences and Natural Resources)
BWDB	Bangladesh Water Development Board
dB	Decibel (unit)
DEM	Digital Elevation Model
DOS	Dark Object Subtraction
ESA	European Space Agency
GNSS	Global Navigation Satellite System
GPAC	Geo-Information for Urban Planning and Adaptation to Climate Change
GPS	Global Positioning System
GSB	Geological Survey of Bangladesh
InSAR	Interferometric Synthetic Aperture Radar
Landsat MSS	Landsat Multispectral Scanner System
Landsat OLI	Landsat Operational Land Imager
Landsat TM	Landsat Thematic Mapper
LEDAPS	Landsat Ecosystem Disturbance Adaptive Processing System
NASA	National Aeronautics and Space Administration
NIR	Near Infrared
NDWI	Normalized Difference Water Index
PSI	Persistent Scatterer Interferometry
RADAR	Radio Detection and Ranging
SAR	Synthetic Aperture Radar
SBAS	Small Baseline Subset
SRTM	Shuttle Radar Topography Mission
SWIR	Shortwave Infrared
TIR	Thermal Infrared
UAV	Unmanned aerial vehicle
USGS	United States Geological Survey

1 Introduction to Remote Sensing

Remote sensing has been variously defined, but basically is the science that describes the collection of physical information, interpretation and extraction of information acquired over an object or area of interest without having physical contact, by the use of remote sensing instruments. The term information refers to a wide range of observable quantities, such as reflected solar radiation across the electromagnetic spectrum and emitted thermal radiation measured from handheld, unmanned aerial vehicle (UAV), airborne or spaceborne imaging sensors and received back-scattered microwave radiation equipment. Availability and effective exploitation of such data has facilitated advances in many applied fields (CHAMBELL, 1996; USTIN, 2004)

The availability and capacity of remote sensing data is comprehensive and huge, therefore the application of remote sensing data to identify and monitor land surfaces and environmental conditions has expanded enormously and remotely sensed data are an essential tool in natural resource management. Climatic changes, desertification processes, forest fires, glaciers melting, water pollution, land cover and vegetation status can be observed thanks to remote sensors onboard of aircraft or satellites orbiting around the earth. Remote sensors onboard of aircraft and satellites allow for a synoptic view of the earth surface at different wavelengths of the electromagnetic radiation at the same time (multi-spectral, -frequency), with (high-) frequent time interval and scale (multi-resolution).

Sensors can be divided into two groups: Passive sensors depend on an external source of energy, usually the sun. Sun radiation is reflected and emitted from the earth surface and collected by a wide variety of optical sensors. Active sensors have their own source of energy. These sensors send out a signal and measure the amount reflected back, and do not depend upon varying illumination conditions (PRASAD ET AL., 2011) (see Fig. 1).

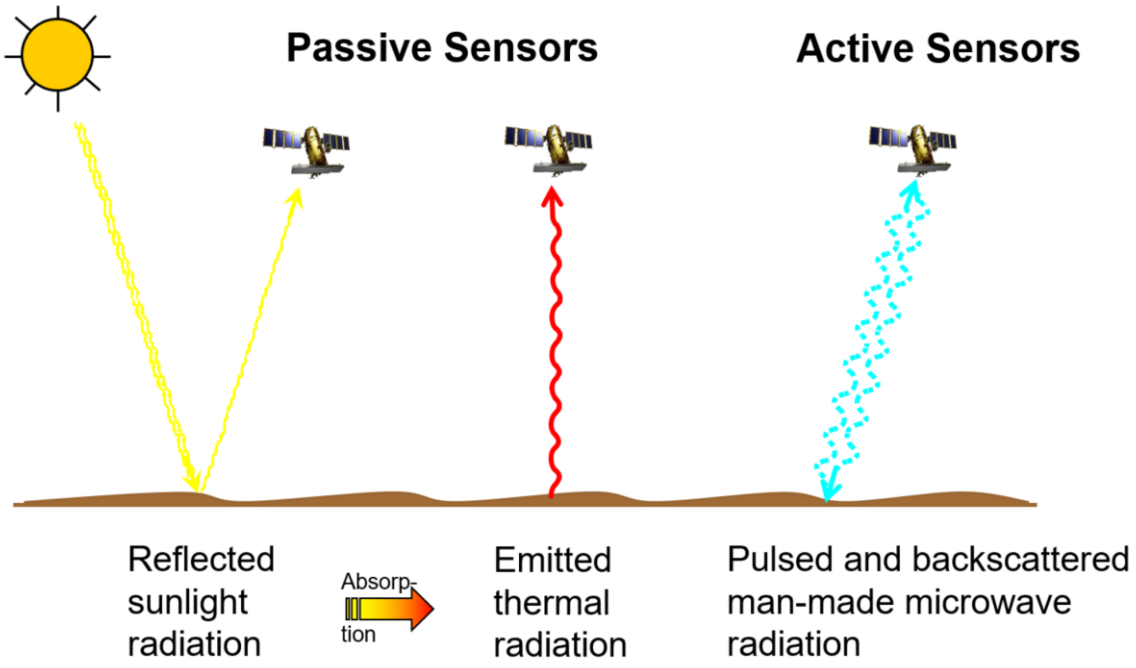

Figure 1: *Passive and active sensors (Source: BGR).*

1.1 Fundamentals of Optical Remote Sensing

Optical remote sensing involves acquisition and analysis of optical data, based on solar illumination and the detection of electromagnetic radiation reflected from targets on the ground. Optical Remote Sensing deals with those part of electromagnetic spectrum characterized by the wavelengths from the visible (from 0.4 µm) to the near infrared (NIR) and short wave infrared (SWIR) up to thermal infrared (TIR, 15 µm), collecting radiation reflected and emitted from the observed surfaces (see Fig. 1).

Optical remote sensing is a passive technique for earth observation, which is exposed to a strong interaction of the electromagnetic radiation within the atmosphere at its operating frequencies and to the presence of clouds. Both factors constitute important limitations on the potential observation of the earth's surface.

Analysis is based on the spectral differences of materials, as materials reflect and absorb differently at different wavelengths, resulting in a specific and unique "spectral footprint". Thus, the targets can be differentiated by their spectral reflectance signatures in the remotely sensed images (SABINS, 1996; RENCZ, 1999).

Optical remote sensing systems are classified depending mainly on the number of spectral bands used in the imaging process. Advances in imaging hardware enabled availability of high spatial, spectral and temporal resolution (PRASAD ET AL., 2011).

A wide range of applications is still based on multispectral imaging systems e.g. Sentinel-2, Landsat-OLI, even so hyperspectral sensors show rapid development on all platforms from UAV to spaceborne carriers.

1.2 Fundamentals of RADAR Remote Sensing

RADAR is an acronym for *RA*dio *D*etection *A*nd *R*anging and describes an object-detection and active imaging system using radio waves (see Fig. 1). The electromagnetic waves used for imaging radars have wavelengths in the order of several centimeters up to roughly one meter. Since earth's atmosphere has a high penetrability in this part of the electromagnetic spectrum, radar-imaging systems are highly independent from weather conditions in the atmosphere.

The accuracy of an imaging radar is defined by two measures: the resolution along the line-of-sight (range resolution) and the resolution along the flight path of the carrier platform (azimuth resolution). The azimuth resolution depends on the antenna aperture: the larger the distance to the area of interest, the larger the antenna must be. For space-borne missions this leads to unrealistic demands on the size of the antenna mounted on the satellite (WOODHOUSE, 2006). To overcome this obstacle, Synthetic Aperture Radar (SAR) exploits the Doppler Effect to synthesize a larger virtual antenna through the combination of several return signals (echoes).

The signal received at the sensor has a frequency variation induced as a result of the platform motion. This effect is known as Doppler shift, a well-known phenomenon in physics. Since the resolution depends on the time, a particular object on the ground is illuminated by the radar beam, making use of the Doppler shift to combine several backscattered echoes effectively results in increasing the duration of irradiation. As this is in effect equal to increasing the antenna aperture size of which the illumination time is a direct function, the term Synthetic Aperture Radar (SAR) is used to describe such an imaging system (RICHARDS, 2009).

SAR sensors are usually mounted on an airborne or space-borne platform and have a side-looking imaging geometry. While the carrier platform moves forward, the SAR system continuously emits and receives electromagnetic pulses. The emitted radiation interacts with objects on the surface that will then backscatter a portion of the signal to the sensor. How big that portion will be, depends on the physical and electrical properties of the objects (FORNANO & PASCAZIO, 2014). At the sensor, both amplitude and phase of the backscattered signal are received (MOREIRA ET AL., 2013).

While the amplitude is related to the object properties (material, roughness, dielectric properties, etc.), the phase is a function of the sensor-target distance.

Synthetic aperture radar (SAR) remote sensing is used today in a wide range of applications and offers a number of complementary and additional capabilities with regard to optical remote sensing. For instance, it can be used to acquire images at night and almost weather independent, to determine soil moisture, biomass or to measure terrain deformations. The ranging capabilities of SAR are used in various ways. Radar interferometry (InSAR) is one such application and allows the estimation of ground deformation and / or topography from (at least) two SAR acquisitions making use of the phase information contained in both images. Multi-temporal InSAR approaches such as Persistent Scatterer Interferometry (PSI) allow the precise estimation (with millimeter accuracy) of surface deformation for specific point targets over long time periods.

2 Products

2.1 Land-use Map

The fast growing population and the trend to move to urban areas leads to a dynamic change in land use. New urban areas are developed by filling agricultural land with river sand to make the building ground more resilient to flooding (see Fig. 2).

The overall goal of this analysis is the comprehensive mapping of the 2019 land-use in Faridpur to derive information on existing and newly established filled areas. The resulting maps will be used in further analyses together with a geomorphological map as a basis for the regionalization of drilling points. Freely available optical satellite data and a supervised classification method allow for the mapping of the land-use.

Figure 2: *Filling of agricultural land with river sand in Faridpur. Photo: L. Wimmer, 11/2019.*

Land-use maps using the classes “Water”, “Bare Soil”, “Urban”, “Rural Settlements” and “Agriculture” are provided for October 2019. An overview map shows the land-use of the study area as well as the surrounding rural areas (Fig. A2). A map, focusing on the study area presents the land-use within the city of Faridpur (Fig. A3).

The main focus of this analysis is the distribution of filled and non-filled areas from the land-use map by reclassification of the five above-mentioned classes. A third map presents these areas within the study area of Faridpur (Fig. A4).

To process the land-use maps, a supervised classification method based on interactively selected training areas is used. These areas are interactively chosen from the original satellite image and represent the spectral properties of a certain land-use class. The supervised classification classifies the satellite image by comparing all the image values with the selected training areas.

Data

The land use classification is based on a cloud-free image from the Copernicus Sentinel-2 mission for the period of the Bangladesh dry season between October and April and the transition times before and after it. To be able to receive results on the most recent land-use and in order to map water areas comprehensively, a satellite image from the early dry season 2019/2020 is required. Different atmospheric conditions during the sensing times of the images can result in different image features of the same ground objects. Therefore, atmospheric corrected images are mandatory, to allow comparison with future land use maps based on Sentinel-2 data. An atmospheric correction eliminates the atmospheric effects in an image and results in a surface reflectance image that characterizes the spectral surface properties. The atmospherically corrected image, showing the overview area cloud-free, from the 14. October 2019 is used for further processing (see Annexure C: Data).

As input for the land use mapping, all bands with the resolution of 10m and 20m of the image are used (Tab. 1). This selection enables the classification method to accurately characterize the land-use classes by using all available spectral properties of the ground objects.

Table 1: *Overview of the Copernicus Sentinel-2 satellite image used for the classification. Blue color represents the spectral band subset used in the analysis.*

Sensing Date	Bands		Wavelengths	Spatial Resolution
22.09.2019	1	Coastal Aerosol	417nm – 471nm	60m
	2	Blue	399nm – 595nm	10m
	3	Green	515nm – 605 nm	10m
	4	Red	627nm – 703nm	10m
	5	Near Infrared	685nm – 723nm	20m
	6		722nm – 758nm	20m
	7		754nm – 810nm	20m
	8		690nm – 980nm	20m
	8A		832nm – 898nm	20m
	9	Water Vapor	919nm – 971nm	60m
	10	Cirrus	1299nm – 1449nm	60m
	11	Shortwave Infrared	1471nm – 1757nm	20m
	12		1960nm – 2444nm	20m

Methods

The workflow of the classification is visualized in Fig. 3.

Preprocessing

To prepare the image for the classification, a spatial subset and a spectral subset are created. The spatial subset shows an overview of the study area of Faridpur as well as the surrounding rural areas (Fig. A1). The spectral subset includes the above-mentioned (Tab. 1) Sentinel-2 bands (Band 2, 3, 4, 5, 6, 7, 8, 8A, 11, 12). Subsequent, all image bands with 20m resolution are resampled to a 10m spatial resolution to keep the information of the higher resolution 10m bands.

Classes and Training Areas

The purpose of the land-use classification is to derive information on urban settlement structures. Accordingly, the two classes “Urban" and "Rural Settlements" are used for the description of these structures. “Agriculture" and "Bare Soil" are chosen to describe the undeveloped areas in general. Water areas are represented by the class "Water".

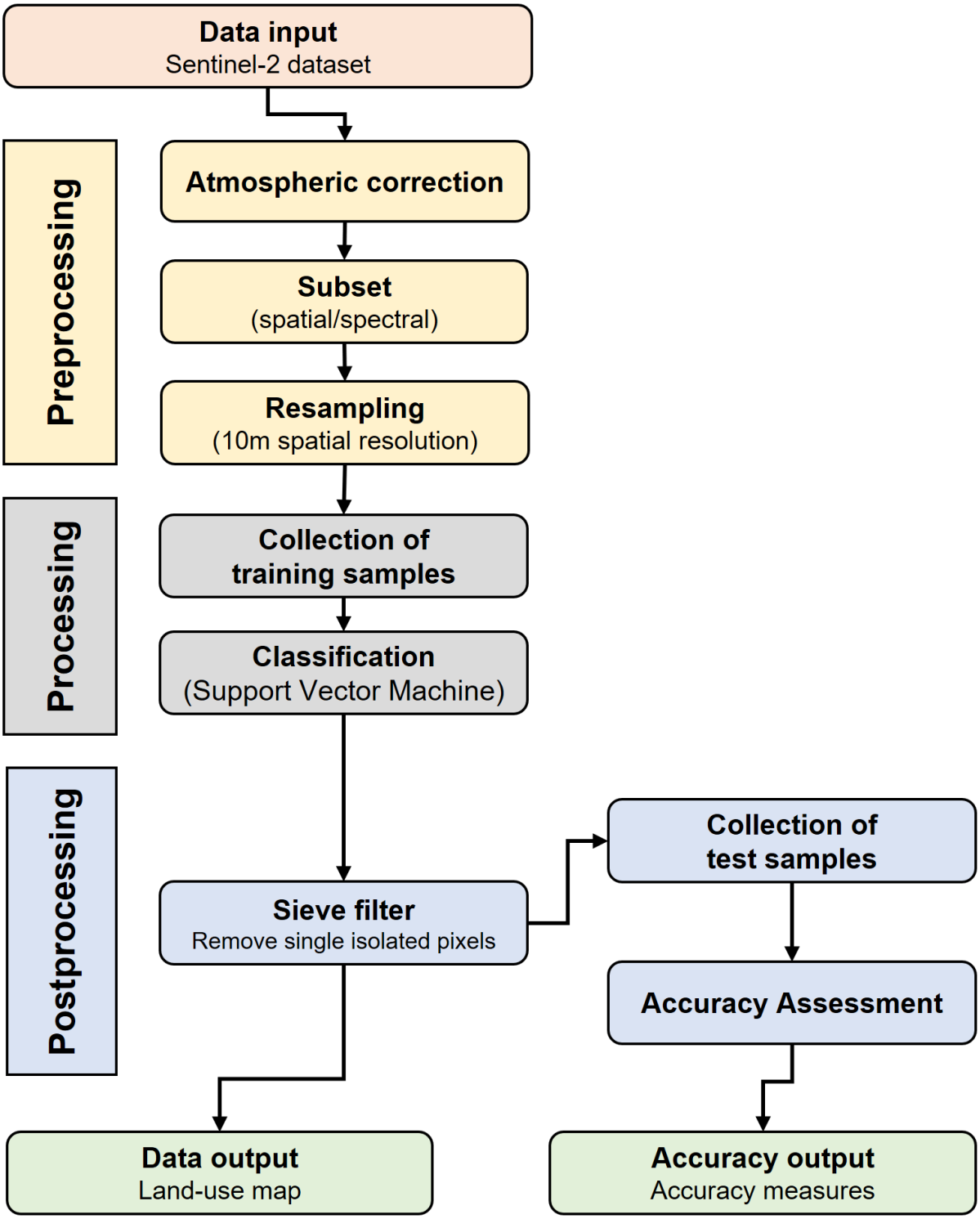

Figure 3: *Workflows of the Land-use classification.*

These classes are based on the CORINE Landcover (CLC) program (EUROPEAN ENVIRONMENT AGENCY, 2019). CORINE Landcover is a program of the European Commission to standardize the most important forms of land cover for environmental policy development. The standardized classes are based on biophysical characteristics of the Earth's surface (EUROPEAN ENVIRONMENT AGENCY, 2017).

"Water" includes all open water bodies, such as river, canals, channels, lakes and ponds. "Bare Soil" includes all surfaces of bright bare soil, such as riverbanks, pointbars and filled areas for urban development. "Urban" includes residential and industrial buildings without tree cover. Furthermore, it includes streets, railway lines and sealed surfaces. "Rural Settlements" include the city suburbs and rural villages that have tree coverage. "Agriculture" are all areas of farmland, such as cropland (rice, vegetables, etc.) or pasture land (for cattle, goats, etc.).

Training areas for all classes are selected from the Sentinel-2 dataset (see Tab. 2). To receive an acceptable classification result, the training areas must be both representative and complete for their land-use classes (LILLESAND ET AL., 2015).

All land-use classes have non-uniform spectral characteristics in common. For example, in the "Urban" class, the spectral characteristics of tin shacks and high-rise buildings differ. The "Agriculture" class includes spectral characteristics of different crops and in the "Water" class, different water qualities also differ spectrally. Different soil types in the "Bare Soil" class also have different spectral characteristics. The "Rural Settlements" class contains areas with different tree species, which result in different spectral characteristics.

The training areas of the land-use classes are required to represent these different spectral characteristics. The number of training areas therefore depends on the spectral variability within a land-use class (see Tab. 2).

The training areas are dispersed throughout the Sentinel-2 dataset to increase the representation of all variations in the land-use classes (LILLESAND ET AL., 2015).

Table 2: *Overview of the number of training areas per class.*

Class	Number of Training Areas
Agriculture	20
Bare Soil	10
Rural Settlements	15
Urban	15
Water	20

To show the spectral variabilities of the individual classes, the spectral profiles of the classes are shown in Fig. 4. Each curve represents the averaged spectral signatures of all training areas per class, based on the Sentinel-2 data set of 14.10.2019. Fig. 4 shows the spectral separability of the classes over the whole band range (see Tab. 1).

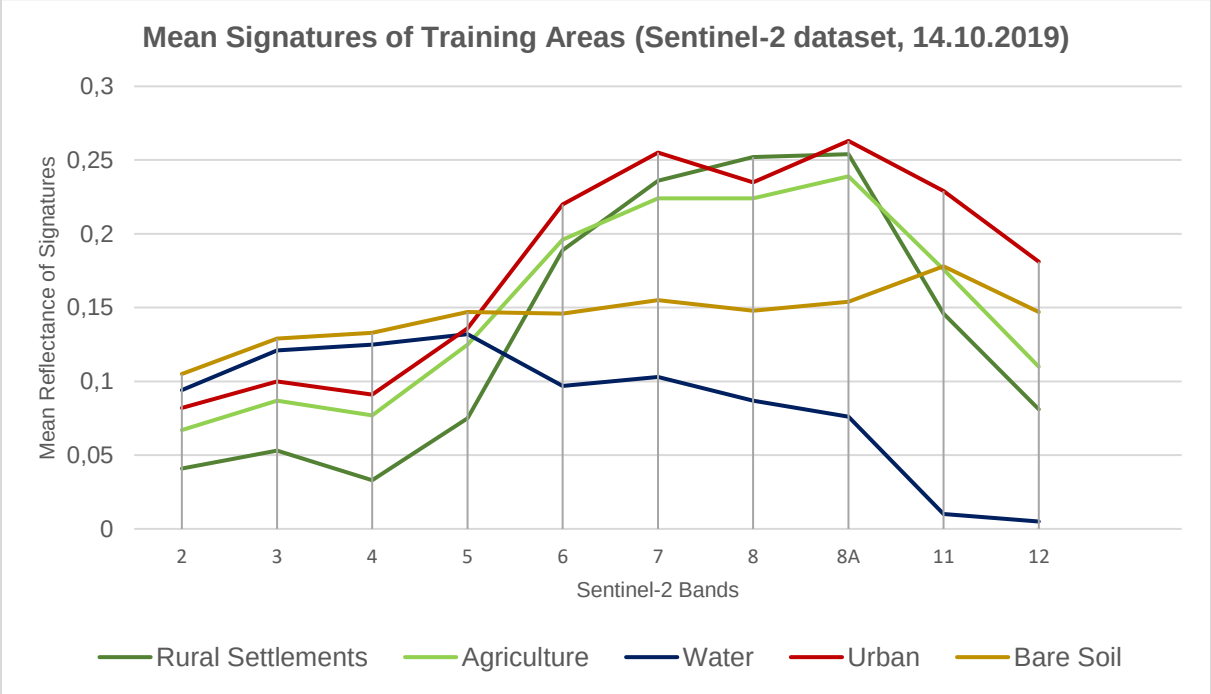

Figure 4: *Mean signatures of the merged training areas.*

The spectral curves of the classes “Agriculture” and “Rural Settlements” have similar spectral signatures. The reason for these similarities is that the class “Rural Settlements” is dominated by tree coverage and therefore represents a strong vegetation signal.

Both classes show vegetation-typical characteristics, such as the "red edge" (a significant increase of reflection in the near infrared bands 5 and 6 compared to the visible bands 2 to 4). The main differences are a higher reflectance in the class “Agriculture” in band 2 to 5 and a higher reflectance of the class “Rural Settlements” in bands 7 to 8A.

The spectral signature of “Water” shows higher reflection values around band 7 and 8 leading to the interpretation that the water class/signature contains impurities, such as sediments. Pure water would have zero reflectance in these longer wavelengths.

The spectral curve of the class “Bare Soil” shows a relatively continuous increase. The shape of the spectral curve of the class “Urban” shows similarities to the class “Agriculture”. Due to the two peaks (band 7 and 8A), interrupted by a lower reflectance (band 8) and the different intensities, the spectral curve nevertheless differs from the curve of the "Agriculture" class.

Classification

To perform the supervised classification, the Support Vector Machine (SVM) classifier is selected, a method based on statistical learning theory. Support Vector Machines are supervised learning models with associated learning algorithms that analyze data used for classification.

The classifier looks at spectral boundaries between individual classes in the multidimensional feature space. It aims to find an optimal margin (known as “hyperplane”) to separate the classes. The data values that constrain the width of the margin are known as “support vectors” (JONES & VAUGHAN, 2010).

In its simplest form, a SVM separates two classes (a binary classifier). Nevertheless, a classification with multiple classes is possible. Based on the training areas, several binary classifiers are calculated which separate the properties of each class from those of every other class (known as “one-versus-one” approach). The number of binary classifiers depends on the number of classes to be separated:

$$n_{classifier} = \frac{n_{class} * (n_{class} - 1)}{2}$$

The variable $n_{classifier}$ represents the number of classifiers; the variable n_{class} represents the number of classes.

Therefore, the properties of the five classes of this investigation are separated using 10 binary classifiers (Tab. 3 shows an example of possible connections of classes), as a result the classes are differentiated spectrally. Each classifier designates a class name to every pixel, the most frequent class name assigns the pixel to the final class (RICHARDS, 2013).

Table 3: *The table shows all possible connections of classes (cf. RICHARDS, 2013).*

Number of binary classifiers	Class name 1	Class name 2
1	Agriculture	Bare Soil
2	Agriculture	Rural Settlements
3	Agriculture	Urban
4	Agriculture	Water
5	Bare Soil	Rural Settlements
6	Bare Soil	Urban
7	Bare Soil	Water
8	Rural Settlements	Urban
9	Rural Settlements	Water
10	Urban	Water

Post-Processing

The same object feature may be classified in different classes due to spectral variabilities. The classification result might show single isolated pixels of one class in the area of another class (LILLESAND ET AL., 2015).

To remove the single isolated pixels in the classification image, a sieve filter is applied. This filter replaces all pixel patches that are smaller than twelve pixels by the value of the surrounding neighbor class. A pixel patch is a group of pixels that share their sides or have connected angles. The final classification result is shown in Fig. A2 and A3.

Calculation of filled and non-filled areas

Based on the knowledge of the GSB colleagues and the experience gained during fieldwork, all urbanized areas and settlement structures in Faridpur are developed on filled areas. Therefore, those areas are considered as filled areas, the classes “Urban” and “Rural Settlements” are reclassified to “Filled” and the classes “Water”, “Bare Soil” and “Agriculture” are reclassified to “Non-filled” (see Fig. A4).

Accuracy Assessment

During the accuracy assessment, randomly distributed test samples are used to compare the classification result with an independent high-resolution reference dataset. As a high-resolution reference dataset, free accessible Google Earth satellite images are used. Thus, details for a more precise interpretation of the actual land use become visible and the classification result can be assessed visually without having the necessity to collect ground truth information during fieldwork.

LILLESAND ET AL. (2015) recommends using at least 50 test samples per class for accuracy assessment. Following this recommendation, 250 test samples are randomly distributed in the image, using 50 samples for each class (Tab. 4).

Table 4: *Accuracy Assessment, Sentinel-2 dataset (14.10.2019).*

Sentinel-2, 14.10.2019		Reference						
		Agriculture	Bare Soil	Rural Settlements	Urban	Water	Row Total	**User's Accuracy (%)**
Classification	Agriculture	44	0	5	1	0	50	88.0
	Bare Soil	2	38	0	0	10	50	76.0
	Rural Settlements	2	1	47	0	0	50	94.0
	Urban	1	15	4	28	2	50	56.0
	Water	3	0	2	0	47	50	94.0
	Column Total	52	54	56	29	59	250	
	Producer's Accuracy (%)	84.61	70.37	89.92	96.55	79.66		
	Cohen's Kappa per Class	0.75	0.75	0.92	0.54	0.91		
	Overall Accuracy (%)	**81.6**						
	Overall Kappa	**0.83**						

Since the images from Google Earth represent a compilation of different points in time, the Sentinel-2 dataset is used as an auxiliary dataset. Both data sets were acquired at different stages of flooding. Therefore, the visual impression of the Sentinel-2 dataset is given priority over the data from Google Earth when assigning water areas. Based on these datasets, land-use classes are interactively assigned to the test sample classes. Following this, the test areas are compared with the classification results to receive the accuracy measures (Tab. 4).

The overall accuracy of the classification is 81.6 %. The Kappa coefficient, a measure for the agreement between classification result and reference shows a good result of 0.83. The User's Accuracy shows how reliable the classified pixels represent actual land use, while Producer's Accuracy shows how well an object class has been correctly classified. In addition, the Kappa coefficients of each class are displayed in order to individually evaluate the reliability of the classification result.
The “Water” and the “Rural Settlements” classes are the most reliably classified with a User’s Accuracy of 94.0 %. This is reflected in the high Kappa coefficients of 0.92 for “Rural Settlements” and 0.91 for “Water”.
The “Agriculture” (88.0 %) and the “Bare Soil” (76.0 %) also show a high User’s Accuracy, compared to the class “Urban” with the lowest accuracy of 56.0 %. This is also visible in the Kappa coefficients, so that the agreement between the classification result and the reference data is 0.75 (“Agriculture” and “Bare Soil”) and 0.54 (“Urban”).

The reason for lower accuracy values may be related to different circumstances:
For example, the spectral signature of the class “Agriculture” shows similarities to the spectral signature of the class “Rural Settlements” (Fig. 4). Therefore, agricultural areas that have spectral characteristics near to “Rural Settlements” (e.g. vegetable plantations) may be classified incorrectly and lead to a lower User’s Accuracy.
Table 4 also shows that a notable number of “Bare Soil” samples were classified as “Water”. Fig. 4 already shows a higher reflection of water in band 7 and 8. This higher reflection and also the misclassification may be related to impurities (e.g. a higher sediment load) inside of the water bodies.
The relatively low accuracy value (56.0 % User’s Accuracy) of the “Urban” class may be related to a mixed-pixel problem in the Sentinel-2 dataset. Individual residential or industrial buildings may be smaller than the resolution of the Sentinel-2 dataset (10m x 10m). As a result, a pixel represents a mixture of urban buildings and other surfaces (e.g. soil or trees). This mixture can lead to misclassification. Due to the high-resolution reference image, it is possible to interactively determine the main content of a pixel (e.g. urban buildings) and to assign it to the test sample classes. The mixed pixels of the Sentinel-2 dataset can thus lead to a lower accuracy in the "Urban" class.

The overall visual impression of the classification result (Fig. A2), as well as the overall accuracy and the overall Kappa coefficient (Tab. 4) show a good result and representation of the actual land-use.

2.2 River Shifting Change Detection Map

Rivers in Bangladesh are highly dynamic and underlie severe changes in location and intensity during a few years. During a few decades, rivers may change whole landscapes. The overall goal of this analysis is to provide information on the changes of the Padma river system course and the direction of shifting. The river system includes the water bodies and pointbars. A regional map covers these changes from the area west of Shivalaya in the northwest to the area of Sadarpur in the southeast (Fig. A5). Local changes inside this area are presented in a map showing only the city of Faridpur (Fig. A16). The main focus is the mapping of recent active areas of the river system and passive areas which were active in the past decades but are inactive recently. River course maps are provided for six time slices (1973, 1980, 1990, 2000, 2010 and 2019) (Fig. A8-A13). The change detection map shows data of the time slices with the highest difference in river system areas (1973, 2000 and 2019) (Fig. A8, A11, A13, A15). A map focusing on the Faridpur study area shows active and passive river system areas using all six time slices (Fig. A16).

Rivers inside the study area of Faridpur are often vegetation overgrown or tree canopied. Additionally, they are often smaller in width than the spatial resolution of the satellite images available (10m to 60m). For these reasons, the river course maps and the change detection map are only showing the changes of the main river of the Padma river system.

Data

To carry out the analysis, cloud-free optical images from Landsat Multispectral Scanner System MSS, Landsat Thematic Mapper TM and Copernicus Sentinel-2 missions are used. These are available during the period of the Bangladesh dry season between October and April, and images from January and February are used in the analysis. A comparison between images of different years is only possible when the target features (e.g. water) can be identified in all the images by similar response signal. This can be ensured by using images of the same month in every year of the analysis.

Starting 1973, one image per decade is used (1973, 1980, 1990, 2000, 2010 and 2019).

To enable comparability between the final river shifting products, only bands from the Landsat and Copernicus Sensors with similar wavelengths positions have been chosen for processing (see Tab. 5 and Annexure C: Data).

Table 5: *Overview of the satellite images and their bands used for the analysis (EUROPEAN SPACE AGENCY 2017; UNITED STATES GEOLOGICAL SURVEY n.d.).*

Mission	**Sensing Date**	**Bands (B), Spatial Resolution/ Wavelengths**	
		Green	**NIR**
Landsat MSS	21.02.1973	B4, 60m 0.5-0.6 µm	B7, 60m 0.8-1.1 µm
	16.01.1980		
Landsat TM	17.01.1990	B2, 30m 0.52-0.6 µm	B4, 30m 0.76-0.90 µm
	20.02.2000		
	15.02.2010		
Sentinel-2	11.02.2019	B3, 10m 0.538-0.583 µm	B8, 20m 0.76-0.97 µm

Methods

The workflow of the analysis is visualized in Fig. 5.

Atmospheric Correction

Different atmospheric conditions during the sensing times of the images can result in a different image feature of the physically same ground objects. Therefore, to enable the comparison between all the images, an atmospheric correction is mandatory. An atmospheric correction eliminates the atmospheric effects in an image and results in a surface reflectance image that characterizes the surface properties.

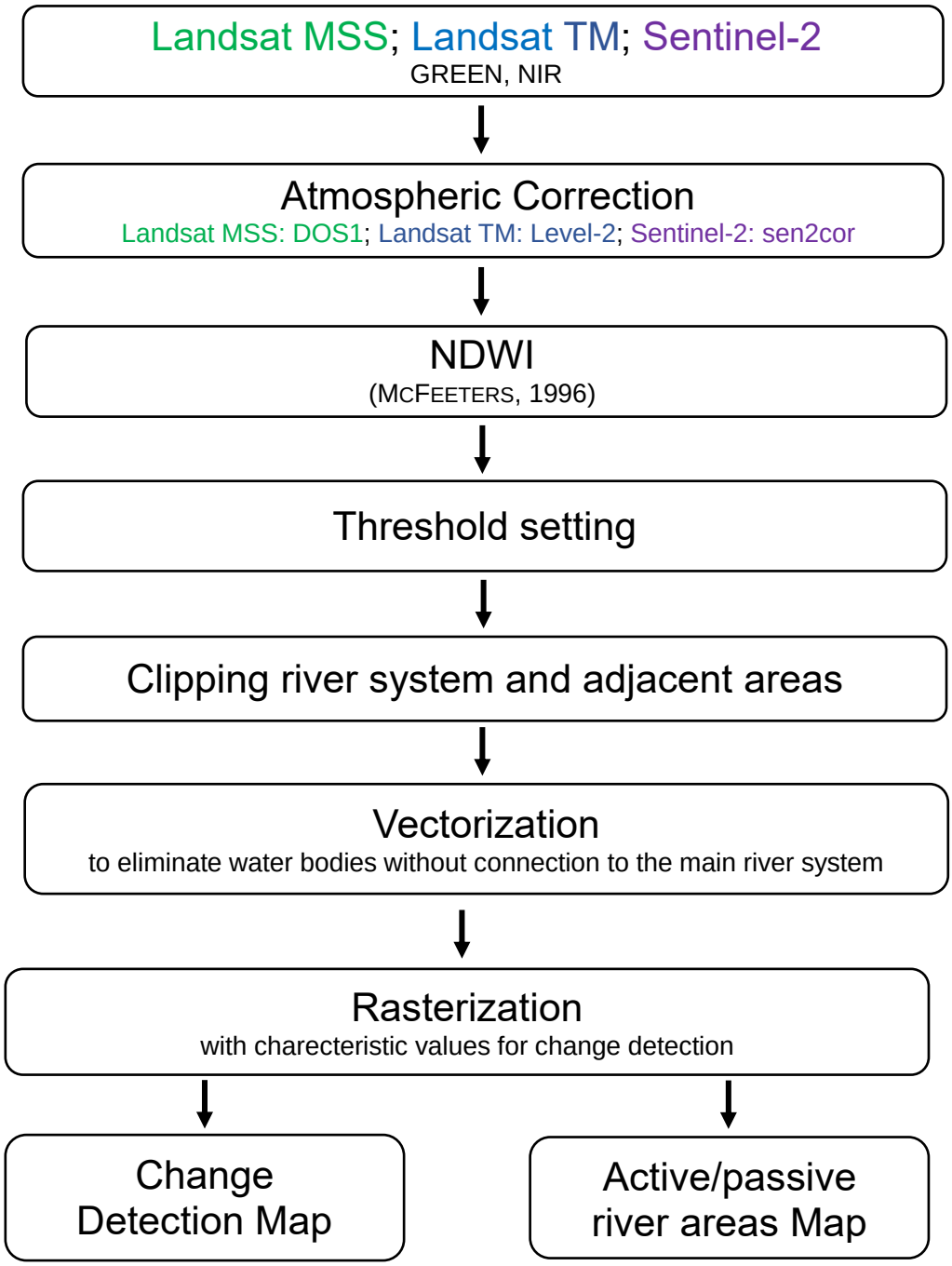

Figure 5: *Workflows of the River Shifting Change Detection analysis.*

Sentinel-2 and Landsat TM images are already atmospherically corrected and surface reflectance data are available for download (free Sentinel-2 download from Copernicus Open Access Hub and free Landsat TM download from USGS EarthExplorer).

The Sentinel-2 atmospheric correction is based on physical principals, physical-based algorithms use radiative transfer methods, which are simplified models of the radiation pathway from source to sensor, to model atmospheric scattering and absorption (LILLESAND ET AL., 2015). Auxiliary data such as water vapor data, atmospheric pressure or a digital elevation model are added to receive more precise information for the correction. The effects in the atmosphere are quantified by the model and used to calculate the surface reflectance values.

The Landsat TM surface reflectance "products are generated by a specialized software called Landsat Ecosystem Disturbance Adaptive Processing System (LEDAPS)" (LEDAPS PRODUCT GUIDE, 2020). Similar to the Sentinel-2 atmospheric correction, LEDAPS is also a physical-based algorithm that fits a radiative transfer model and includes auxiliary data to receive the atmospherically corrected surface reflectance product.

The Landsat MSS image is corrected by using the DOS1 (Dark Objects Subtraction) method. CHAVEZ (1996) describes that the methods "[…] basic assumption is that within the image some pixels are in complete shadow and their radiances [if above zero] received at the satellite are due to atmospheric scattering (path radiance). This assumption is combined with the fact that very few targets on the Earth's surface are absolute black, so an assumed one-percent minimum reflectance is better than zero percent." (CHAVEZ, 1996). The calculated radiance-value based on this assumption is used for the correction of the whole Landsat MSS image (image –based correction).

It is important to mention that the accuracy of an image-based correction technique is lower than a physically based correction (e.g. as applied for Sentinel-2) (CONGEDO, 2016). Nevertheless, CONGEDO (2016) states that image-based corrections "are very useful when no atmospheric measurements are available as they can improve the estimation of land surface reflectance" (CONGEDO, 2016).

Calculation of Normalized Difference Water Index (NDWI)

Using the respective bands of the images (Tab. 4), the NDWI is calculated (see Fig. A7). The Normalized Difference Water Index (NDWI) (MCFEETERS, 1996) uses the green and near-infrared bands to delineate open-water features.

Water surfaces show high reflections in the green and low reflections in the near-infrared wavelength region (see Fig. 6).

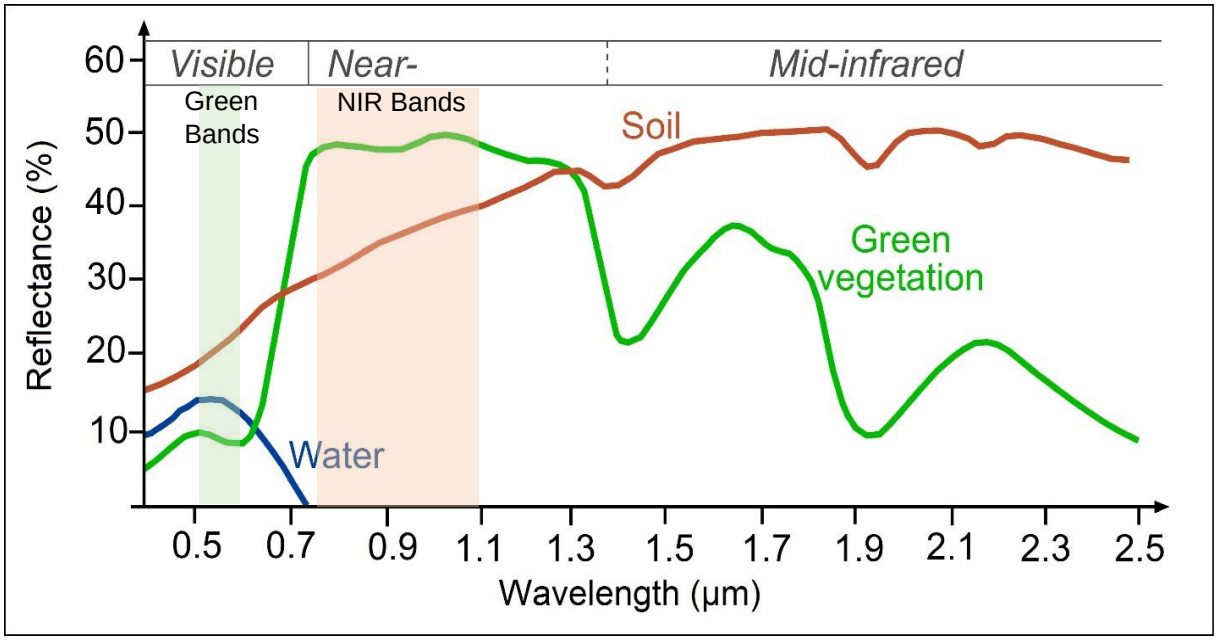

Figure 6: *Reflectance of water, soil and vegetation at different wavelengths; the wavelength areas used by the NDWI are highlighted in green (green bands) and red (NIR bands), modified after SEOS-PROJECT.EU, 2020.*

These differences are used to calculate an index that enhances the presence of open water features and suppresses the presence of soil and vegetation (McFeeters, 1996). The Waterindex is calculated as follows, using the respective bands of the satellite image:

$$NDWI = \frac{GREEN - NIR}{GREEN + NIR}$$

The generated index map contains values in the range of -1 to +1 (see Fig. A6), while excluding zero. Positive values are interpreted as water features. Soil and vegetation features have negative values (McFeeters, 1996).

Processing steps

At first, a threshold value is applied to discriminate between values that belong to the river system (water-bodies and pointbars) and all other values. This threshold value is defined manually by inspecting the pixels of the different NDWI images (see Tab. 6).

Table 6: *Thresholds to discriminate between river system and other values.*

NDWI image of the year	Threshold
1973	-0.2
1980	-0.18
1990	-0.18
2000	-0.2
2010	-0.12
2019	-0.18

The application of the thresholds results in maps that only show water-body and pointbar areas differentiated from other areas (see Fig. A7 as an example).

Based on these threshold maps, an area is clipped interactively (due to computing limitations of QGIS regarding data quantity) that covers mainly the river system (including water bodies and pointbars) and adjacent areas. In the next step, all remaining pixels of the river system in the clipped images are assigned the value “1”, whereas the areas below the threshold (see Tab. 6) are assigned NA.

The resulting image still includes many small objects that lie outside of the main riversystem (e.g. small ponds, agricultural canals). To eliminate these water bodies having no connection to the main river system, the raster data are vectorized and single isolated polygons are automatically eliminated, based on the assumption that the main river area shows in one connected polygon.

The results of all processed years are overlain to visualize the different extents (Fig. A8-A13). The three results with the greatest differences in extent are selected interactively and then processed for the change detection map: years 1973, 2000 and 2019 (Fig. A15).

Change Detection Map

The goal of the change detection map is to provide information on the changes of the Padma river system course and the direction of shifting. The changes are visualized in a single map. The conversion of the vector map (polygons) back to a raster map enables to present different river areas with characteristic values in a single map.

A unique year-dependent characteristic value is assigned to the cells of each new raster image (see Tab. 7). The raster cell size is set to 20 m, as this is the pixel size, needed by the successive project analyses.
The yearly products are joined to receive the change detection map of the area of the Padma river system for the different years (see Tab. 8).

Table 7: *Overview of the characteristic values per year.*

	1973	**2000**	**2019**
Characteristic value	1	10	100

Table 8: *Legend of the raster values in the change detection map.*

Raster value	**Area of the Padma river system in**
1	1973
10	2000
11	1973, 2000
100	2019
101	1973, 2019
110	2000, 2019
111	1973, 2000, 2019

Mapping active and passive river system areas
In the Faridpur study area, the information of all results (1973, 1980, 1990, 2000, 2010, 2019) are included into a map that presents active and passive areas of Padma river system.

Active areas are defined as the area of the Padma river system in 2019.

Passive areas are defined as the area of the Padma river system in all years before 2019 but not in 2019.

The polygons of each year are rasterized. A unique year-dependent characteristic value is assigned to the cells of each new raster image (see Tab. 9). The raster cell size is set to 20 m, as this is the pixel size, needed by the successive project analyses.

The individual results are joined. The values of the map represent the area of the Padma river system in different years (see Tab. 10). To reduce the values to active or passive areas, the raster is reclassified into two classes (see Tab. 10).

Areas where the river is not classified in 2019, are defined as passive and are assigned with a value of “1”. Areas, which show the river system in 2019, are defined as active and are assigned with the value of “2”.

Table 9: *Overview of the characteristic values per year for the mapping of active/passive river system areas.*

	1973	**1980**	**1990**	**2000**	**2010**	**2019**
Characteristic value	1	10	100	1000	10000	100000

Table 10: *Legend of the raster cell values in the map of active/passive river system areas.*

Characteristic value	**Area of the Padma river system in**	**Reclassified value (1=passive/2=active)**
1	1973	1
10	1980	1
11	1973, 1980	1
100	1990	1
101	1973, 1990	1
110	1980, 1990	1
111	1973, 1980, 1990	1
1000	2000	1
1001	1973, 2000	1
1010	1980, 2000	1
1011	1973, 1980, 2000	1
1100	1990, 2000	1
1101	1973, 1990, 2000	1
1110	1980, 1990, 2000	1
1111	1973, 1980, 1990, 2000	1
10000	2010	1
10001	1973, 2010	1
10010	1980, 2010	1
10011	1973, 1980, 2010	1

10100	1990, 2010	1
10101	1973, 1990, 2010	1
10110	1980, 1990, 2010	1
10111	1973, 1980, 1990, 2010	1
11000	2000, 2010	1
11001	1973, 2000, 2010	1
11010	1980, 2000, 2010	1
11011	1973, 1980, 2000, 2010	1
11100	1990, 2000, 2010	1
11101	1973, 1990, 2000, 2010	1
11110	1980, 1990, 2000, 2010	1
11111	1973, 1980, 1990, 2000, 2010	1
100000	2019	2
100001	1973, 2019	2
100010	1980, 2019	2
100011	1973, 1980, 2019	2
100100	1990, 2019	2
100101	1973, 1990, 2019	2
100110	1980, 1990, 2019	2
100111	1973, 1980, 1990, 2019	2
101000	2000, 2019	2
101001	1973, 2000, 2019	2
101010	1980, 2000, 2019	2
101011	1973, 1980, 2000, 2019	2
101100	1990, 2000, 2019	2
101101	1973, 1990, 2000, 2019	2
101110	1980, 1990, 2000, 2019	2
101111	1973, 1980, 1990, 2000, 2019	2
110000	2010, 2019	2
110001	1973, 2010, 2019	2
110010	1980, 2010, 2019	2
110011	1973, 1980, 2010, 2019	2
110100	1990, 2010, 2019	2

110101	1973, 1990, 2010, 2019	2
110110	1980, 1990, 2010, 2019	2
110111	1973, 1980, 1990, 2010, 2019	2
111000	2000, 2010, 2019	2
111001	1973, 2000, 2010, 2019	2
111010	1980, 2000, 2010, 2019	2
111011	1973, 1980, 2000, 2010, 2019	2
111100	1990, 2000, 2010, 2019	2
111101	1973, 1990, 2000, 2010, 2019	2
111110	1980, 1990, 2000, 2010, 2019	2
111111	1973, 1980, 1990, 2000, 2010, 2019	2

Results and Discussion

The resulting maps are added in Annexure A (A5-A16) and described in this section. For better orientation, topographical information and some in Bangladesh well-known cities are included in the final map visualization of the remote sensing based products.

Extent of Padma river system and its water body

As already mentioned, the NDWI values greater than the threshold lead to the classification of a larger area than just the water bodies as it includes water bodies and pointbars. All together is interpreted as full extent (maximum water coverage) of the Padma river system based on discussions with the GSB colleagues. As an example, Figure A14 shows the NDWI result for 2019 with a threshold greater than -0.18 overlain on the Sentinel-2 RGB 432 image from 2019. It is visible that the water body and pointbars are included into the result.

Figure A8 to A13 show in blue the extents of the Padma river system (based on NDWI) in the years of 1973, 1980, 1990, 2000, 2010 and 2019.

The different levels of details between the final maps are caused by the different spatial resolutions of the images. Due to the higher spatial resolution, Sentinel-2 shows more details than Landsat TM and Landsat MSS (Tab. 5).

It can be summarized, that the general shape of river system for the different years is visible in all decades.

Change Detection Map

Based on the NDWI evaluations, the change detection map is calculated (Fig. A15). This map includes information on the shifting direction of the river system, together with the locations of land-loss and possible land-gain. Furthermore, it shows which regions were part of the river system for the period between 1973 and 2019 (Fig. A15, dark blue).

In several regions of the river areas, changes in time are observable (Fig. A15): West of Shivalaya, a retreat of the river system is clearly visible. Turquoise color indicates the location of the river system in 1973; light green shows it in both years of 1973 and 2000 In the time slices 1973 and 2000, the area west of Shivalaya–was part of the river system. The change detection map visualizes a retreat of the junction to the southeastern direction. Parts of the former river area in 2019 changed to land that is bordered by the rivers of Jamuna in the east and Padma in the south.

A similar relocation is visible north of the study area of Faridpur. In this area turquoise and light green colors indicate a retreat of the river system to the east (Fig. A15). This retreat corresponds to a shifting of the Padma river system to the east. On the riverbank opposite to the study area of Faridpur, light orange color indicates the location of the river system in the year 2000, dark orange color shows the river location in the years of 2000 and 2019 and red color indicates the location in the year of 2019. Thus, the change detection map visualizes a clear shift to the east from the year 2000 onwards (light orange and dark orange). Nevertheless, between the years 2000 and 2019, the river system experienced a slight retreat to the west (light orange). During the shift to the east, a former river area (in 1973 (turquoise color), 2000 (light orange) and 1973/2000 (light green)) developed to a large river island surrounded by two river channels of the Padma river system.

Immediately east of the Faridpur study area, a north to south flowing river channel is visible in the change detection map. The red color indicates that the river channel only exists in the change detection time slice of 2019. Following that, the river channel developed between the timeslice/year of 2000 and the timeslice/year of 2019. Fig. A12 specifies this argument as the map is showing the mentioned river channel already in the year of 2010, which is not visible in the change detection result. Therefore, it can be concluded that, the river channel bordering Faridpur study area developed between the years 2000 and 2010.

In conclusion, the river system east of the study area of Faridpur developed from a quite straight and slim flowing river channel in 1973 to a wider system with multiple river channels flowing parallel. It is important to mention that a single channel developed in immediate neighborhood of the eastern border of the study area of Faridpur.
Worth to mention is also that the riverbanks directly at the Daulatdia and Paturia Ferry Terminals stayed relatively stable compared to the changes east of Faridpur. A possible explanation could be an anthropogenic embankment along the riverbanks to keep the ferry terminals functional.

Overall, the Change Detection Map in Figure A15 shows significant changes of the Padma river system between the years of 1973 and 2019. Of particular note is the development of the river system east of Faridpur. Within about 50 years, the Padma River has widened significantly by developing from two river channels in 1973 to three river channels in 2019.
The change detection map shows significant changes of the river system also outside of the study area that should be considered for further urban planning in Faridpur.

Active and passive river areas in Faridpur study area
In the Faridpur study area, the change detection map shows active and passive areas (Fig. A16). The map allows locating areas of sedimentation processes (passive areas) and provides indications on other geo-related processes (e.g. liquefaction-prone areas).

2.3 Inundation Map
Due to climate change, Bangladesh is experiencing an increase in rural-urban migration movements. Therefore, the demand for safe building ground is very high. One result is an increasing lateral growth of urban areas. However, urban growth is limited to suitable building ground and eligible areas are often low-lying and therefore prone to flooding during the yearly monsoon season between May and October. Planning agencies may benefit from geodata on inundation-prone areas that are reliable, available frequently and sustainable, easy to process and easily understandable.

The overall objective of this analysis is to receive a map that gives an overall impression on the frequency of inundation in areas that are at risk of flooding (Fig. A17) for the years 2015 to 2020. The analysis is carried out using 21 Sentinel-1 radar images from 2015 to 2020 and a threshold approach to differentiate between inundated and non-inundated areas. To ensure an easy processing of the large amount of multi-temporal radar data, the analysis is carried out using the online processing tool Google Earth Engine (see the programming code in Annex B).

The Bangladesh Water Development Board (BWDB) already established inundation mapping using Sentinel-1 datasets. In their annual flood reports, the BWDB is using an inundation map to verify the output of a flood-forecasting model (BANGLADESH WATER DEVELOPMENT BOARD 2018, pp. 92-93).

Data

The analysis is based on Copernicus Sentinel-1 images starting 2015, with operation of the Sentinel-1 sensor.

Google Earth Engine states to preprocess the images using the Sentinel-1 Toolbox to receive radiometrically calibrated images, terrain corrected and thermal noise removed (GOOGLE EARTH ENGINE DATA CATALOG, 2020).

A data selection from the rainy season in Bangladesh is required to map the maximum inundation. The selected images are acquired in “IW” (interferometric wide swath), the default acquisition mode of Sentinel-1 (EUROPEAN SPACE AGENCY, 2020). To differentiate between water and non-water pixels, the VH polarization is selected. Preliminary works in the study areas have shown that VH is the most suitable polarization for the detection of water. The respective spatial resolution of the VH polarization images is 10 meter.

The Bangladesh rainy season is roughly between May and October of each year. The time of maximum inundation for the study area of Faridpur is set to the months of July and August of each year. This assumption is based on the experience and knowledge of colleagues at the Bangladesh Geological Survey (GSB), the flood reporting by the BWDB (see e.g. BANGLADESH WATER DEVELOPMENT BOARD, 2017, 2018, 2019) and by interactively assessing and selecting the images from a period that show the largest inundated areas. Since the exact dates of maximum inundation of a year are unknown, all available images of July and August of each year are processed in this analysis.

Finally, using the above-mentioned benchmarks, 21 Sentinel-1 images of descending orbits are selected for the processing (Annex B, lines 8-23). Annex C: Data lists the images in a table.

Method

The workflow of the processing in Google Earth Engine is visualized in Fig. 7. The selected images of each year are combined and mean values are calculated. The mean-value images are subsetted to fit the extent of the study area (see Fig. A18; Annex B, lines 24-29).

Thresholding

Water surfaces appear in black and dark gray colors in the averaged amplitude images (see Fig. A18). In order to identify a threshold value, the values of assumed water and non-water image areas are identified interactively. Based on experience in the definition of thresholds discriminating between water and non-water surfaces, the identified threshold values in Bangladesh range from -20 dB to -22 dB. For the Faridpur study area, a threshold value including values smaller than -20 dB is chosen and applied to images from all years (Annex B, lines 109-118). The output image only shows pixels smaller than the threshold, representing the inundated areas of each year (see Fig. A19).

All areas that have been flooded between 2015 and 2020, are compiled by combining the threshold images of all years into one image (see Fig. A17; Annex B, lines 120-123). The result is exported with a 20m spatial resolution, which is a requirement for further analyses in the project (Annex B, lines 129-141).

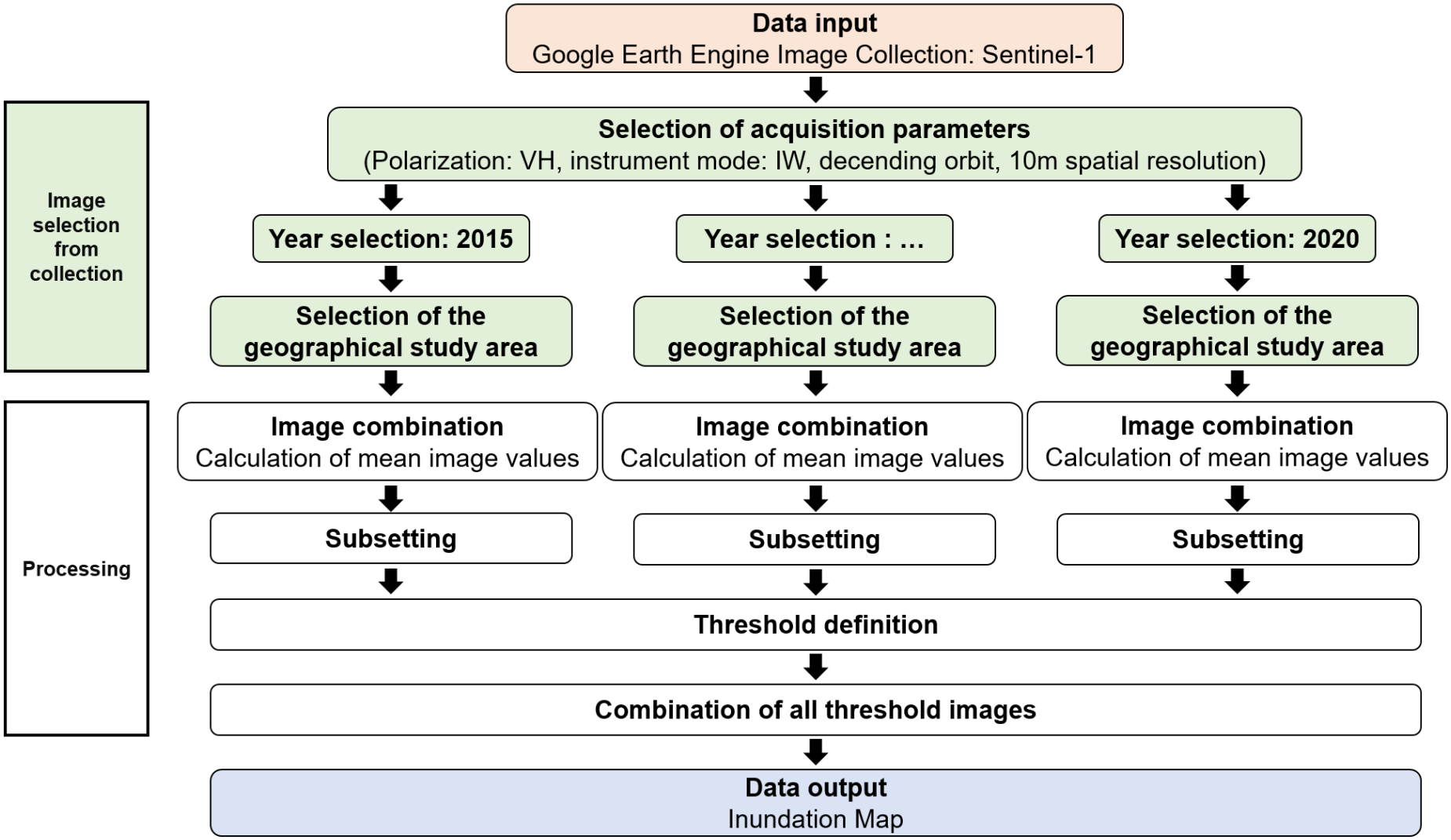

Figure 7: *Workflow of the Google Earth Engine processing of the inundation mapping method.*

Results and Discussion

The resulting map presents the areas and frequencies of inundation between 2015 and 2020 (see Fig. A17).

The map exhibits a larger east-west complex in the center of the study area between the landmarks of Raghuunandanpur and Govt. Rajendra College, which shows less inundated areas in the years from 2015-2020. The majority of inundated areas is located in the outskirts of Faridpur.

Figure 8: *Low-lying area that is inundated regularly during rainy season. The elevated areas on the left side indicate a part of the east-west running road bordering the area. Rural settlement structures are located along this road. Viewing direction: SW. Faridpur, 02/2019. Photo: L. Wimmer.*

The largest continuous inundated area is visible in the extreme northeast of the study area. Large extents of the area were inundated at least three to four times during the study period. The predominant influence in this area is the Bhubaneswar River, a branch of the Padma River that immediately adjoins the area to the east. Low-lying areas (as seen in Fig. 8) are more likely to be inundated during the rainy season followed by the deposition of sand. The elevated areas of the road and the rural settlement structures are not affected by the inundation.

Figure 9: *Extraction of sand as a raw material for brick production. View over low-lying areas that are inundated frequently during the rainy season. Viewing direction: NE. Faridpur 02/2019. Photo: L. Wimmer.*

Secondly, this area is extensively used by brick factories, which use the during sand deposited during inundation events as their raw material for brick production. Fig. 9 is located north-east of the road junction that is shown north-west of the Tepakhola landmark (Fig. A17).

The area shows deep extraction pits that are inundated frequently (see Fig. 9). According to local workers, sand extraction and brick production have been at this site for about 35 years and remained stationary during this time.

As shown in the River Shifting Change Detection investigation (see Chapter 2.2), this area is additionally influenced by a westward movement of the Padma river system which may explain the high-frequency inundation events.

Another area that is inundated between two to four times within the six-year period of the study is the region south-west of the Bil Mahmudpur landmark (Fig. A17). According to local workers, the waterbody in Fig. 10 holds water during the whole year. Instead of a direct agricultural use of the waterbody area, the water is used to irrigate the surrounding rice fields of the low-lying area.

Figure 10: *Low-lying area of frequent inundation south-east of the Bil mahmudpur landmark. The area is characterized by agriculture, predominantly rice farming. The water in the image is used as irrigation for farming. Viewing direction: S. Faridpur 02/2019. Photo: L. Wimmer.*

Between the landmarks of Banangarm in the southwest of the study area and the Faridpur Medical College Hospital in the South, a large area of frequent inundation is visible (Fig. A17). The results show, that most of the area is only inundated once or twice during the six-year period, but there are also inundation clusters that show an inundation frequency of three to five times. In comparison with the land-use map (Fig. A3, see chapter 2.1) it is visible that this low-lying region is used for agriculture (also see Fig. 11a/b).

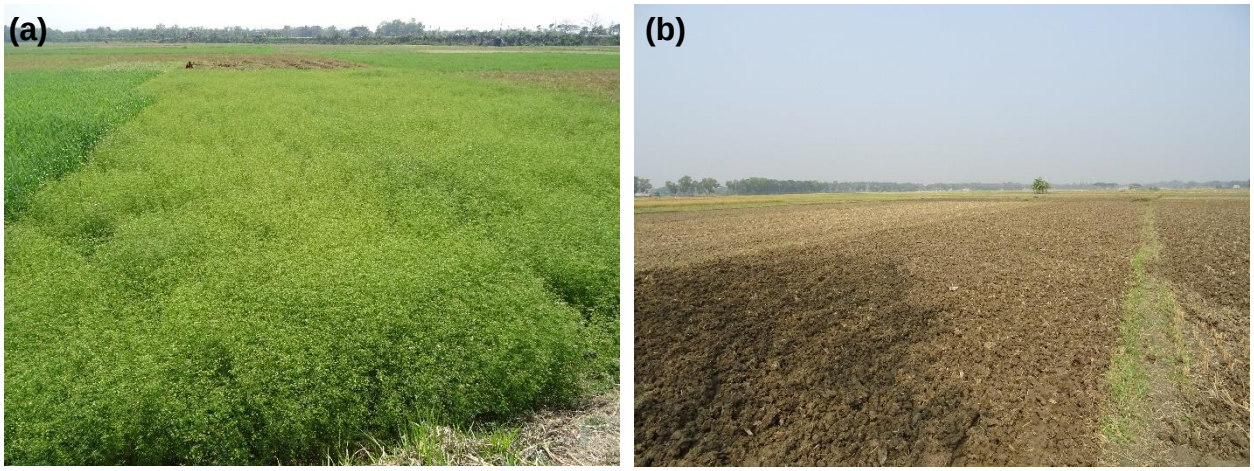

Figure 11: *Low-lying agricultural used area south-west of Faridpur Medical College Hospital landmark. (a) Agriculture in 02/2019, at the horizon an elevated road is visible, running north-west/south-east through the area. View direction: S. (b) Agricultural fields in 11/2019. View direction: N. Photos: L. Wimmer.*

Many small areas in the Faridpur city area are inundated yearly, representing ponts and lakes as they partially overlap with the water bodies in the topographic base map (data of the Survey of Bangladesh and OpenStreetMap).

It can be concluded that between 2015 and 2020 for the months July and August (rainy season) mainly areas in the rural outskirts of Faridpur were inundated. The frequent inundation occurs in the areas of brick production in the north-west of the study area due to its direct neighborhood to the Padma river system. Also, examples as presented in Fig. 11a/b, show that areas which are used for agriculture are affected by high frequency inundation. The urban area of Faridpur city experiences a non-annual inundation.

2.4 Ground Motion Map

2.4.1 Introduction

Within the project Geo-Information for Urban Planning and Adaptation to Climate Change (GPAC), a project of German-Bangladeshi technical cooperation and carried out by the Geological Survey of Bangladesh (GSB) and the German Federal Institute for Geosciences and Natural Resources (BGR), ground motion products based on Radar Interferometry (InSAR) were created for several study sites in Bangladesh. The goal of these analyses is to establish a workflow for the systematic integration of ground motion data into a climate change adapted urban planning in Bangladesh. The availability of free, medium resolution, radar satellite images through the European Copernicus program and the progress in computing capabilities, open up new opportunities for the wide-scale, multi-temporal and continuous ground motion analysis based on satellite data.

In the context of an advancing urbanisation and the resulting increased demand in suitable building space, in combination with the particular exposure of Bangladesh to climate change related risks, InSAR ground motion products enable the identification and monitoring of potentially stable areas and can be used in the prediction of inundation scenarios. In combination with other relevant geodata, InSAR can hence contribute to the assessment of building ground suitability.

In this section, the results of the InSAR analysis for the city of Faridpur from October 2014 to December 2019 are presented and discussed.

2.4.1.1 SAR Interferometry (InSAR)

SAR interferometry (InSAR) is a technique for the precise measurement of topography and terrain movement in the range of several millimetres from two or more SAR images (see Figs. 12 and 13). The different methods used in this field have in common that they exploit the phase information contained in the images acquired from two or more different sensor positions (spatial baselines) and/or at different acquisition times (temporal baselines). Concretely, the phase difference between the different acquisitions (the so-called interferometric phase) implicitly contains information about the topography of the area of interest and – when data from different points in time is available – on any terrain movements during the observation period.

When terrain deformations are to be observed over a longer period, the issue of increasing loss of coherence - or decorrelation - between the different scenes arises. Coherence is estimated from the amplitude of the complex correlation coefficient of two SAR images. In the context of SAR interferometry, coherence is used as a measure to evaluate the quality of the phase difference; high coherence indicates high quality of the phase difference while low coherence indicates a highly noisy phase difference (LÓPEZ-MARTÍNEZ ET AL., 2004).

Decorrelation particularly affects areas with vegetation (forests, parks, farmland …) where the backscatter to the radar sensor is subject to high temporal variations due to quick changes in geometry (e.g. leaves moving with the wind) and dielectric properties (moisture variations). It also affects areas with a low backscatter to the sensor such as smooth surfaces (water, roads, airstrips …) or areas of radar shadow. In these areas, noise dominates the return signal (low signal-to-noise ratio). In essence, decorrelation occurs when the contributions of topography and deformation to the total phase difference are superimposed by random phase contributions and noise, and can no longer be isolated. As a rule of thumb, the longer the time gap between two acquisitions and the larger the spatial distance between the sensor positions (temporal and spatial baseline), the higher the degree of decorrelation (WOODHOUSE, 2006).

Therefore, if the goal is to examine deformation time series, one has to limit the analysis to image pixels that are less affected by decorrelation. That is, pixels that exhibit a strong and stable backscatter to the radar sensor even over long periods of time. These sort of targets are usually abundant in urban areas and correspond to man-made structures. In addition, natural targets such as rocks, gravel fields and even desert surfaces can be sufficiently stable over time to be considered for multi-temporal

analyses. There are different approaches in this field of multi-temporal radar interferometry. Two approaches, Persistent Scatterer Interferometry (PSI, see FERRETTI ET AL., 2001) and Small Baseline Subset (SBAS, see BERARDINO ET AL., 2002) are used in the frame of this work and are described briefly in the following section.

2.4.1.2 Multi-temporal InSAR (PSI and SBAS)

Persistent Scatterer Interferometry (PSI) is a technique that relies on point targets, which have a strong backscatter and are stable over time (so-called persistent scatterers, PS). Within an image pixel, a PS has to be dominant while the backscatter contributions of the other objects (scatterers) within that resolution cell can be neglected. These conditions are normally fulfilled by artificial (i.e. man-made) objects which are particularly prevalent in urban areas. Examples include cell phone towers, roofs and edges of houses, bridges, metallic structures, utility poles, etc. These objects are referred to, in the context of radar interferometry, as *persistent scatterers* and can be identified within the image stack using different methods. Frequently, the amplitude stability over the observation period is considered for this purpose. PSI is particularly effective in urban areas with a high density of point targets. In rural areas on the other hand, the number of potential PS is considerably less.

The PSI algorithm initially selects a master image from the stack of available radar acquisitions based on a minimisation of the average spatial and temporal baseline with respect to the other images in the stack. Secondly, one interferogram is created between the master image and each of the secondary images. All images in the stack of acquisitions are then *zero baseline steered*, i.e. the measured interferometric phases are adjusted for the different imaging geometries of the different acquisitions with respect to the master image, using an external DEM like e.g. SRTM and precise orbit information. The next step is the identification of PS candidates. Here, the classical approach is to use the amplitude stability over time. Subsequently, and using an iterative approach, the atmospheric and topographic phase contributions are calculated and removed and the deformation velocity for the PS is calculated. To do so, a deformation model is applied. In the most common case, a linear deformation model is used (see FERRETTI ET AL., 2001).

Small Baseline Subset (SBAS) is another method for multi-temporal radar interferometry that uses a network of interferograms. Instead of choosing a single reference image for all interferograms, groups (subsets) of images are considered that

have been acquired with a small temporal and spatial baseline. Subsequently, for each image combination within a subset, an interferogram is calculated respectively (as long as a user-defined maximum temporal and spatial baseline is not violated). For this reason, in SBAS the number of interferograms is usually much higher than the number of available SAR acquisitions. In order to achieve a continuous motion time series, the individual subsets are subsequently linked together (see BERARDINO ET AL., 2002). Since SBAS tries to minimise the temporal and spatial baseline between the images of a particular subset, the resulting interferograms are less affected by decorrelation when compared to PSI. This leads to the detection of more stable points (scatterers) including natural objects such as rocks, gravel fields or desert surfaces. SBAS is also able to deal with disconnected subsets (although this should be avoided) and can interpolate over points that are affected by a temporal loss of coherence.

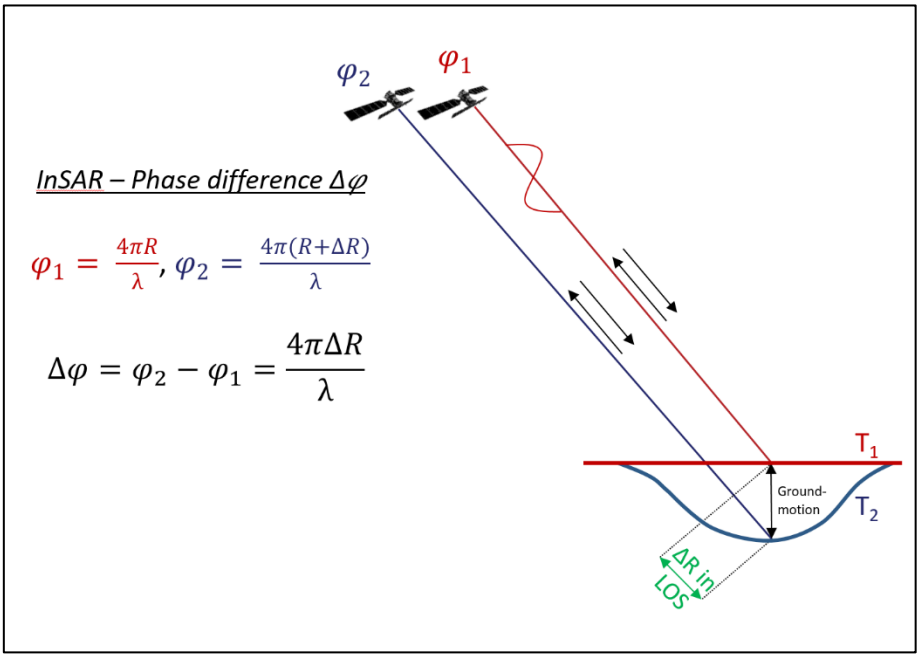

Figure 12: *Schematic representation of InSAR basic principle.*

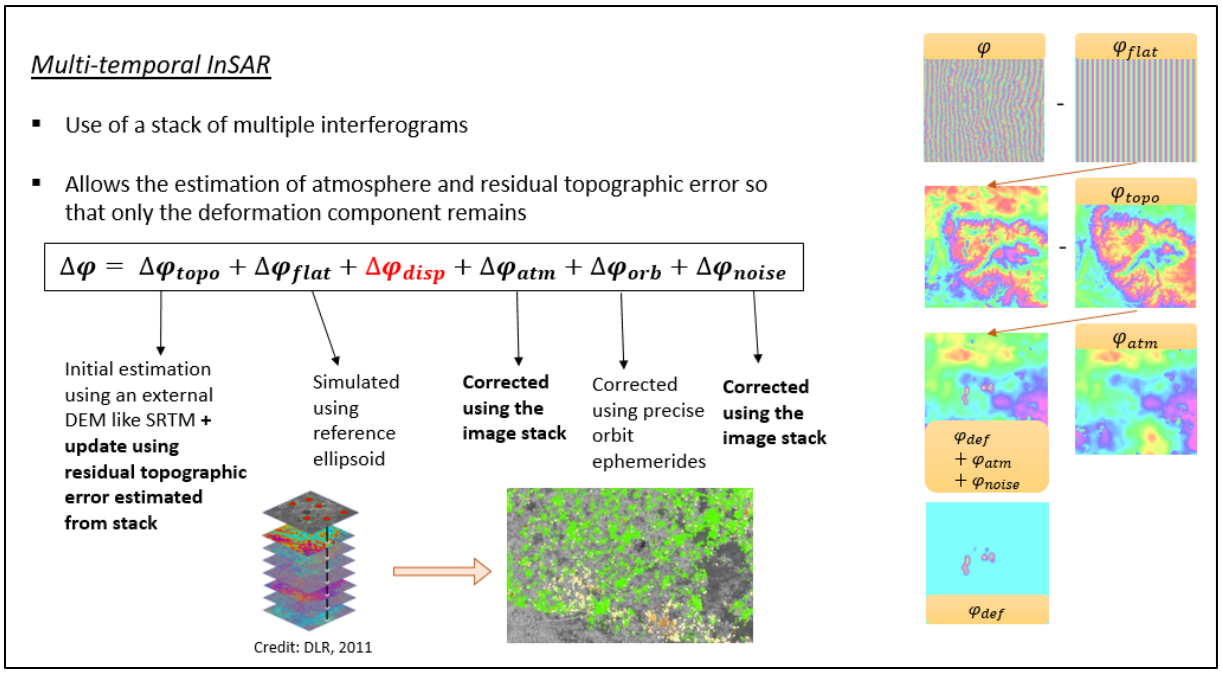

Figure 13: *Schematic representation of an interferometric stacking (multi-temporal InSAR) approach.*

2.4.1.3 Multi-temporal InSAR limitations

The deformation measured in radar interferometry is always along the line-of-sight of the imaging sensor/satellite and not the true vertical deformation. SAR sensors are not nadir looking but instead are looking at the ground obliquely with an incidence angle. For Sentinel-1 this angle is between 20 and 45 degrees with respect to nadir. However, the vertical deformation component can be estimated with a certain probability using adjustment calculation if acquisitions from both satellite orbit directions (ascending and descending) are available. In this case, two images acquired in different orbits with different look angles are used to estimate the vertical motion component and one horizontal motion component (usually the east-west component is estimated since the north-south component is not well constrained by most satellite imaging geometries). Furthermore, in radar interferometry all the estimated velocities and displacements are relative to one or several reference points. The principal reference point is assumed to be stable over the whole observation period, an assumption that is not always true. In order to get the absolute motion, GNSS or other survey data is required, to which the dataset can be referenced instead. For our analyses within the GPAC project, no external reference data is used, as no adequate GNSS are available.

Another aspect that needs to be considered is the ability to exactly assign a particular deformation measurement to an object on the ground. For the German Ground Motion Service (BBD) a mean geolocation accuracy of 3.5 metres for strong point targets was

shown (KALIA ET AL., 2020). In the case of SBAS, assigning a particular object to an observation proves more challenging since SBAS applies spatial averaging of adjacent pixels, merging together signals from numerous individual scatterers.

The ambiguous nature of the phase information contained in SAR images (only displacements corresponding to fractions of a wavelength can be measured) means that InSAR is limited in its ability to measure fast displacements. In fact, the maximum theoretical displacement that can be measured between two scenes corresponds to one fourth of the wavelength. CROSETTO ET AL. (2016) described the maximum differential accumulated deformation rate measurable with Sentinel-1 with 42.6 cm/year. A final limitation that needs to be mentioned is the availability of coherent targets. While SBAS is able to detect a high density of targets even in rural areas, neither technique (PSI or SBAS) can provide information in areas where there are strong changes in ground cover over time (for example seasonally flooded fields).

The BGRs Remote Sensing Working Group is mainly using ENVI SARscape software for InSAR processing. This software is developed by the Swiss company sarmap S.A. and is entirely integrated into ENVI. For PSI, SARscape currently only supports linear deformation models while the SBAS implementation in SARscape also supports non-linear models.

2.4.2 Methods

2.4.2.1 Project area

Faridpur is a city in the Dhaka Division in central Bangladesh roughly 100 km West of Dhaka (see Fig. 14). It is located on the western bank of the Padma River and had a population of around 120,000 in the 2011 government census. Faridpur has a flat topography without any pronounced features. The average elevation is roughly 10 meters above sea level. The city is furthermore characterised by numerous waterbodies (ponds, channels, rivers) in particular the massive Padma River that forms the natural eastern border of the city. The areas to the south, west and northwest of the relatively small city centre are characterised by agricultural fields seamed with rural settlements built mostly on elevated dikes or natural levees. The northeast is characterised by brick factories and adjacent housing facilities for the workers.

Faridpur has experienced intense construction activities over the past two decades. Before the year 2000, most buildings in the city had two or three stories. Today the city centre features a large number of high-rise buildings while there continues to be a high

level of construction activity including the topping up of existing buildings. To the south of the city centre, one can find a number of large public institutions such as the River Research Institute, the Faridpur Medical College and the Faridpur Engineering College. The campus of the Medical College has recently undergone a large-scale extension and, in November 2019, parts of the campus were still under construction. The Faridpur Engineering College was established in 2010 and occupies large, newly built facilities.

While the Faridpur project area has a size of 77 km², for the InSAR analyses a larger area of 216 km² was chosen. This area covers the city of Faridpur and its immediate suburbs. Even though the deformation dynamics within the city of Faridpur are the main focus of this work, a larger area was consciously chosen for the InSAR processing, to enable a higher selection of potential reference points in the phase unwrapping part of the processing.

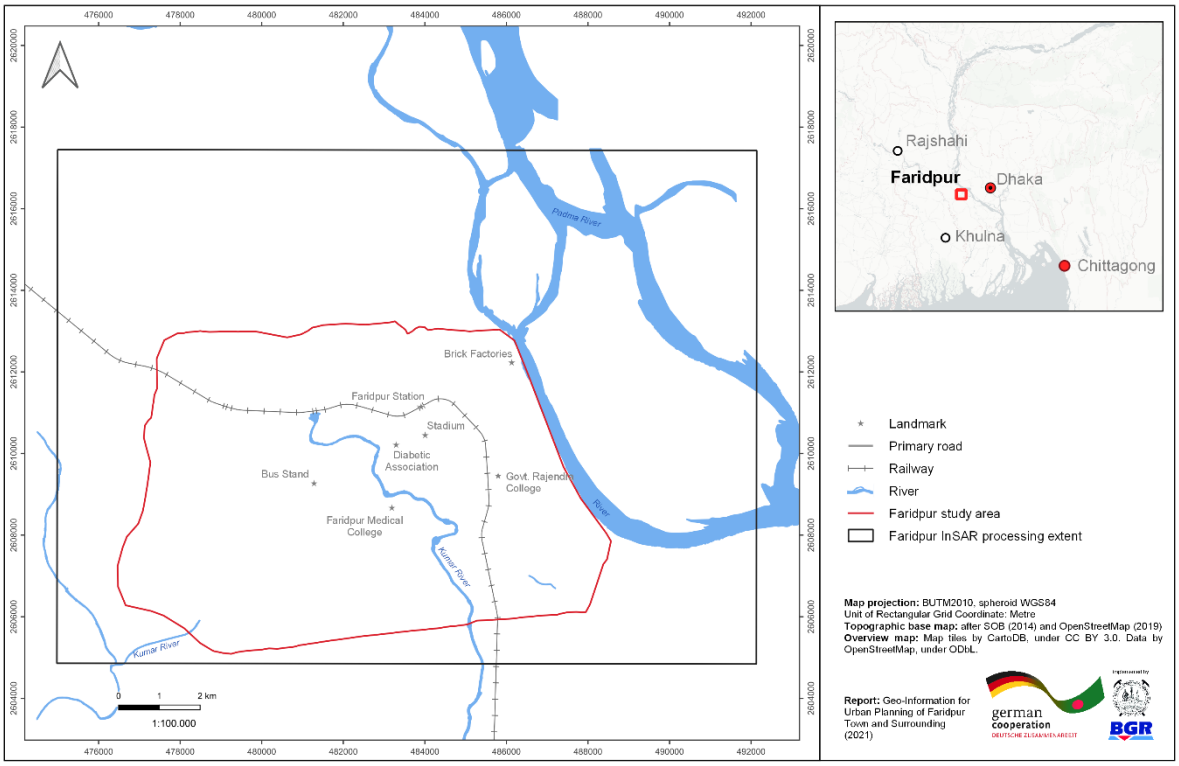

Figure 14: *Map of project area and InSAR processing area.*

2.4.2.2 Data and data download

The radar interferometry analyses carried out within the scope of the GPAC project are based on Sentinel-1 data. Sentinel-1 is a C-band radar satellite constellation operated by the European Space Agency (ESA) consisting of two identical satellites – Sentinel-1a and Sentinel-1b. The data is distributed free of charge by ESA.

For the Faridpur area, Sentinel-1 data covering the period from October 2014 to December 2019 in the ascending and the descending orbit direction is used. Until April 2017 roughly one acquisition per month is available for each orbit direction. Starting from April 2017, a repeat cycle of roughly 12 days is available for each orbit direction. In total, 323 Sentinel-1 scenes are downloaded for the Faridpur analyses. Some of these scenes cover adjacent tracks on the same acquisition date and are mosaicked together. Mosaicking resulted in 233 individual scenes (see Annexure C: Data).

Sentinel-1 data can be downloaded from the Copernicus Open Access Hub (https://scihub.copernicus.eu/) and from the Alaska Satellite Facility (ASF) (https://asf.alaska.edu/). For this project, all Sentinel-1 data are downloaded through the ASF. For more details on the download process, please refer to the *Interferometric Stacking in SARscape Processing Guidelines.*

2.4.2.3 Orbit files download

In addition to the image files, it is necessary to download the so-called precise orbit ephemerides files. These are highly precise satellite position vectors, which are available online 20 days after the Sentinel-1 acquisitions are published. These vectors are necessary for InSAR processing, since the exact sensor position at the time of acquisition is needed for high quality InSAR results. The orbit files can be downloaded from the *Sentinel-1 Quality Control* website (https://qc.sentinel1.eo.esa.int/).

For an InSAR analysis only those Sentinel-1 scenes should be considered, which are older than 20 days at the time of the analysis. The accuracy of the satellite positions after the update using precise orbit information is given by ESA with 5 cm (3D RMS). For more information on the orbit file download, please refer to the *Interferometric Stacking in SARscape Processing Guidelines.*

2.4.2.4 SARscape PSI and SBAS workflow

ENVI SARscape is used in this project for InSAR processing. The PSI workflow within the software consists of five steps: Connection graph, Interferometric process, Inversion: First Step, Inversion: Second Step and Geocoding. Once both orbit directions are processed until the Geocoding step, the tool Shape Combination is used to combine both datasets and estimate the vertical deformation component.

SBAS processing was also done using ENVI SARscape. The SBAS workflow consists of seven iterative steps: Connection Graph, Interferometric Process, Ground Control Point Selection, Refinement and Re-Flattening, Inversion: First Step, Inversion: Second Step and Geocoding. As with PSI, both orbit directions were processed separately and then merged using the Meta Combination tool. In following, the processing steps are briefly explained.

The first step in the PSI and SBAS processing chain is the **Connection Graph** tool. For PSI, this function analyses the stack of SAR images and selects the best master image from the stack (based on temporal and spatial baseline). All differential interferograms are subsequently formed with this master image. For SBAS the tool creates a network of image connections based on a user defined maximal temporal and spatial baseline. For every image connection, an interferogram is formed in the following step. Not all images in the network need to be directly connected to each other. Ideally however, all images are connected at least *indirectly*.

The Connection Graph tool also creates a working directory in which the outputs of all the processing chain's steps are stored and creates the auxiliary.sml file in the working directory. This file is needed as an input to all the following steps and it contains information about the data used and the progress of the processing chain

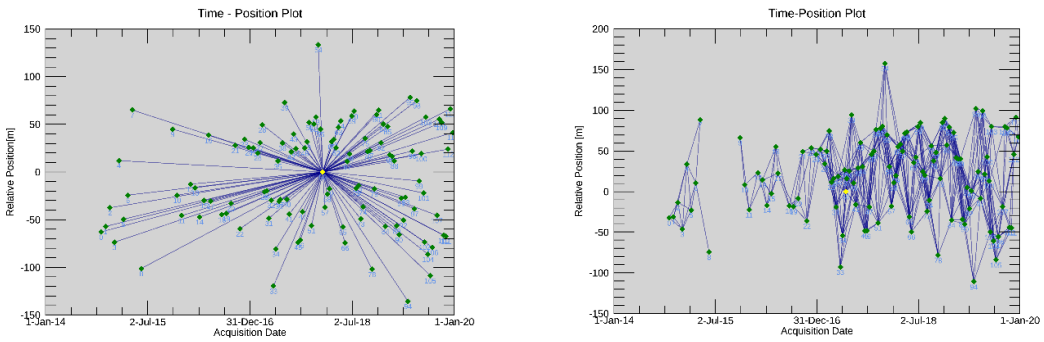

Figure 15: *Right: PSI connection graph with one master image and only one connection between master and each child; Left: SBAS connection graph showing multiple connections for each image and two disconnected blocks.*

In the **Interferometric Process**, the interferograms between all image pairs are generated. To do so, all images are first co-registrated, i.e. they are aligned in such a way that each pixel in the child image represents the corresponding object in the master image. This is achieved by locally matching the image intensity values using a maximisation of local cross-correlation between master and child image.

After co-registration, each master image is multiplied by the complex conjugate of the child image. The phase of the resulting complex interferogram corresponds to the phase difference between master and child image. This phase difference is retained, the so-called interferometric phase. This phase has multiple contributions of which the most important ones are the different atmospheric attenuation between the two acquisitions, the topography, the so-called flat earth contribution and the deformation that occurred between the two acquisitions. Since we are only interested in the latter contribution, the others need to be cancelled out as best as possible.

The flat earth phase is the phase contribution which comes from the variation of range distance across the image due to the curvature of the earth. This contribution can be removed by using an ellipsoid in a process called interferogram flattening. The topographic phase contribution can be initially estimated using a digital elevation model (DEM) such as SRTM and the satellite orbit information. This estimate is further refined in the following steps of the workflow. Similarly, the atmospheric contribution is estimated in the following steps of the workflow.

For PSI, the Interferometric Process includes the steps coregistration, interferogram generation and interferogram flattening (which includes removal of flat earth component and topographic phase component). Contrary to “standard” InSAR processing, no spatial filtering is applied and point targets (individual objects with a strong backscatter to the sensor) are preserved.

For SBAS, the Interferometric process also includes coregistration, interferogram generation and interferogram flattening but also includes filtering of the flattened interferogram to reduce phase noise and an initial phase unwrapping (transformation of the interferometric phase from multiples of 2π to absolute values using appropriate reference points).

The next step in the SBAS workflow, **Refinement and Re-Flattening**, uses user defined reference points to correct for possible orbit inaccuracies and large-scale atmospheric influences.

In the **Inversion: First Step** an initial estimate of the model parameters (residual height and displacement information) is undertaken. In the case of PSI, the algorithm identifies a number of coherent targets (Persistent Scatterers, PS) and analyses the phase history of these targets only. Initially, only highly coherent targets are considered and their information is used to get a first estimate of the model parameters. In the case of SBAS, the input scenes are processed in whole, the residual height and displacement related information are estimated from the interferometric phases and the phase unwrapping is re-done to generate higher quality products.

In the **Inversion: Second Step** the atmospheric phase components are estimated. This step is identical for both PSI and SBAS. The atmospheric phase contributions are estimated, removed from the interferometric phase and the date-by-date displacements are estimated for all images in the stack. Finally, in the **Geocoding** step, the calculated displacement information is geocoded from SAR slant range geometry into a geographic coordinate system.

All steps are explained in detail in the document *Interferometric Stacking in SARscape Processing Guidelines*. The processing parameters are detailed in Annexure D: SARscape processing parameters.

2.4.3 Results

2.4.3.1 PSI processing

Using the SARscape PSI workflow, both orbit directions (ascending and descending) were processed. The results were combined to obtain the vertical and east-west motion component. The combined dataset contains more than 16,000 points (persistent scatterers) that are mostly concentrated in the city centre with some points found in the rural settlements surrounding the city. As expected, almost no points are found within agricultural areas. This is because these areas are mostly free of stable targets. Fig. 16 shows the average vertical ground motion velocity between October 2014 and December 2019 for the city of Faridpur obtained by the PSI multi-temporal InSAR approach. The original dataset, where each measurement location is represented by a point geometry, is converted into raster format for visualisation purposes for this report. A single pixel value in Fig. 16 is the mean displacement velocity value of all points within that raster cell. Figures showing the original PSI point dataset for selected locations can be found in chapter 2.4.3.3, in particular Fig. 21, Fig. 25, Fig. 27, Fig. 30 and Fig. 31.

Fig. 16 shows a high point density within the immediate city centre and a lower point density in the surrounding rural settlements. Agricultural areas are largely not captured by the algorithm due to a lack of suitable targets. Within the city centre, the motion patterns are diverse. Green colors correspond to points, which are stable, blue tones to points that have experienced an uplift during the observation period, and red points correspond to areas of subsidence. While large areas of the city show no ground motion within the margin of error (+/-2 mm/year), several clusters of strong deformation are also present. In particular, the campus of the Diabetic Association Medical College Hospital shows strong subsidence. Between the stadium and the Faridpur railway station, an area of slight uplift (+2 to +5 mm/year) is observed.

Outside of the city centre, a few areas of slight uplift can be found. Such as a hamlet immediately to the north of the city, as well as a few points south of the city centre, particularly around the Faridpur Engineering College and the adjacent railway station. Also south of the city centre, the area of the Faridpur Medical College shows strong subsidence rates. The most striking area of strong subsidence however is in the northeast of the project area, just outside the city centre. This area is characterised by brick factories and adjacent housing facilities for the workers. It is also bordering the Padma River.

Fig. 17 shows the average east-west ground motion for the period October 2014 to December 2019 obtained from PSI. As with the vertical geometry, and for visualisation purposes, the dataset was rasterized such that every image pixel represents the mean value (mean deformation velocity) of all points located within the raster cell. Most points fall within the error margin of +/-2 mm/year and can be considered stable over the observation period (October 2014 to December 2019). Areas of positive East-West ground motion are found southwest of the city centre and in the area north of the stadium, an area that also experiences a slight uplift (see Fig. 16).

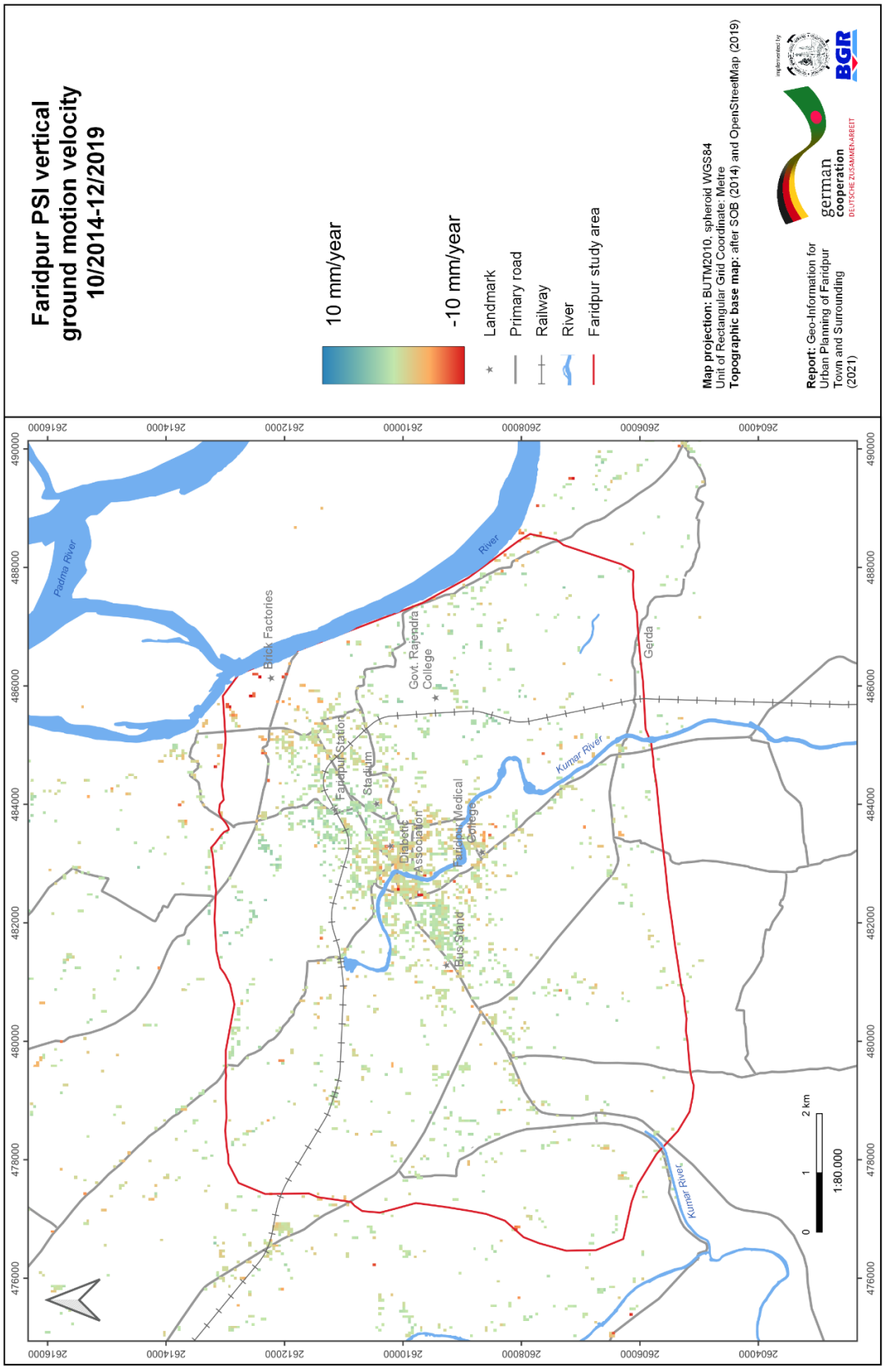

Figure 16: *PSI vertical ground motion component.*

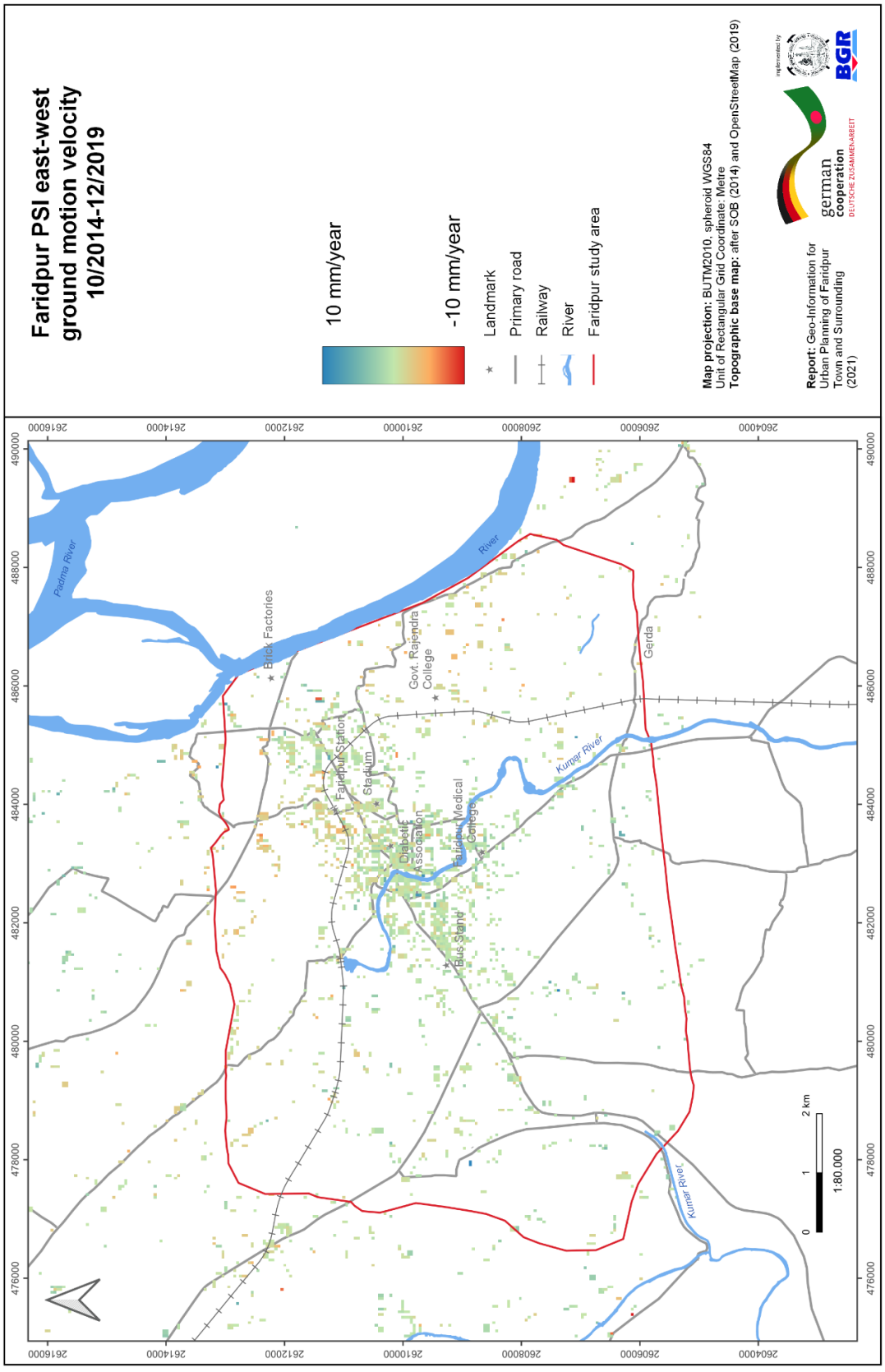

Figure 17: *PSI east-west ground motion component.*

2.4.3.2 SBAS

SBAS results are obtained using the SBAS workflow within the SARscape software. As with PSI, both orbit directions are processed separately and then merged to obtain the vertical and east-west motion components. The resulting dataset is notably denser than the PSI dataset. Using SBAS, information is obtained in areas where the PSI method failed to deliver results or PSI point density is low. However, the dataset is showing gaps in areas that are subject to strong changes over time, such as agricultural areas.

Fig. 18 shows the average vertical ground motion velocity in Faridpur for the period October 2014 to December 2019 obtained from the SBAS method. Overall, the results seem to match well with the PSI results. Large parts of the city and its surrounding areas fall within the error margin and can be considered stable during the observation period. The SBAS analysis further reveals several clusters of strong subsidence to the east of the city centre where there has been a lot of construction activity. It also reveals large clusters of strong subsidence west of the city centre around the Faridpur Bus Stand and the Faridpur Housing Society where the coverage of the PSI analysis is low. Both areas contain many recently built structures as can be seen from current and historical satellite images.

Overall, the SBAS dataset makes it easier to detect large-scale deformation patterns. As with PSI, the largest cluster of strong subsidence corresponds to the area northeast of the city centre, which is characterised by brick factories. The Faridpur Medical College campus forms another larger cluster of strong subsidence rates that is also found in the PSI analysis. While the coverage outside of the city centre is larger using SBAS than using PSI, the small-scale motion patterns of the PSI result within the city centre and on individual buildings are lost.

Fig. 19 shows the average east-west ground motion velocity in Faridpur for the period October 2014 to December 2019 obtained from the SBAS processing. Areas of higher negative east-west motion are found in the northeast and the southwest of the project area. The largest part of the project area can be considered stable.

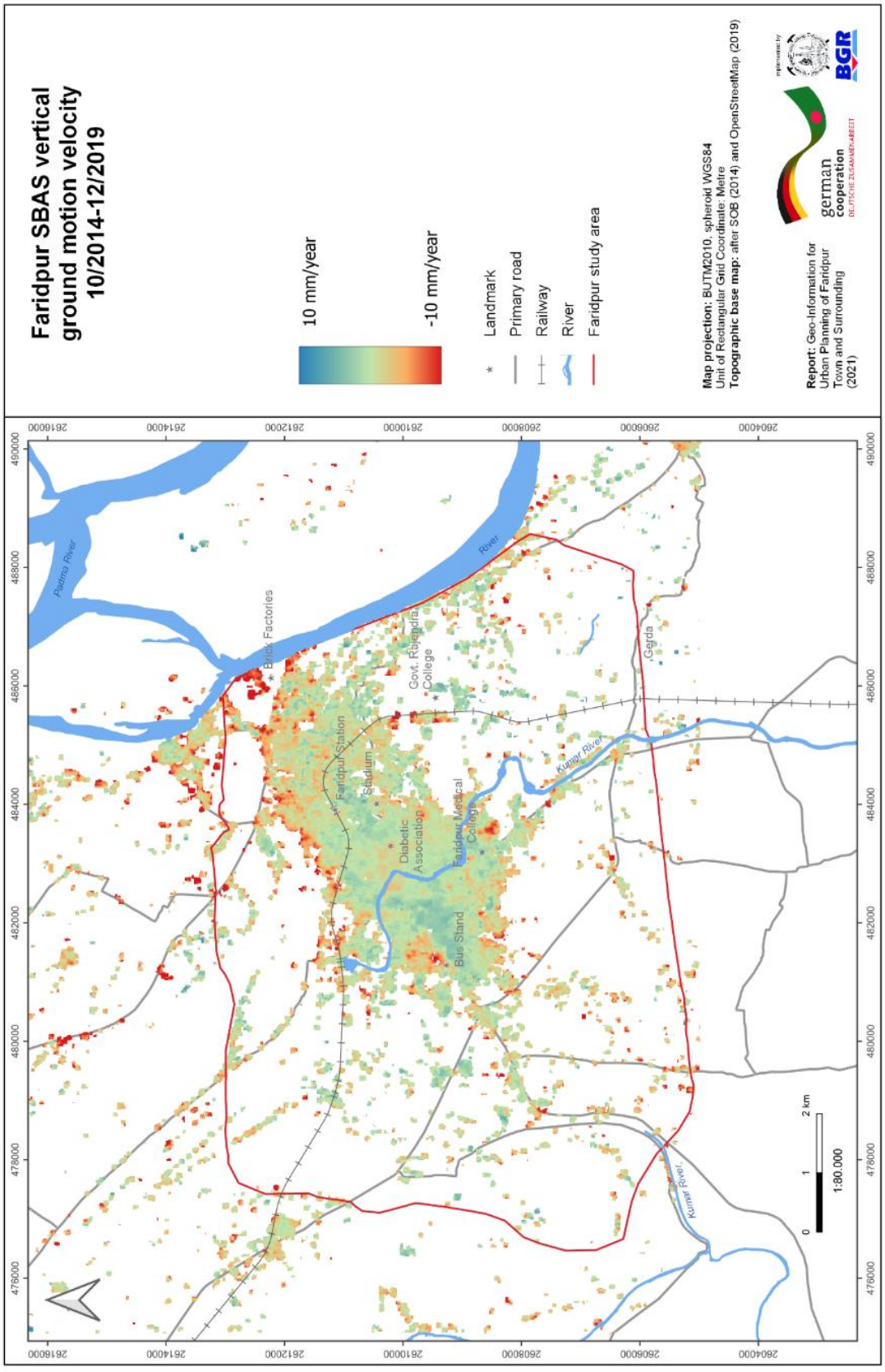

Figure 18: *PSI vertical ground motion component.*

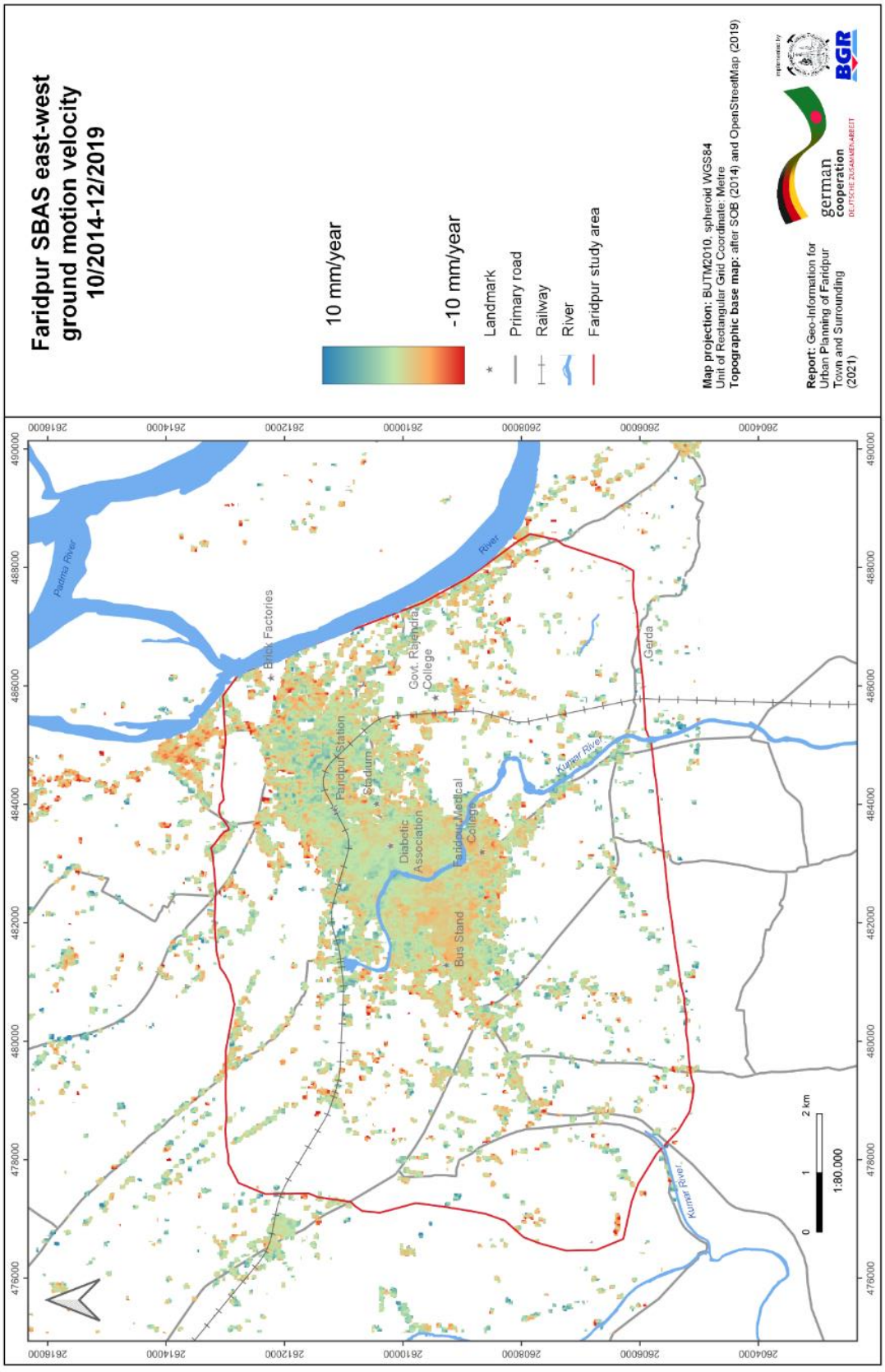

Figure 19: *PSI east-west ground motion component.*

2.4.3.3 Comparison of PSI and SBAS results

When comparing both datasets, it is immediately evident that SBAS achieves a higher spatial coverage than PSI. The difference is particularly striking in areas outside of the city centre. This is due to the ability of the SBAS approach to deal with so-called distributed scatterers (DS) like open fields, rocks and other geometrically not well-defined objects. The SARscape implementation of the SBAS algorithm is also able to handle objects that are affected by low coherence or even coherence loss for some parts of the observation period.

On a visual inspection, there seems to be good agreement between the two vertical motion datasets in terms of the general ground motion trends. Where there is coverage in both the SBAS and PSI data, generally both show similar trends. Both datasets reveal that most of the project area can be considered stable within the margin of error (+/-2 mm/year) or moving only slightly. Within the project area, the largest observed vertical motion rates are -23.60 mm/year and +9.76 mm/year for the SBAS dataset and -13.63 mm/year and +3.98 mm/year for the PSI dataset. In the east-west direction, the values are -19.60 mm/year and +17.03 mm/year for the SBAS dataset and -18.13 mm/year and +11.40 mm/year for the PSI dataset respectively (see Tab. 11). Slightly different deformation values are expected since both methods use different reference points for the phase unwrapping. The Pearson Correlation Coefficient is +0.43 for the two vertical datasets, indicating a moderate positive correlation and +0.11 for the east-west datasets, indicating only a small correlation. However, it needs to be considered that due to the spatial averaging applied in the SBAS workflow, the spatial relationship between both datasets is not necessarily straightforward (compare also Fig. 27).

Table 11: *Basic statistics for PSI and SBAS datasets.*

Dataset	Minimum velocity [mm/year]	Maximum velocity [mm/year]	Mean [mm/year]	Standard Deviation [mm/year]
PSI vertical	-13.63	+3.98	-0.63	+1.76
SBAS vertical	-23.60	+9.76	-1.19	+2.91
PSI east-west	-18.13	+11.40	+0.13	+1.75
SBAS east-west	-19.60	+17.03	-0.81	+2.64

The points of strong vertical deformation in the PSI datasets correspond to a high-rise in the city centre of Faridpur (23.6011N, 89.8291E), the Diabetic Association Medical College Hospital (23.6062N, 89.8362E, see also Fig. 25 and Fig. 26) and the area surrounding the brick factories in the northeast of the project area (see Fig. 21 and Fig. 22). Points of uplift are clustered around the Faridpur Railway Station. In the SBAS dataset, the points of strongest subsidence correspond to points in the northeast of the project area (see Fig. 21 and Fig. 22). The points of strongest uplift are found in the south of the project area near the College railway station and the Faridpur Engineering College.

In the following, a few points of interest and their respective vertical motion time series are presented to illustrate the relationship between both methods and exemplify their respective strengths and limitations. Fig. 21 shows the vertical velocity for both methods around the brick factories in the northeast of Faridpur. Fig. 22 shows the displacement time series for a house in the adjacent worker's settlement. While the overall motion trends for both methods seen in Fig. 21 are in good agreement with each other, the displacement time series – while showing the same negative trend – show different displacement magnitudes. While the PSI algorithm has calculated a cumulative displacement for this point over the observation period of around -40 mm, the SBAS algorithm has calculated a displacement of roughly -80 mm i.e. double the displacement. Interestingly, the SBAS time series shows two features that cannot be found in the PSI time series: Firstly, between January and November 2015 the time series shows a value jump resulting in approximately -40 mm of accumulated displacement. Secondly, cyclical patterns that may be related to seasonal influences are present in the data. The magnitude of the value jump corresponds - more or less - to the total observed difference between PSI and SBAS for that point. The PSI algorithm is not able to detect these types of very strong non-linear displacements. Instead, it tries to fit the data onto a linear model while SBAS is also able to deal with non-linearities.

Fig. 25 is a comparison of both datasets in the city centre of Faridpur. Here, the strengths of the PSI algorithm are clearly visible: While SBAS achieves a denser spatial coverage, the PSI results give a much more detailed picture. It is possible to identify individual buildings and on larger buildings and structures, often several points are available, allowing the detection of different displacement rates for different parts of a building. From the PSI data, it also becomes clear that the motion patterns within the

city centre are much more heterogeneous than suggested by the SBAS data. The comparison between both subfigures illustrates well the fact that SBAS is assuming a spatial correlation of the observed deformation phenomena while PSI is well suited to analyse uncorrelated motions.

The Faridpur Diabetic Association Hospital is visible in the centre of Fig. 25 a) and b) as a cluster of relatively strong deformation. The hospital main building is a 15-storey high-rise, the highest building in Faridpur. Until 2006 the building had only five floors and since then ten more floors have been added. A number of active construction sites surrounds the building. Fig. 26 is a comparison of the vertical motion time series of both methods for a point on the hospital main building. The SBAS time series shows strong subsidence until around October 2015 and a subsequent stabilisation while the PSI time series follows a clear negative trend throughout the observation period. The cumulative displacement over the observation period is -25 mm for SBAS and -62 mm for PSI. As in the previous example, both methods agree on the direction of the observed motion but differ in the estimated magnitude. A possible explanation for the stabilisation of the SBAS time series could be linked to the fact that SBAS applies spatial averaging of adjacent pixels. The SBAS signal is therefore a mixed signal showing the more large-scale trends on the hospital campus.

Another point of interest is the Faridpur Medical College campus in the south of the city (Fig. 27). The Medical College campus has recently undergone a large-scale extension with the construction of new accommodation for students, a mosque and a new main building (between 2007 and 2014). As recently as 2019, construction activity on the campus was still ongoing. PSI requires points that fulfil relatively high coherence thresholds throughout the observation period. If buildings are altered during the observation, points lying on these structures may be lost for a PSI analysis. SBAS however is able to deal with points that are affected by a temporary loss of coherence. Both InSAR datasets show high negative vertical deformation velocities over the campus area (Fig. 27). Fig. 28 is a plot of the vertical deformation time series over the main building of the campus. While the PSI time series shows a strong negative deformation trend (-40 mm in ~5 years), the SBAS time series appears to be relatively stable. This is due to the fact that the centre of deformation for the SBAS data is located a little south of the main building while in the PSI dataset it is located directly on the main building.

When we plot an SBAS point just south of the main building (Fig. 29) both time series now look very similar. The PSI dataset also reveals that parts of the Medical College main building are subsiding at different rates.

Figure 20: *Construction in progress on the Faridpur Medical College campus.*

Fig. 30 shows the different spatial coverage achieved by both methods outside of the city centre around the Faridpur Engineering College and the adjacent railway station. PSI spatial coverage in this area is very low while SBAS achieves a higher spatial coverage. Agricultural fields are not captured by either method. Fig. 31 shows vertical ground motion patterns in the west of the city centre. Again, the SBAS spatial coverage is very high while PSI achieves only punctual results. Interestingly enough, the area seems to feature a high number of potential persistent scatterers (such as high-rise buildings) that were not captured by the PS algorithm. This could be an indicator that these buildings were constructed only recently (during the observation period) and therefore were not continuously coherent throughout the observation period. SBAS has less stringent coherency requirements and can also deal with points that are affected by a temporary decrease or loss of coherence (see 4.2.0). The area where the PSI dataset is empty corresponds to a large deformation cluster in the SBAS dataset. It is possible, that the observed deformation is a result of the building load of the newly built structures.

The east-west datasets show less agreement than the vertical datasets. The Pearson correlation between the horizontal PSI and SBAS datasets is only +0.11 and the mean values show different directions (positive mean east-west movement in the PSI dataset vs. negative mean east-west movement in the SBAS dataset), albeit with a very small difference of less than 1mm/year. Nonetheless, both datasets show little to no horizontal movement within the project area overall considering the uncertainty attached to both methods, which is estimated to be +/- 2mm/year.

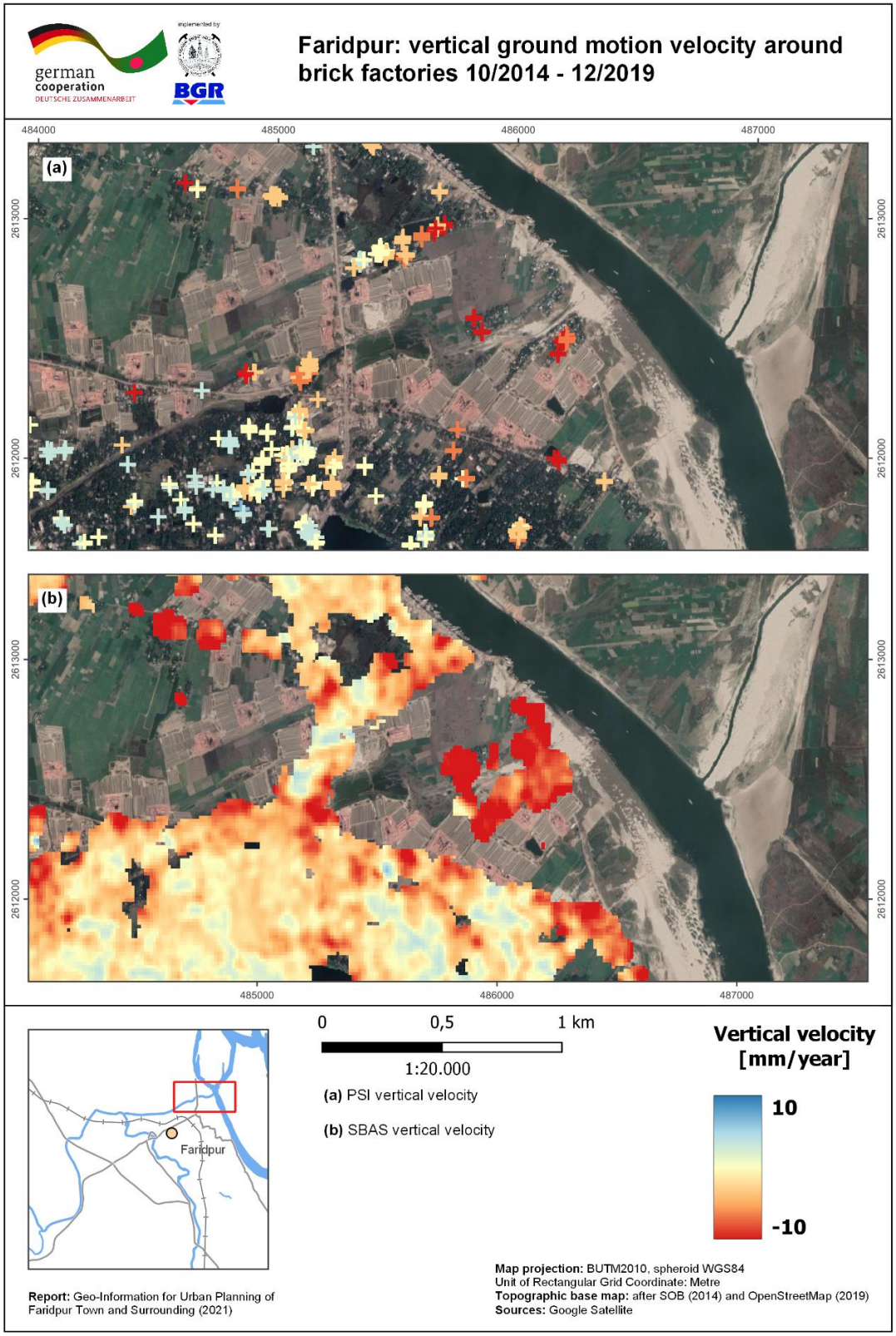

Figure 21: *Vertical velocity around brick factories for PSI and SBAS.*

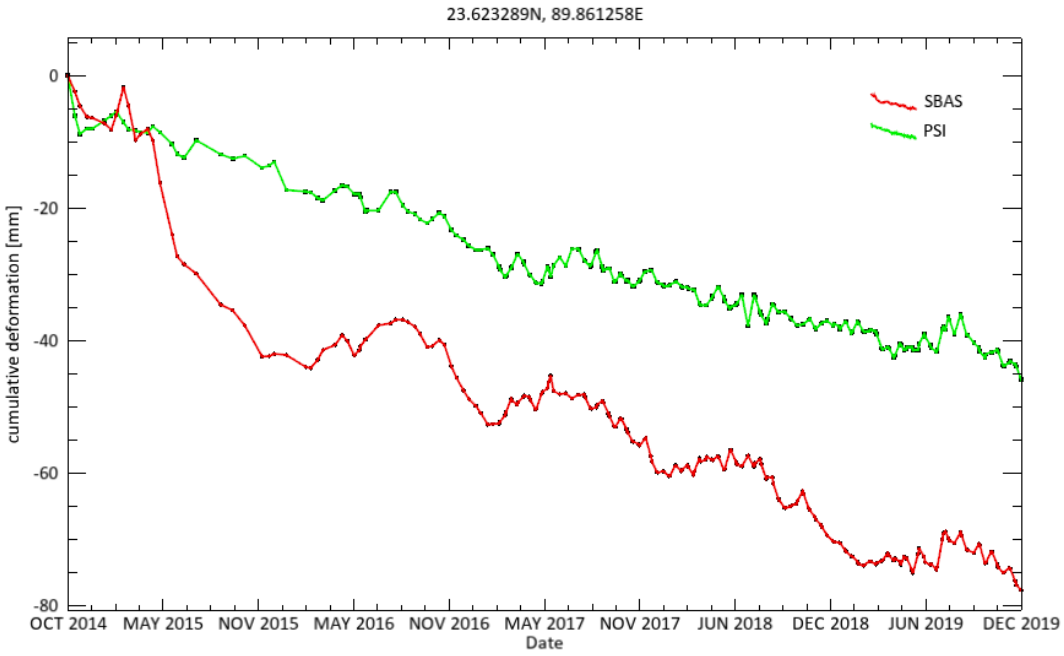

Figure 22: *Comparison of PS and SBAS vertical deformation time series for brick factory worker's housing.*

Figure 23: *Brick factories in the northeast of the project area.*

Figure 24: *Residential neighbourhood adjacent to brick factories is showing strong subsidence.*

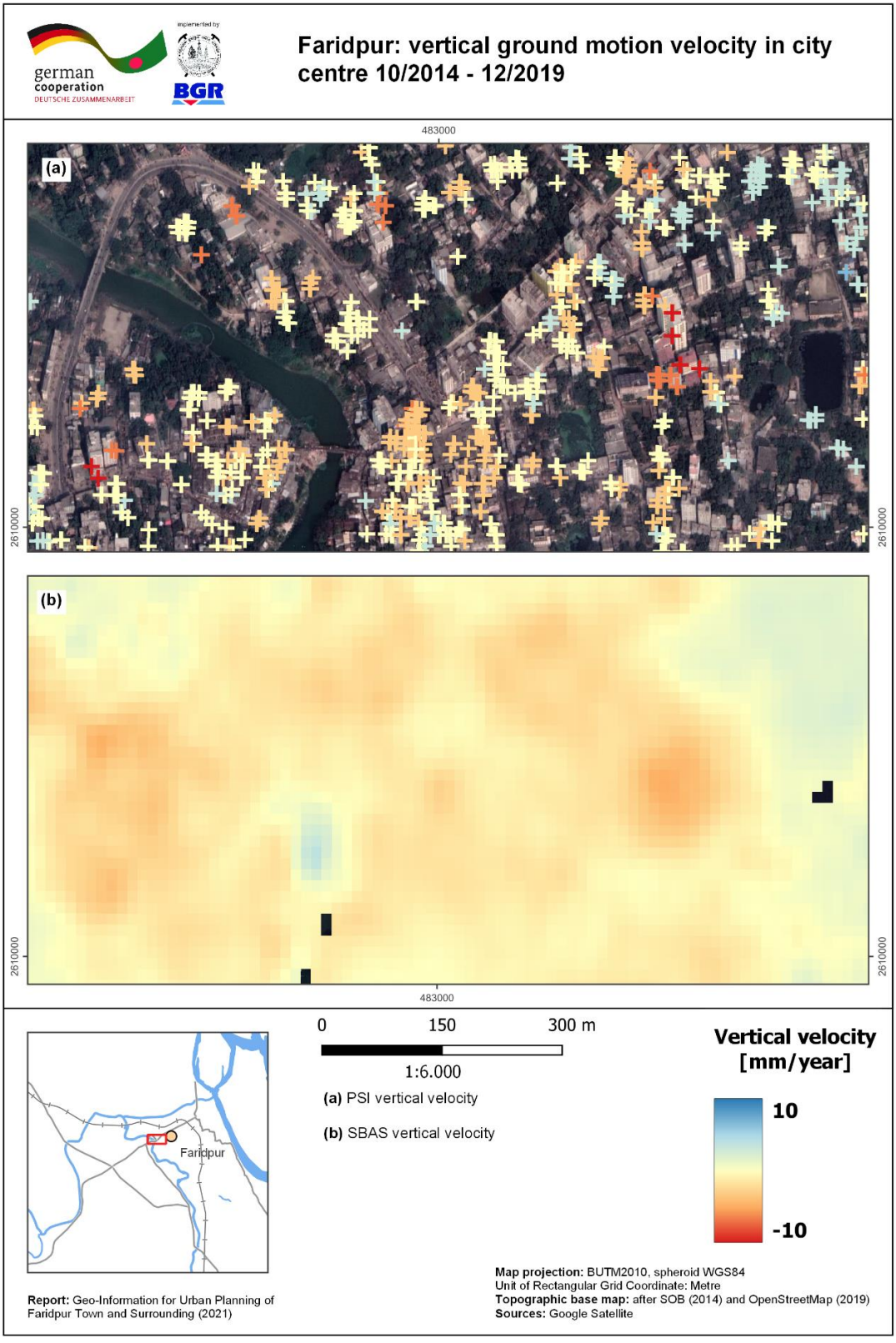

Figure 25: *Comparison of PSI and SBAS vertical motion in the city centre.*

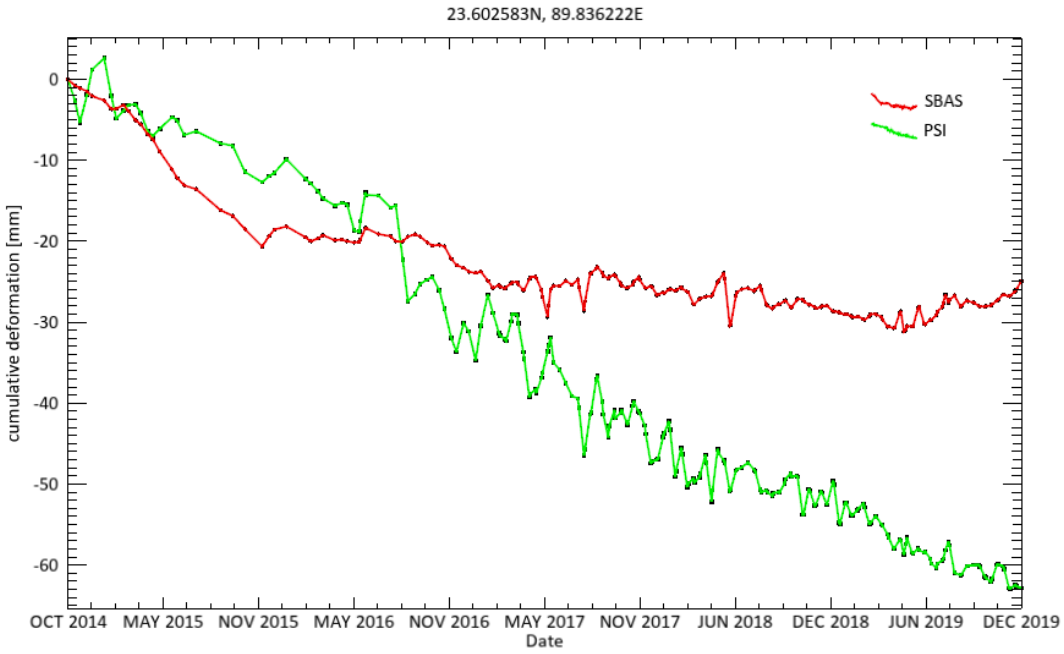

Figure 26: *PSI and SBAS vertical motion time series for Faridpur Diabetic Association Medical Hospital.*

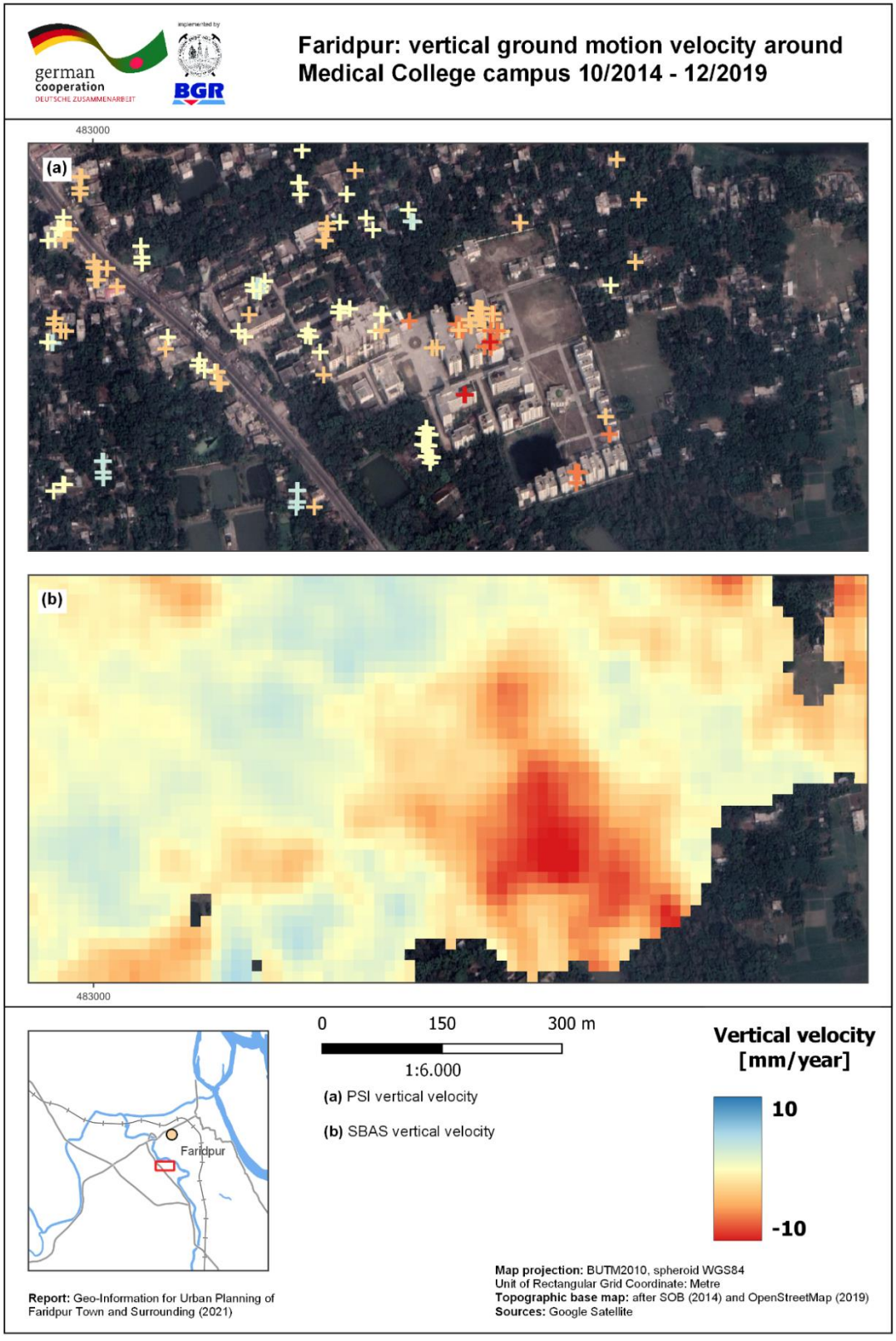

Figure 27: *Comparison of PSI and SBAS vertical motion over Faridpur Medical College Campus.*

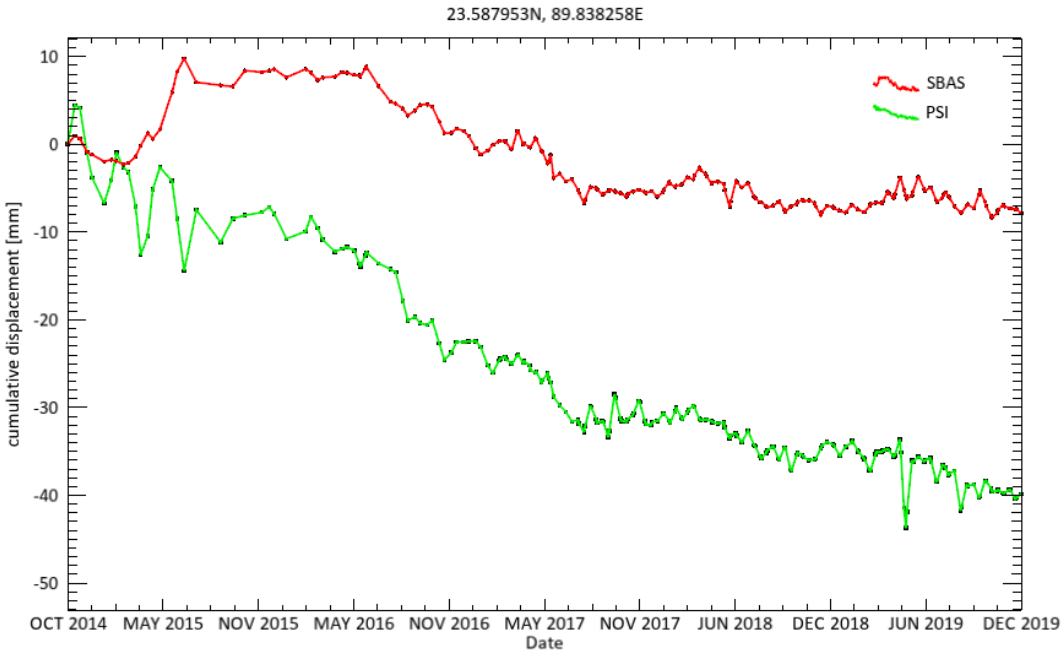

Figure 28: *SBAS and PSI vertical motion time series for Medical College main building.*

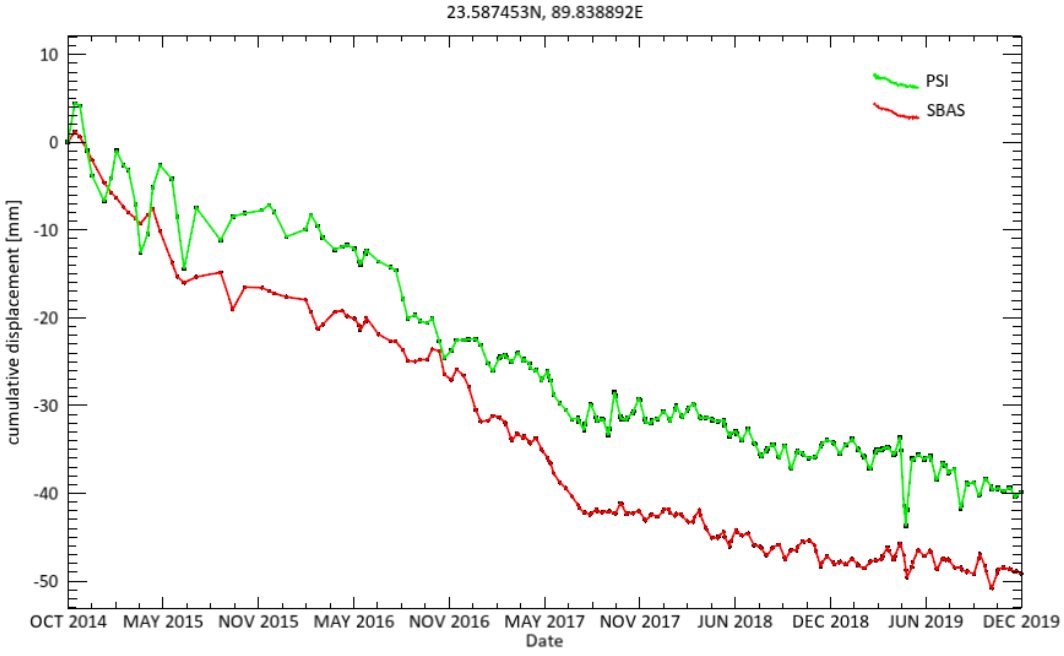

Figure 29: *Vertical motion for Medical College main building (PSI) and Medical College mosque (SBAS).*

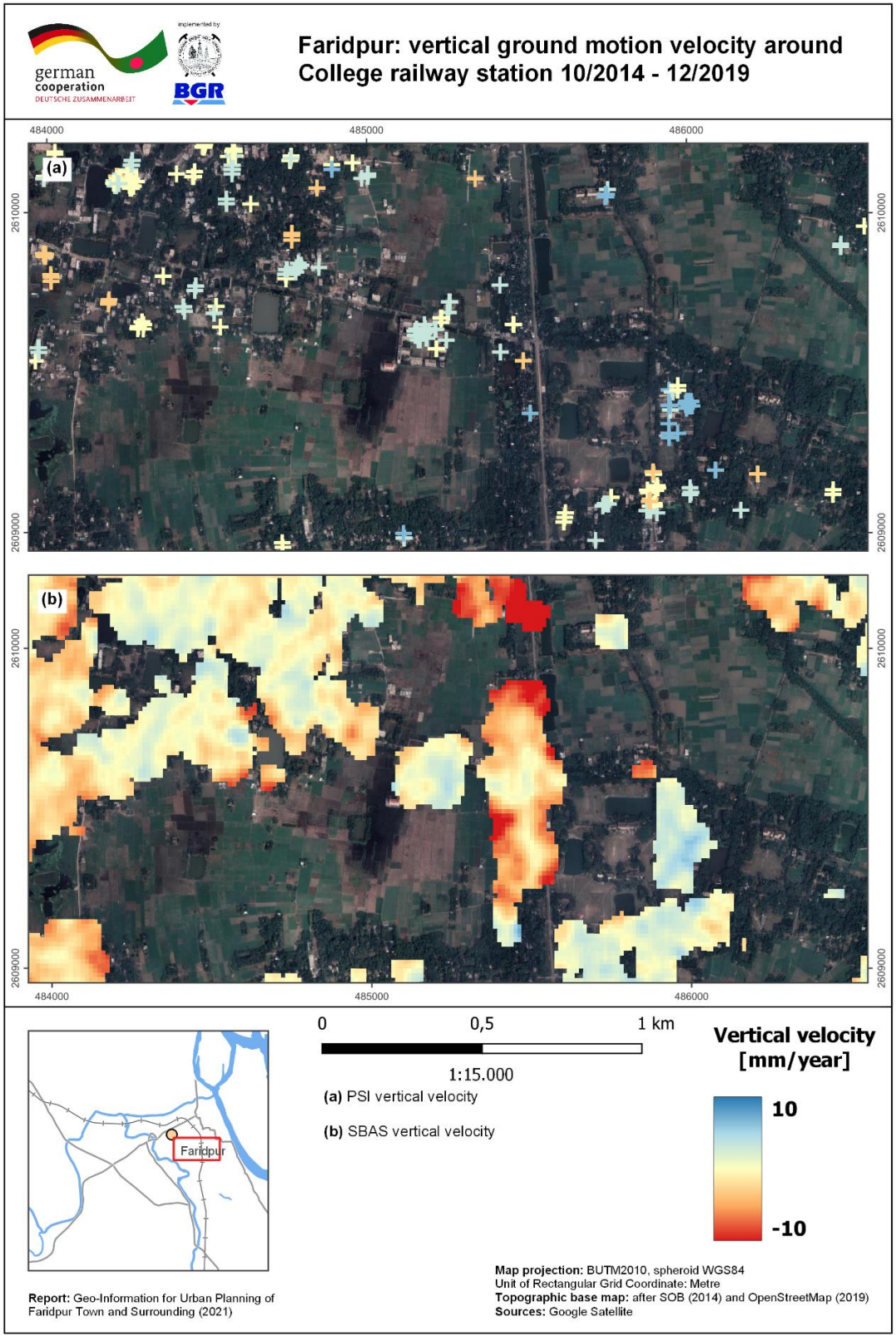

Figure 30: *Comparison of PSI and SBAS vertical motion over College railway station and Faridpur Engineering College campus.*

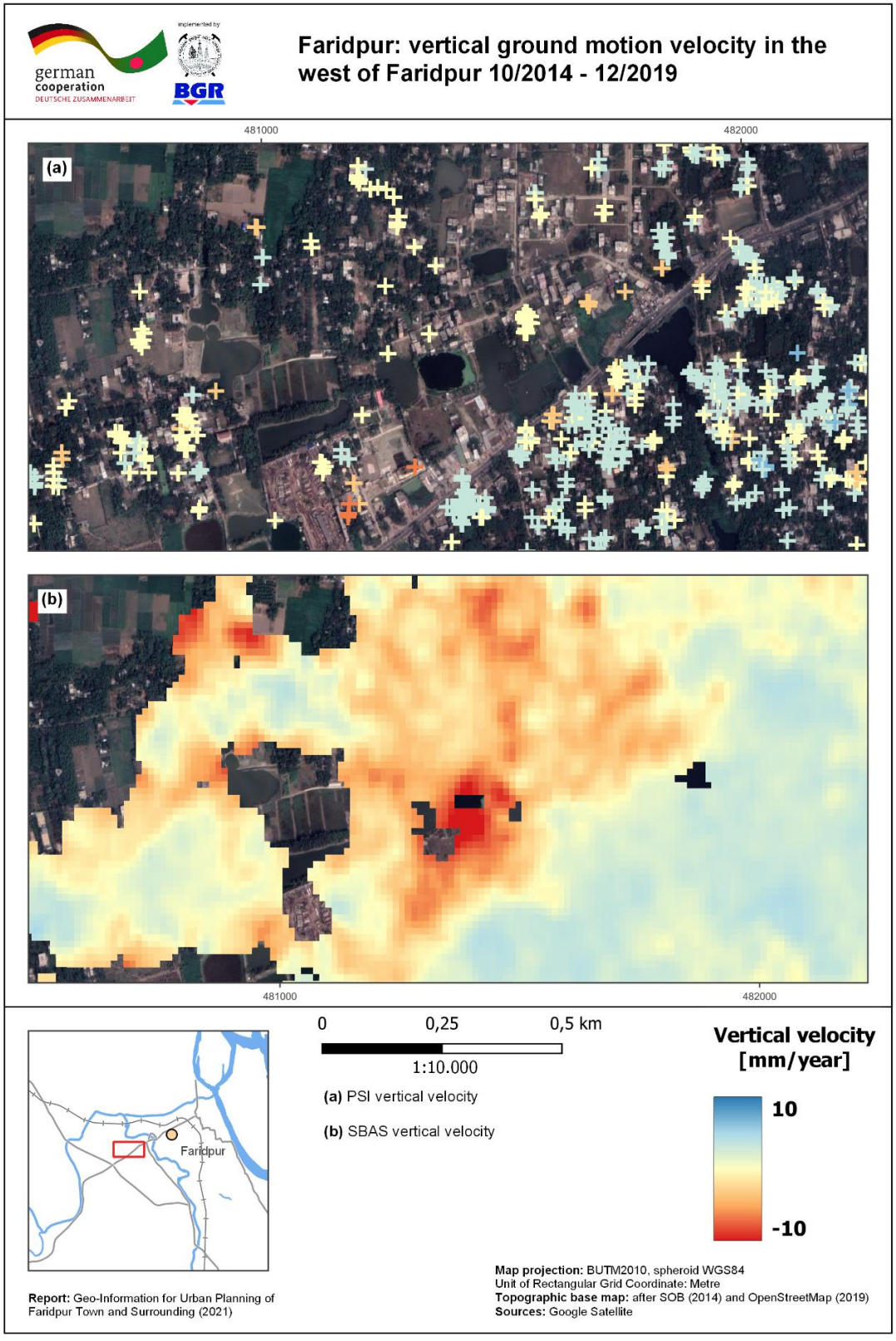

Figure 31: *Comparison of PSI and SBAS vertical motion west of city centre.*

2.4.4 Conclusions

Overall, both methods lead to similar results in both the vertical and horizontal direction, which is an indicator to the validity of the results. In the horizontal direction the correlation between PSI and SBAS is less than in the vertical direction but both horizontal datasets show little to no movement in the project area. Both vertical datasets (PSI and SBAS) mostly agree in the observed ground motion patterns in areas where data from both processing methods are available. SBAS achieves a higher spatial coverage at the cost of spatial resolution, whereas PSI delivers only punctual information but with high accuracy and spatial resolution. Within the urban core of the project area however, both methods lead to a similar spatial coverage. Overall, both datasets show, that there are no strong large-scale vertical movements within the project area but only punctual clusters of subsidence.

Strong subsidence can be observed around the brick factories near the Padma River and the Faridpur Medical College in the south of the city. On top of that, PSI reveals several clusters of strong subsidence within the city centre, while SBAS reveals strong subsidence west of the city centre in an area, where PS coverage is low.

It is expected that a number of factors contribute to the observed ground motion patterns and trends. Many of the observed subsidence clusters seem to be related to structures that were recently built or recently enlarged. Here, the building load of these structures seems to play a role. From other project areas, it is also known that there is a link between the local geomorphology and ground motion. In particular, it could be shown in other project areas that constructions in floodplains are more likely to be affected by strong subsidence while constructions on natural levees tend to be more stable. The role of changes in groundwater levels and seasonal weather patterns on local ground motion is beyond the scope of this report. A link seems likely but more work needs to be done to confirm this suspicion.

Both methods provide huge amounts of measurement points that are spatially and temporarily dense and can be acquired extremely fast and cost-efficiently when compared to other geodetic methods such as levelling or GPS/GNSS (though permanent GPS stations achieve a higher accuracy and temporal density, they provide only punctual measurements). Both methods work particularly well in urban environments where there is a large amount of high coherent targets, while SBAS also performs well in more suburban or even rural environments. These two facts highlight the immense value of multi-temporal InSAR for urban planning.

Each of the two methods used within this work has its unique strengths and possible areas of application within urban planning. While SBAS enables a denser spatial coverage and the detection of large-scale motion trends related to large infrastructure, PSI enables a more detailed analysis of singular buildings, bridges and roads. On large buildings, we can often find several persistent scatterers, thus PSI can be used to detect different displacement rates for different parts of a building. PSI is also expected to be slightly more accurate than SBAS (PASQUALI ET AL. 2014, p. 236).

Both PSI and SBAS allow the extraction of ground motion information from satellite data with millimetre accuracy and at a high temporal resolution using freely available Sentinel-1 data. Due to the unique characteristics of each method, both methods complement each other well. For absolute ground motion data, external data needs to be used as reference (e.g. GPS/GNSS data from fixed stations).

2.4.5 Recommendations

Multi-temporal InSAR can be used in urban planning to detect stable areas that are potentially suited as building ground. The combined analysis of InSAR and ancillary data (in particular geological, geomorphological, hydrological and land use data) possibly enables the detection of links and causalities for observed ground motion patterns. Furthermore, multi-temporal InSAR can also serve as a tool for the monitoring of existing infrastructure and buildings.

Two of the most commonly used methods in this field are Persistent Scatterer Interferometry (PSI) and Small Baseline Subset (SBAS). Overall, both methods have their unique strengths and complement each other well. SBAS provides an overview over the large-scale motion patterns within a study area while PSI enables a more detailed analysis of specific points of interest.

A possible constraint to be considered is the computational effort required. While both methods have high computational demands, SBAS is much more computationally intensive for the same data since the number of interferograms created is usually significantly larger than the number of input images. For PSI, the number of interferograms is N-1. Finally, a precondition for the use of any InSAR technique is the existence of enough coherent targets within the area of interest and over the observation period. In areas with seasonal flooding, the use of artificial targets such as corner reflectors or active transponders should be considered.

Where other ground motion data for example from GPS fixed stations or continuous levelling campaigns is available, this data can and should be used as reference for the InSAR results. While different studies have shown that both PSI and SBAS deliver high quality results much depends on the number of acquisitions used. To properly isolate phase influences due to atmosphere and topography from the actual deformation a large number of acqusitions should be used. In general, the more acquisitions are used, the better the results.

References

BANGLADESH WATER DEVELOPMENT BOARD (2017): Annual Flood Report 2017. – <http://www.ffwc.gov.bd/images/annual17.pdf>. (Last access: 19.02.2021).

BANGLADESH WATER DEVELOPMENT BOARD (2018): Annual Flood Report 2018. – <http://www.ffwc.gov.bd/images/annual18.pdf>. (Last access: 16.12.2020).

BANGLADESH WATER DEVELOPMENT BOARD (2019): Annual Flood Report 2019. – <http://www.ffwc.gov.bd/images/annual19.pdf>. (Last access: 19.02.2021).

BERARDINO, P., FORNARO, G., LANARI, R., SANSOSTI, E. (2002): A New Algorithm for Surface Deformation Monitoring Based on Small Baseline Differential SAR Interferograms, IEEE Transactions on Geoscience and Remote Sensing, vol. 40, no. 11, pp. 2375- 2383.

CHAMBELL J. B. (1996): Introduction to Remote Sensing. 2nd edition. Taylor & Francis. London.

CHAVEZ, P. S. (1996): Image-Based Atmospheric Corrections - Revisited and Improved. Photogrammetric Engineering and Remote Sensing. Vol. 62. No. 9. 1025-1036.

CONGEDO, L. (2016): Semi-Automatic Classification Plugin Documentation. – <http://dx.doi.org/10.13140/RG.2.2.29474.02242/1>. (Last change: n.d.). (Last access: 08.08.2019).

CROSETTO, M., MONSERRAT, O., CUEVAS-GONZÁLEZ, M., DEVANTHÉRY, N., CRIPPA, B. (2016): Persistent Scatterer Interferometry: A review, ISPRS Journal of Photogrammetry and Remote Sensing, vol. 115, pp. 78-89.

EUROPEAN ENVIRONMENT AGENCY (2017): Copernicus Land Service – Pan-European Component: CORINE Land Cover. <https://land.copernicus.eu/user-corner/publications/clc-flyer/at_download/file>. (Last change: n.d.). (Last access: 22.01.2021).

EUROPEAN ENVIRONMENT AGENCY (2019): Updated CLC illustrated nomenclature guidelines. - <https://land.copernicus.eu/user-corner/technical-library/corine-land-cover-nomenclature-guidelines/docs/pdf/CLC2018_Nomenclature_illustrated_guide_20190510.pdf>. (Last change: n.d.). (Last access: 22.01.2021).

EUROPEAN SPACE AGENCY (2017): Sentinel-2 Spectral Response Functions (S2-SRF). – <https://earth.esa.int/web/sentinel/user-guides/sentinel-2-msi/document-library/-/asset_publisher/Wk0TKajiISaR/content/sentinel-2a-spectral-responses>. (Last change: 19.12.2017). (Last access: 13.06.2019).

EUROPEAN SPACE AGENCY (2019): Sen2Cor Configuration and User Manual V2.8. – <http://step.esa.int/thirdparties/sen2cor/2.8.0/docs/S2-PDGS-MPC-L2A-SUM-V2.8.pdf>. (Last change: 05.02.2019). (Last access: 22.08.2019).

EUROPEAN SPACE AGENCY (2020): Sentinel-1 User Guide: Interferometric Wide Swath. <https://sentinel.esa.int/web/sentinel/user-guides/sentinel-1-sar/acquisition-modes/interferometric-wide-swath>. (Last change: n.d.). (Last access: 16.12.2020).

Ferretti, A., Prati, C., Rocca, F. (2001): Permanent Scatterers in SAR Interferometry, IEEE Transactions on Geoscience and Remote Sensing, vol. 39, no. 1, pp. 8-20.

FORNARO, G., PASCAZIO, V. (2014): Chapter 20 - SAR Interferometry and Tomography: Theory and Applications. Academic Press Library in Signal Processing. Vol. 2. 1043-1117. doi: 10.1016/B978-0-12-396500-4.00020-X.

GOOGLE EARTH ENGINE DATA CATALOG (2020): Sentinel-1 SAR GRD: C-band Synthetic Aperture Radar Ground Range Detected, log scaling. – <https://developers.google.com/earth-engine/datasets/catalog/COPERNICUS_S1_GRD>. (Last change: n.d.). (Last Access: 16.12.2020).

JONES, H. G. AND VAUGHAN, R. A. (2010): Remote Sensing of Vegetation – Principles, Techniques, and Applications. Oxford University Press.

KALIA, A., C., FREI, M., LEGE, T., (2020): BodenBewegungsdienst Deutschland - BBD, Projektbericht, Version 1, 133 S., Bundesanstalt für Geowissenschaften und Rohstoffe (BGR), Hannover, unpublished.

LILLESAND, T. M., KIEFER, W., CHIPMAN, J. W. (2015): Remote Sensing and Image Interpretation. Seventh Edition. Wiley.

López-Martínez, C., Fàbregas, X. and Pottier, E. (2004): A new alternative for SAR imagery coherence estimation. Proc. EUSAR Conf., Ulm, Germany.

MCFEETERS, S. K. (1996): The use of the Normalized Difference Water Index (NDWI) in the delineation of open water features. International Journal of Remote Sensing. Vol. 17. No. 7. 1425-1432.

MOREIRA, A., PRATS-IRAOLA, P., YOUNIS, M., KRIEGER, G., HAJNSEK, I., AND PAPATHANASSIOU, K. P. (2013): A tutorial on synthetic aperture radar. In: IEEE Geoscience and Remote Sensing Magazine. Vol. 1, No. 1. 6-43. doi: 10.1109/MGRS.2013.2248301.

MUELLER-WILM, U., DEVIGNOT, O., PESSIOT, L. (2018): Level 2A Input Output Data Definition (IODD) v2.5.5. –

<https://step.esa.int/thirdparties/sen2cor/2.5.5/docs/S2-PDGS-MPC-L2A-IODD-V2.5.5.pdf>. (Last change: 23.03.2018) (Last access: 20.05.2019).

PASQUALI, P., CANTONE, A., RICCARDI, P., DEFILIPPI, M., OGUSHI, F., GAGLIANO, S. AND TAMURA, M. (2014): Mapping of Ground Deformations with Interferometric Stacking Techniques, in Land Applications of Radar Remote Sensing, InTech.

PRASAD S., BRUCE L. M., CHANUSSOT J. (2011): Introduction. Optical Remote Sensing. Augmented Vision and Reality, Vol. 3. Springer. Berlin, Heidelberg.

Rencz A. N. (1999): Manual of Remote Sensing. 3rd edition, Vol. 3. Remote Sensing for the Earth Sciences. John Wiley & Sons.

RICHARDS, J. A. (2009): Remote Sensing with Imaging Radar. Springer-Verlag. Berlin, Heidelberg.

RICHARDS, J. A. (2013): Remote Sensing Digital Image Analysis – An Introduction. 5th edition. Springer. Heidelberg. New York. Dordrecht. London.

SABINS F. F. (1996): Remote Sensing. 3rd edition. Freemann and Company. New York.

UNITED STATES GEOLOGICAL SURVEY (n.d.): What are the band designations for the Landsat satellites? – <https://www.usgs.gov/faqs/what-are-band-designations-landsat-satellites>. (Last change: n.d.). (Last access: 13.06.2019).

UNITED STATES GEOLOGICAL SURVEY (2020): Landsat 4-7 Surface Reflectance (LEDAPS) Product Guide. Version 3.0. August 2020. – <https://prd-wret.s3.us-west-2.amazonaws.com/assets/palladium/production/atoms/files/LSDS-1370_L4-7_C1-SurfaceReflectance-LEDAPS_ProductGuide-v3.pdf>. (Last change: August 2020). (Last access: 02.11.2020).

USTIN S. L. (2004): Manual of Remote Sensing. 3rd edition, Vol. 4. Remote Sensing for Natural Resource Management and Environmental Monitoring. John Wiley & Sons.

WOODHOUSE, I. H. (2006): Introduction to Microwave Remote Sensing. 1st edition. CRC Press. Boca Raton.

Annexure A: Maps

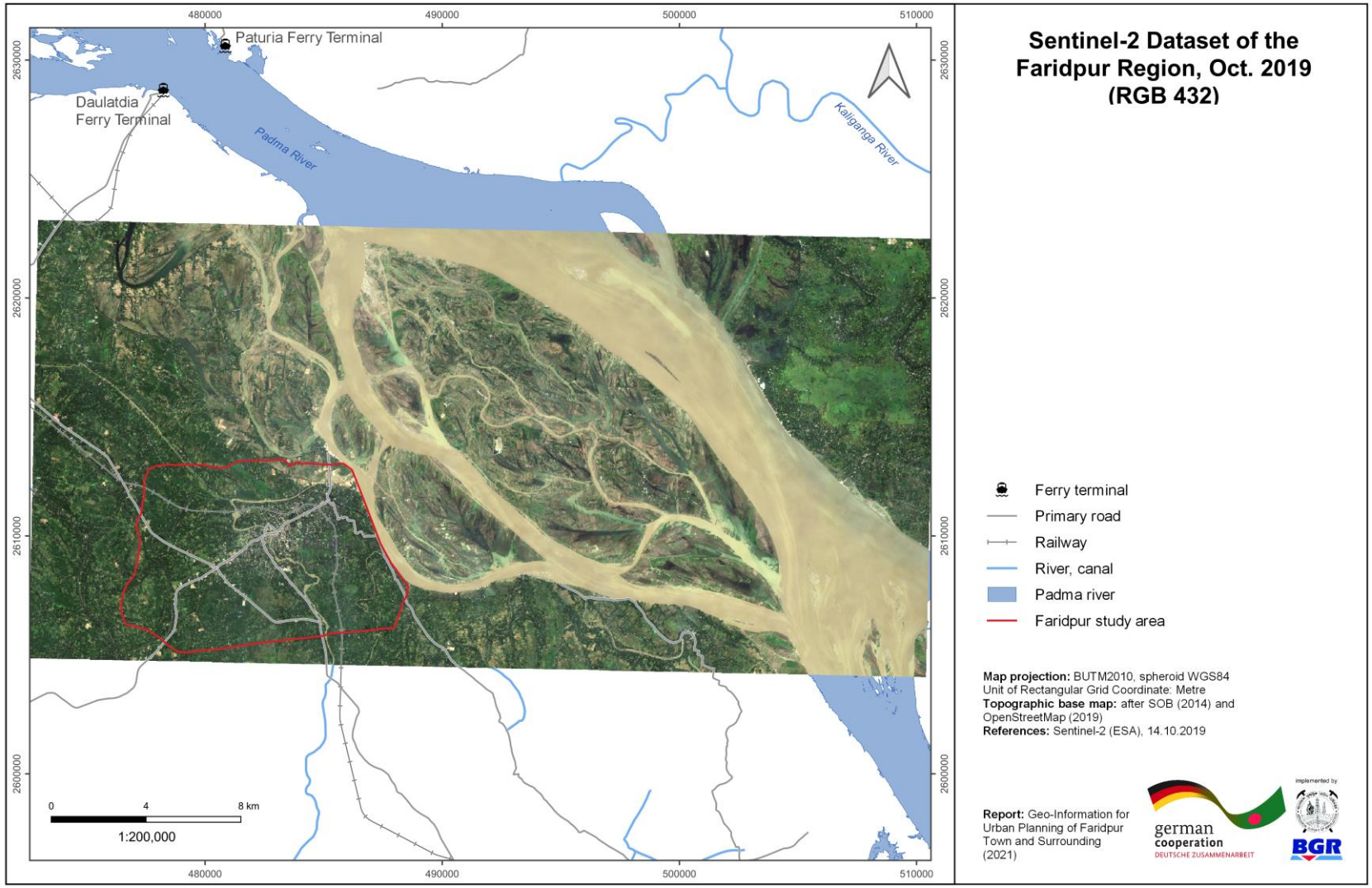

Figure A1: *Sentinel-2 Dataset of the Faridpur Region, 14.10.2019 (RGB 4-3-2).*

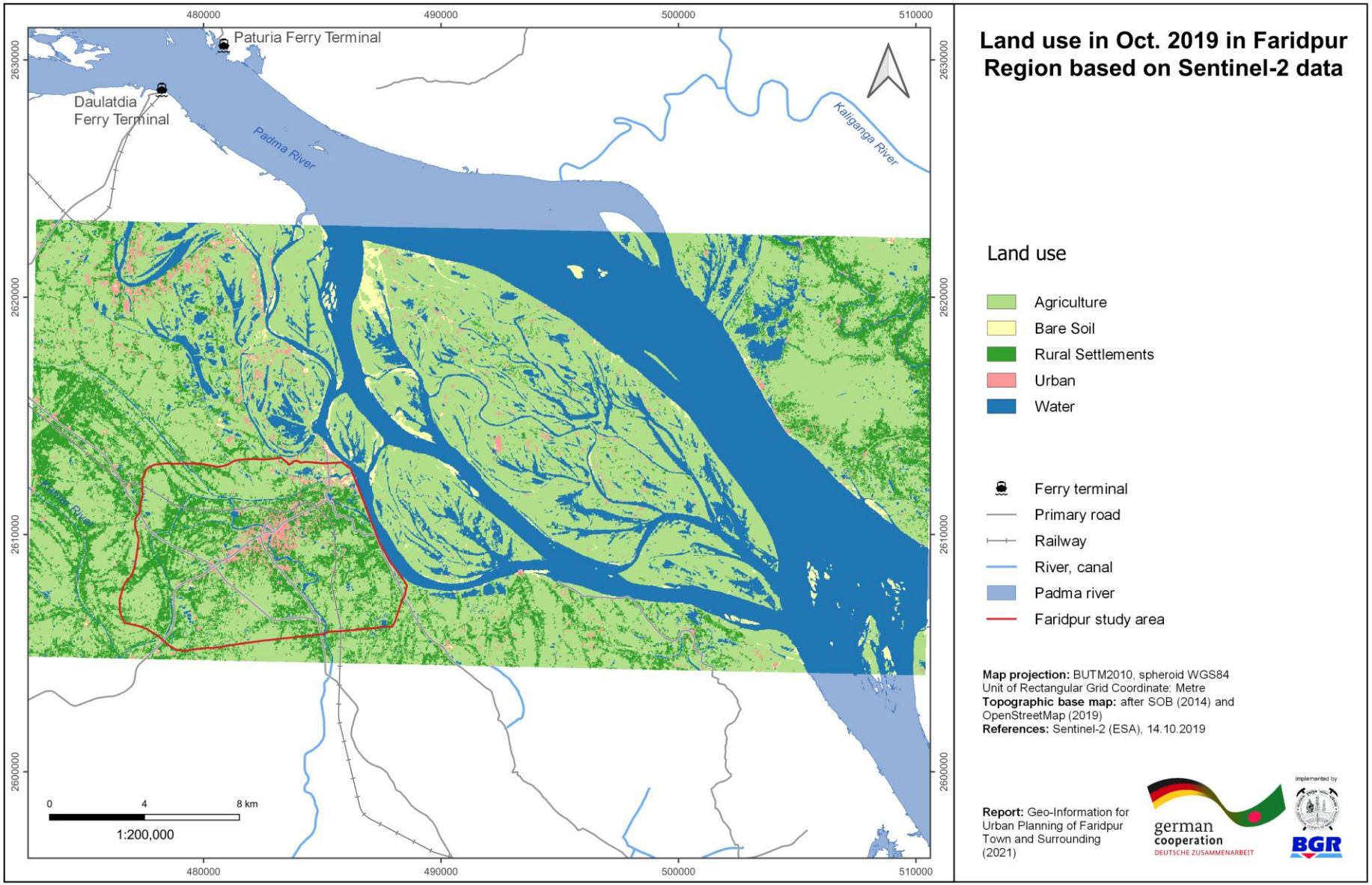

Figure A2: *Land use in October 2019 in Faridpur region based on Sentinel-2 data.*

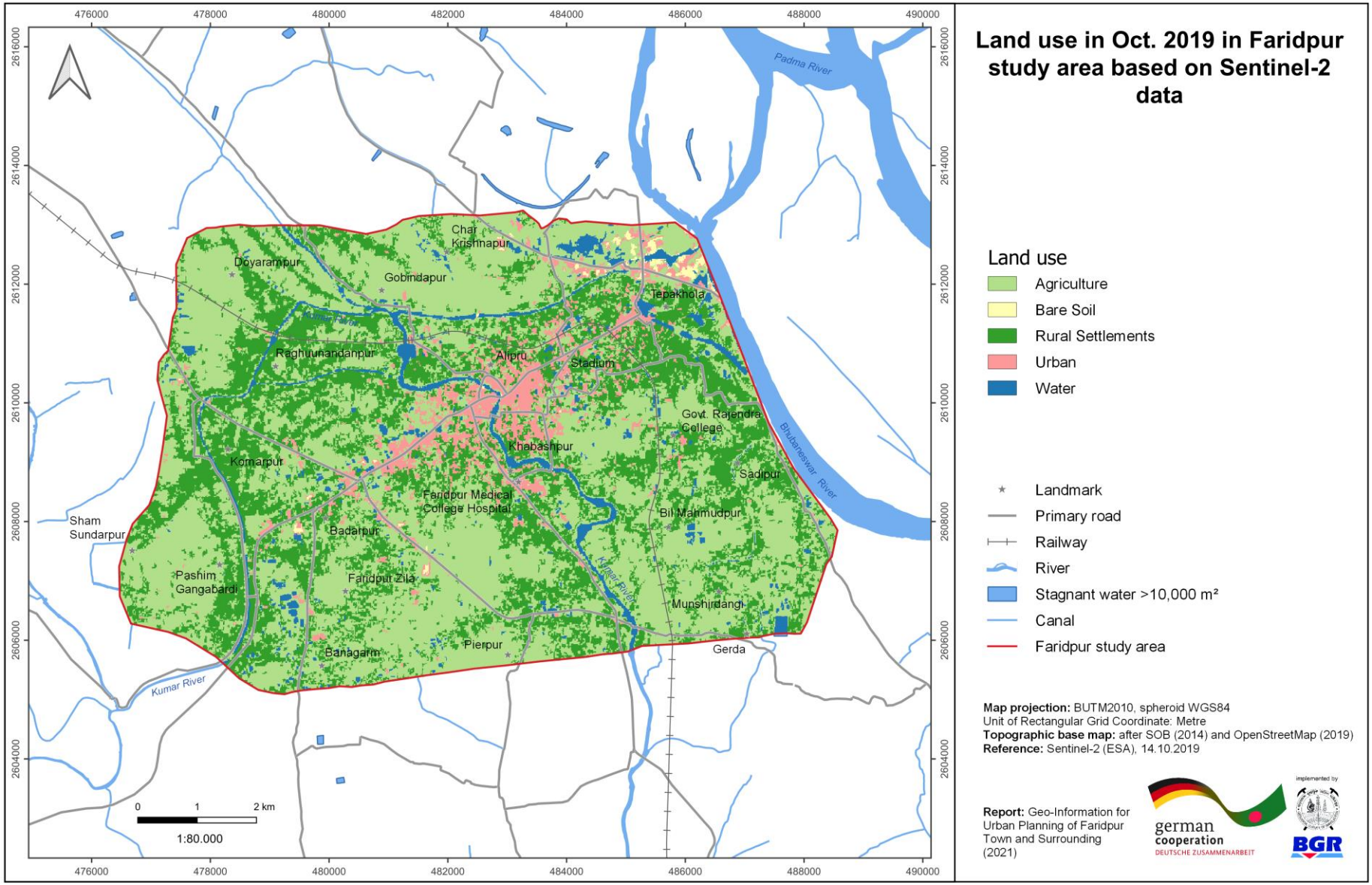

Figure A3: *Land use in October 2019 in Faridpur study area based on Sentinel-2.*

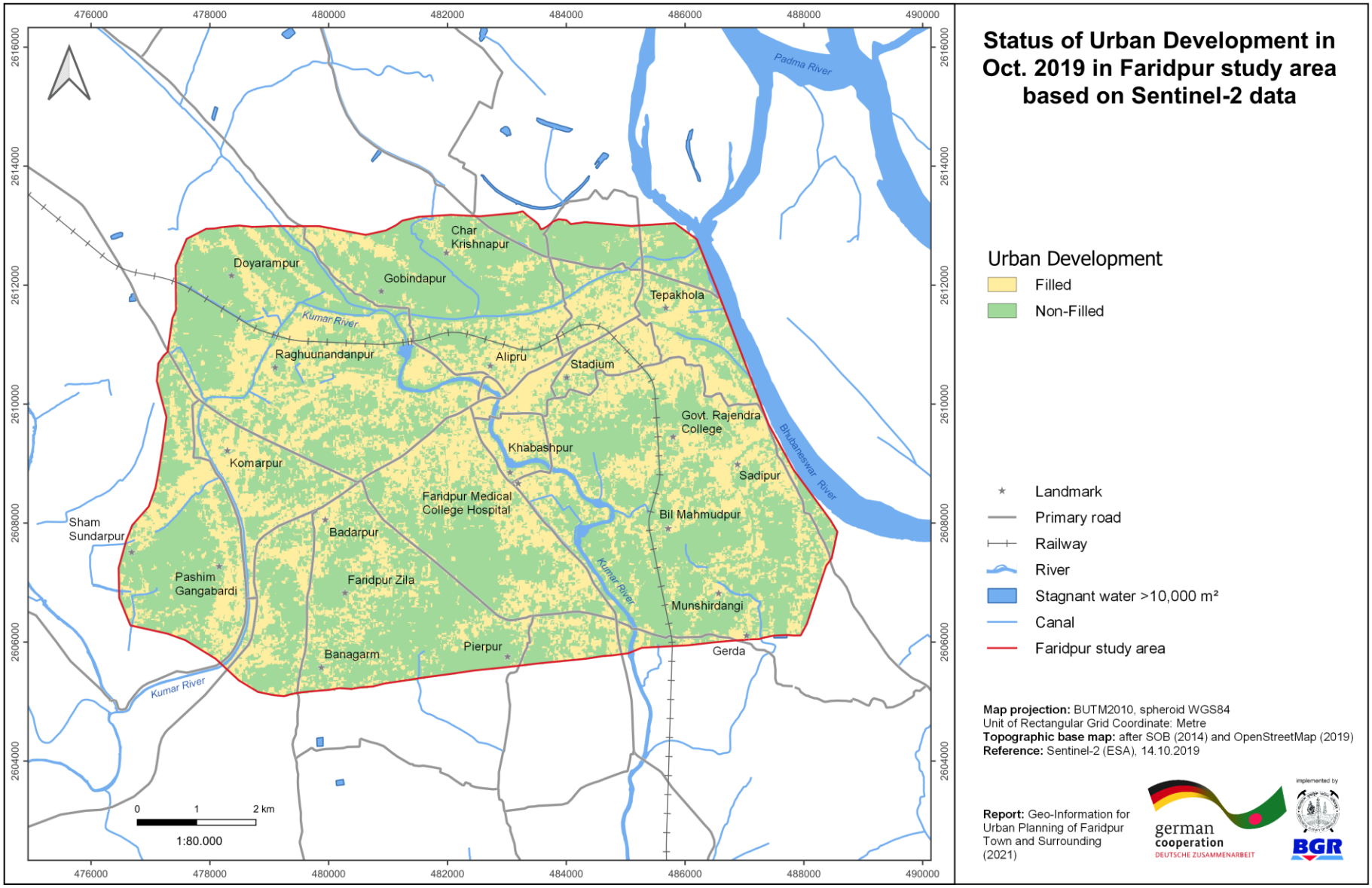

Figure A4: *Status of Urban Development in Oct. 2019 in Faridpur study area.*

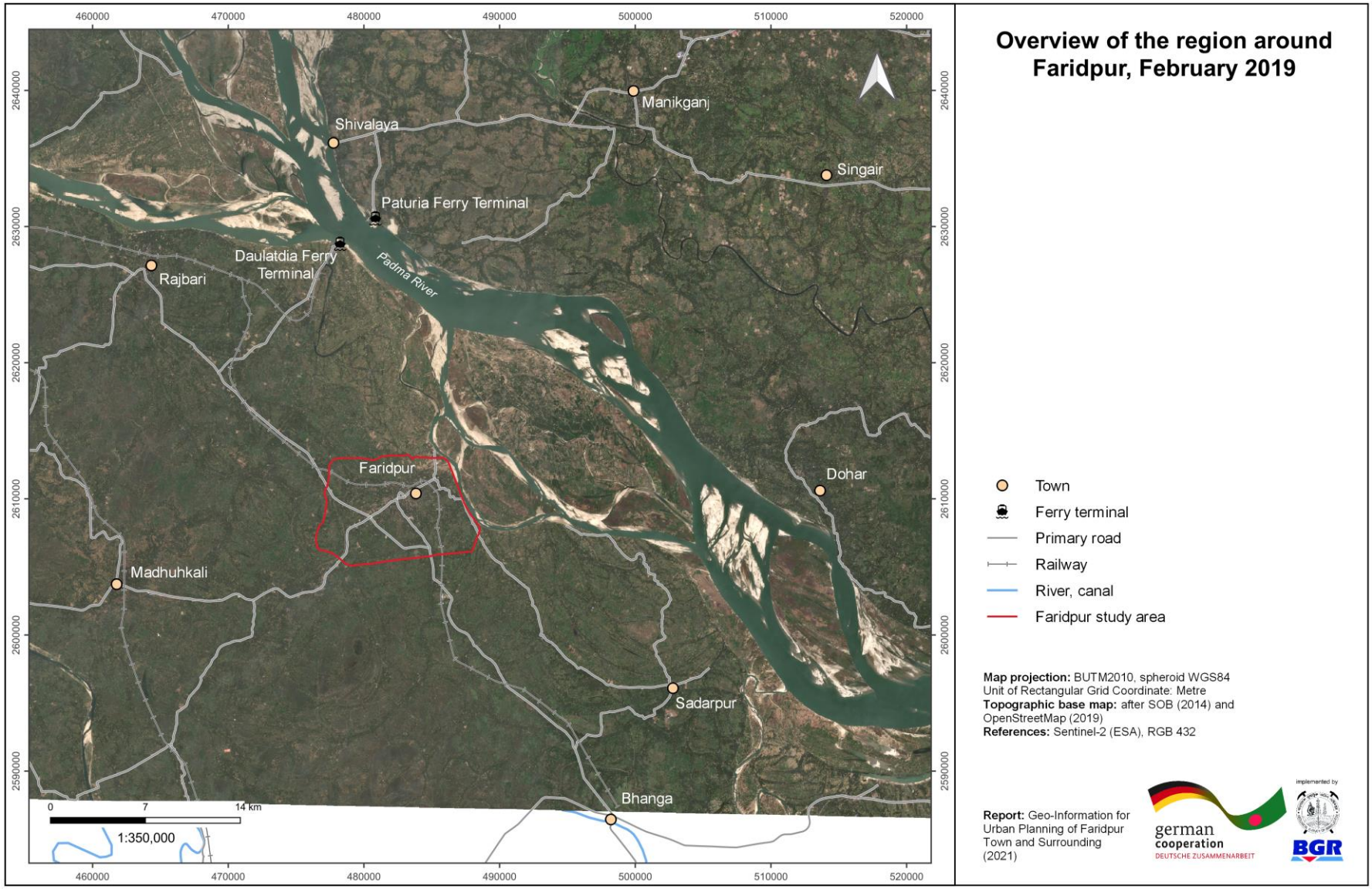

Figure A5: *Overview of the region around Faridpur (Sentinel-2, RGB 432, 11.02.2019).*

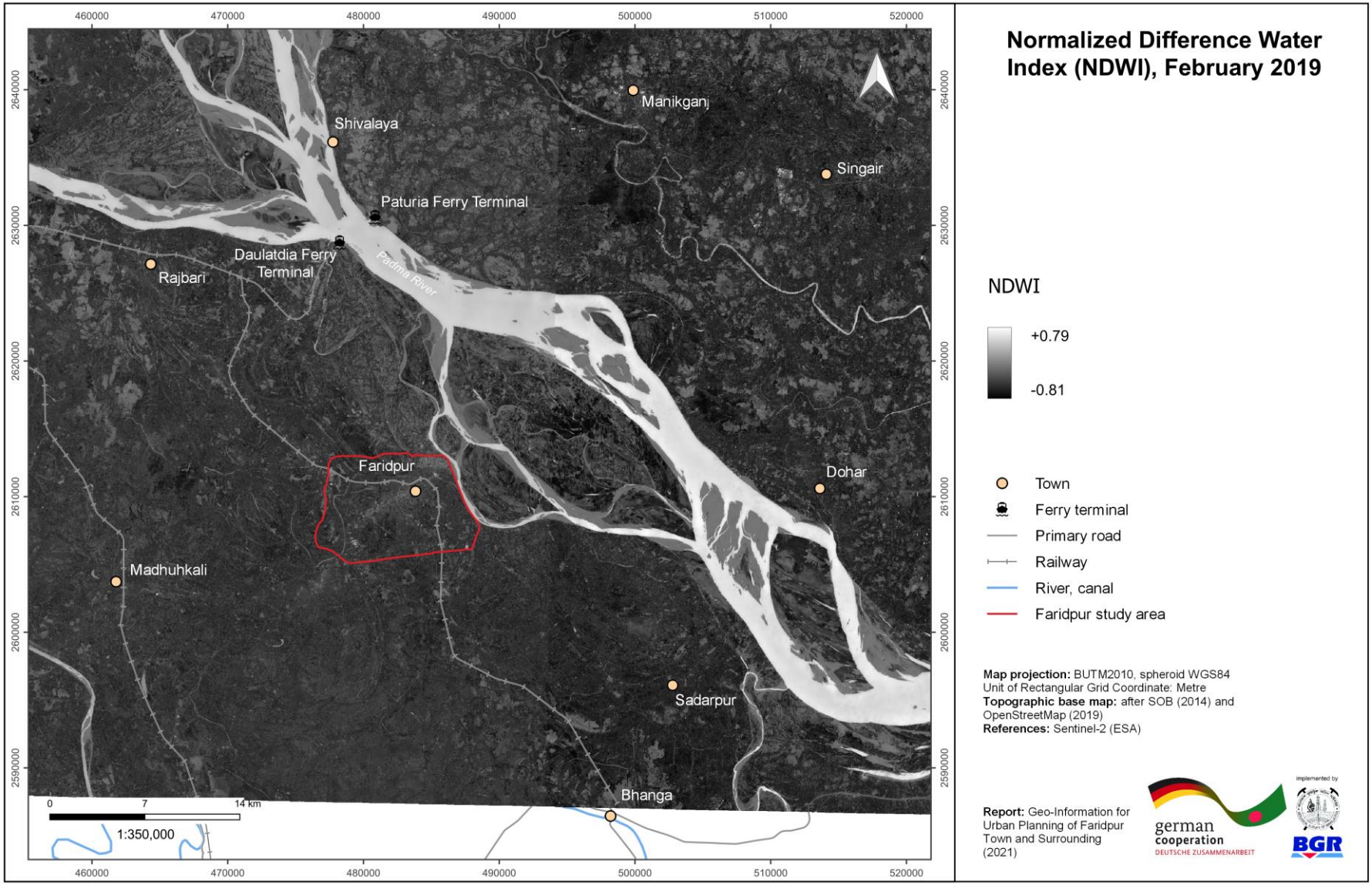

Figure A6: *Normalized Difference Water Index (NDWI), based on Sentinel-2 imagery (11.02.2019).*

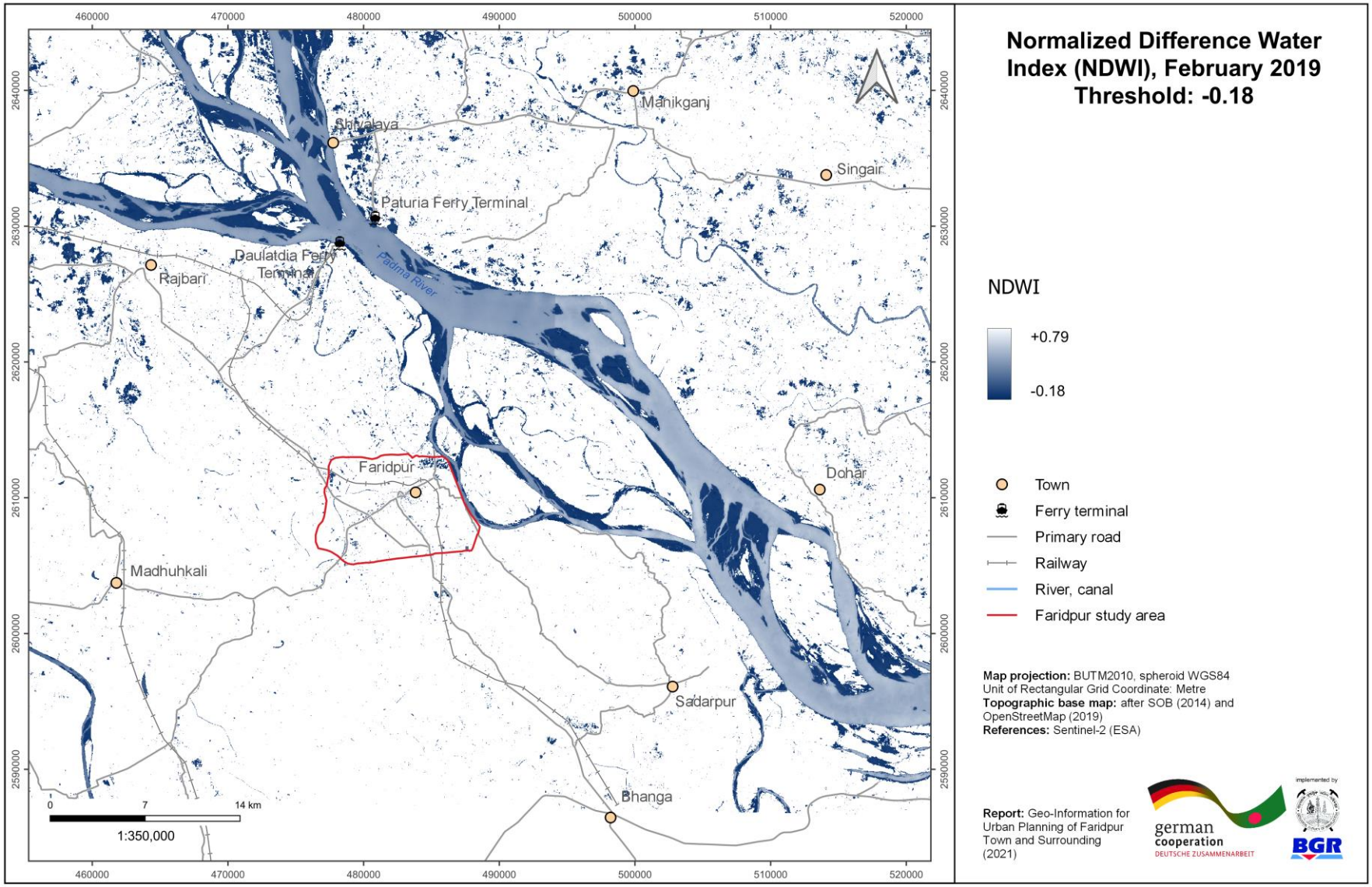

Figure A7: *Normalized Difference Water Index (NDWI), based on Sentinel-2 imagery (11.02.2019), Threshold of -0.18.*

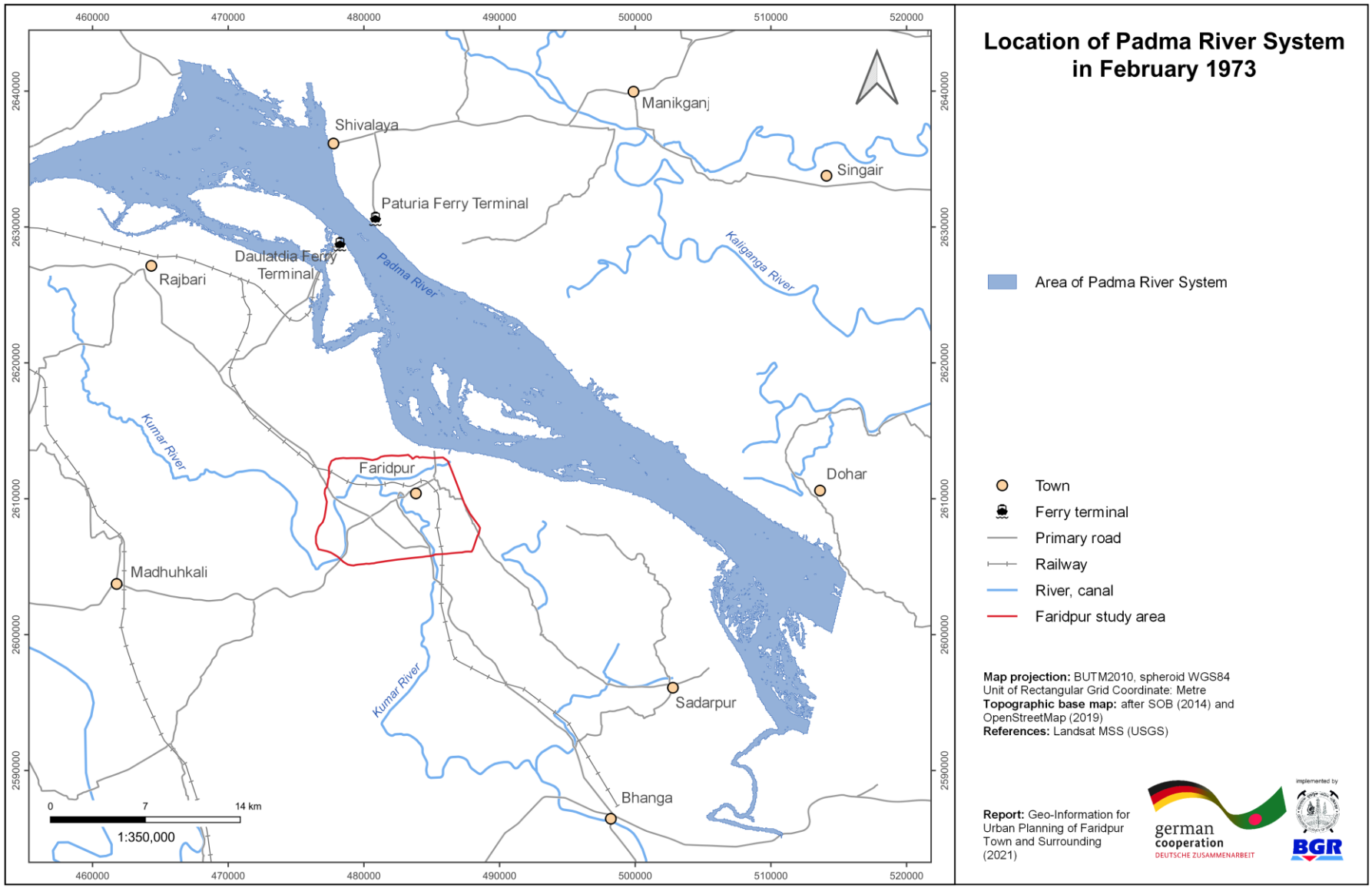

Figure A8: *Location of the Padma River System based on NDWI from 1973.*

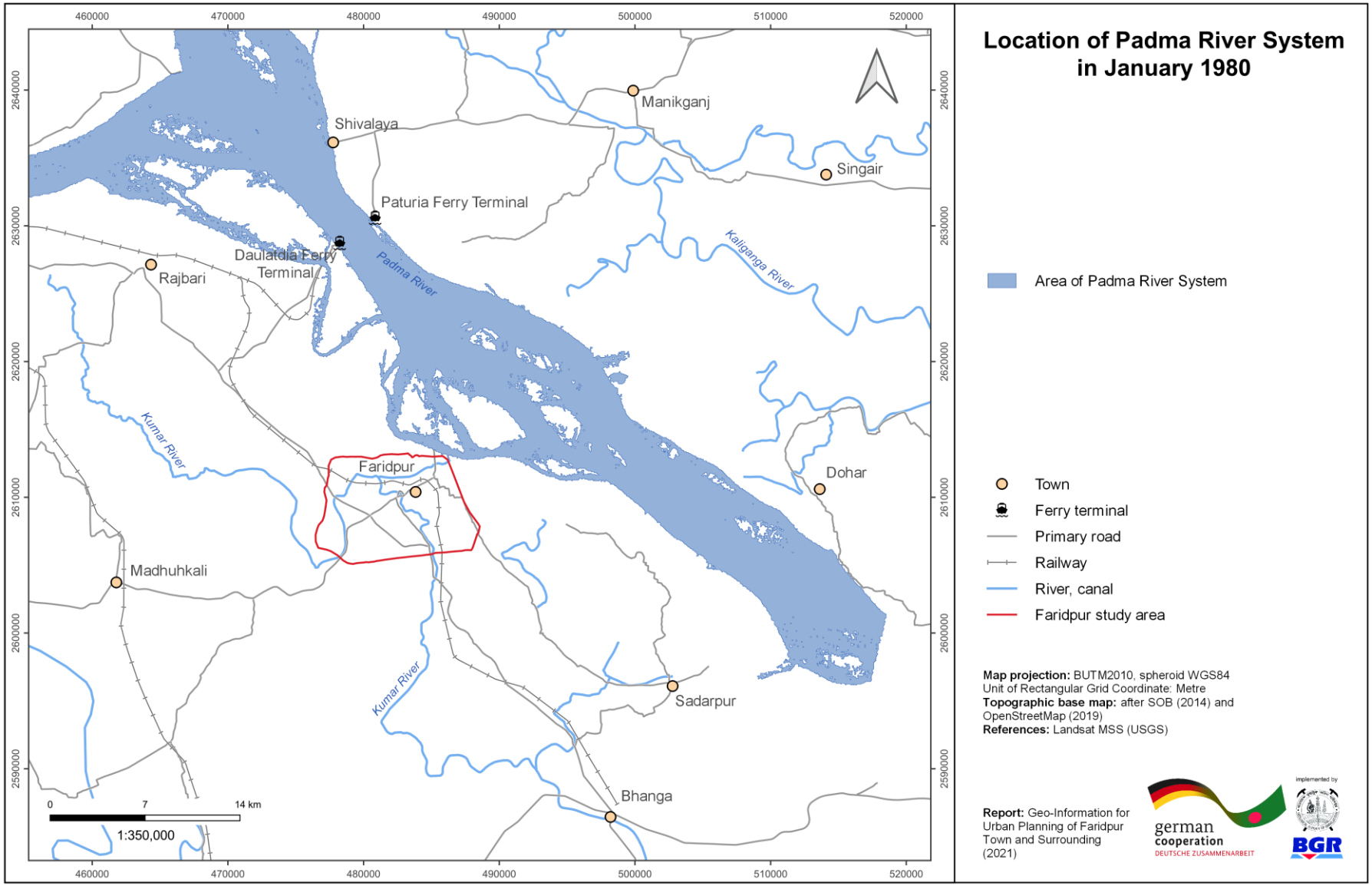

Figure A9: *Location of the Padma River System based on NDWI from 1980.*

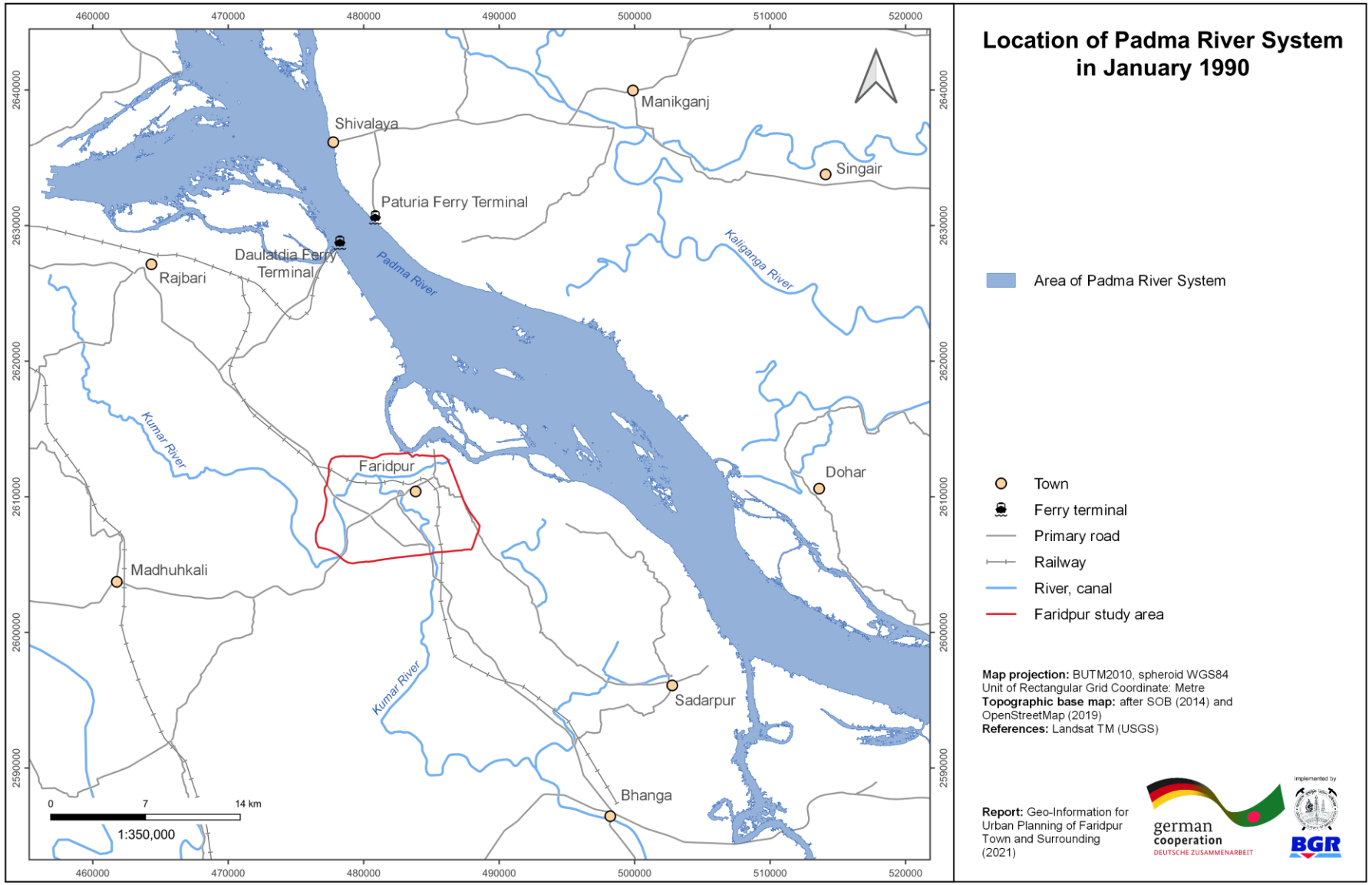

Figure A10: *Location of the Padma River System based on NDWI from 1990.*

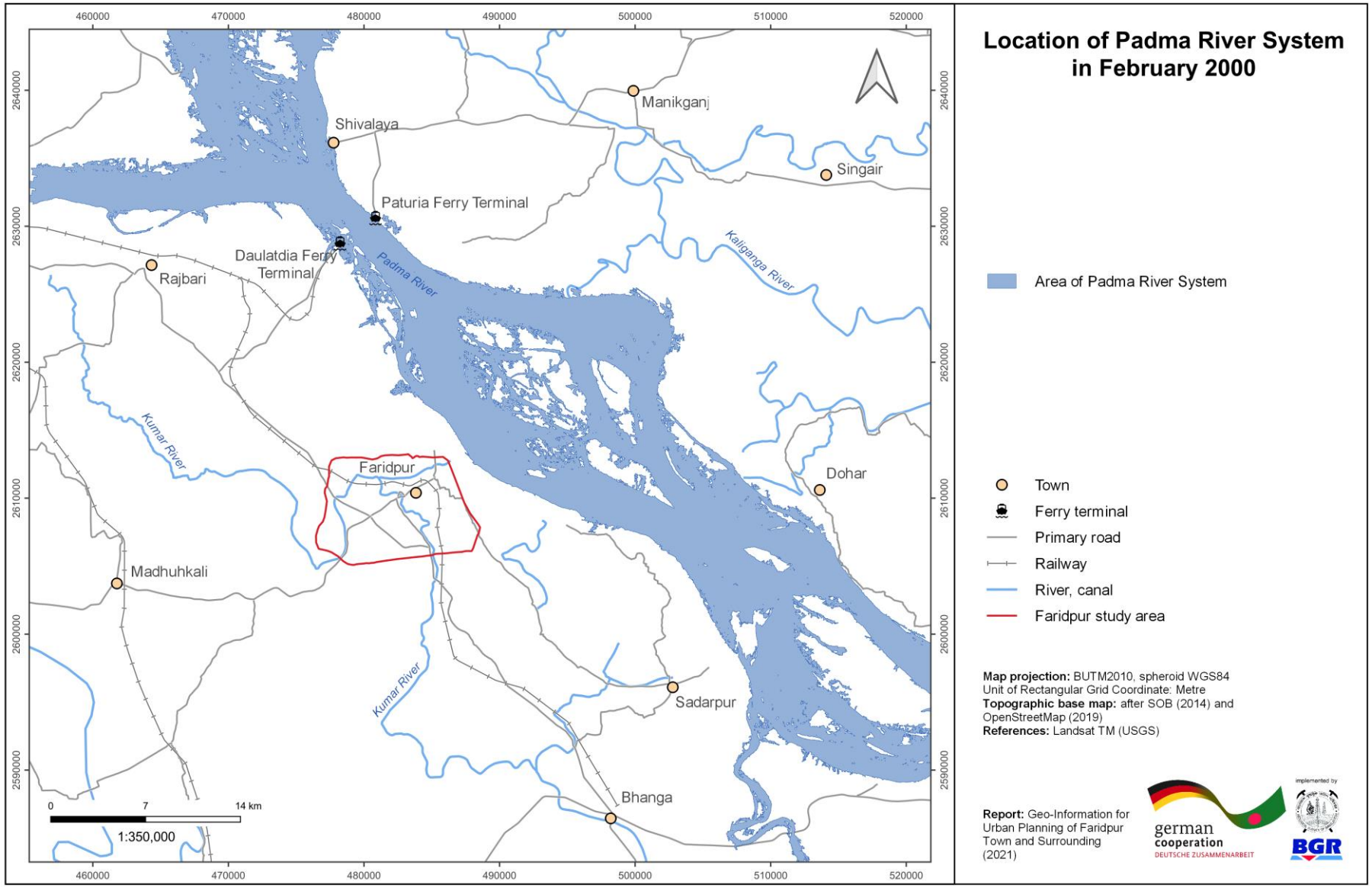

Figure A11: *Location of the Padma River System based on NDWI from 2000.*

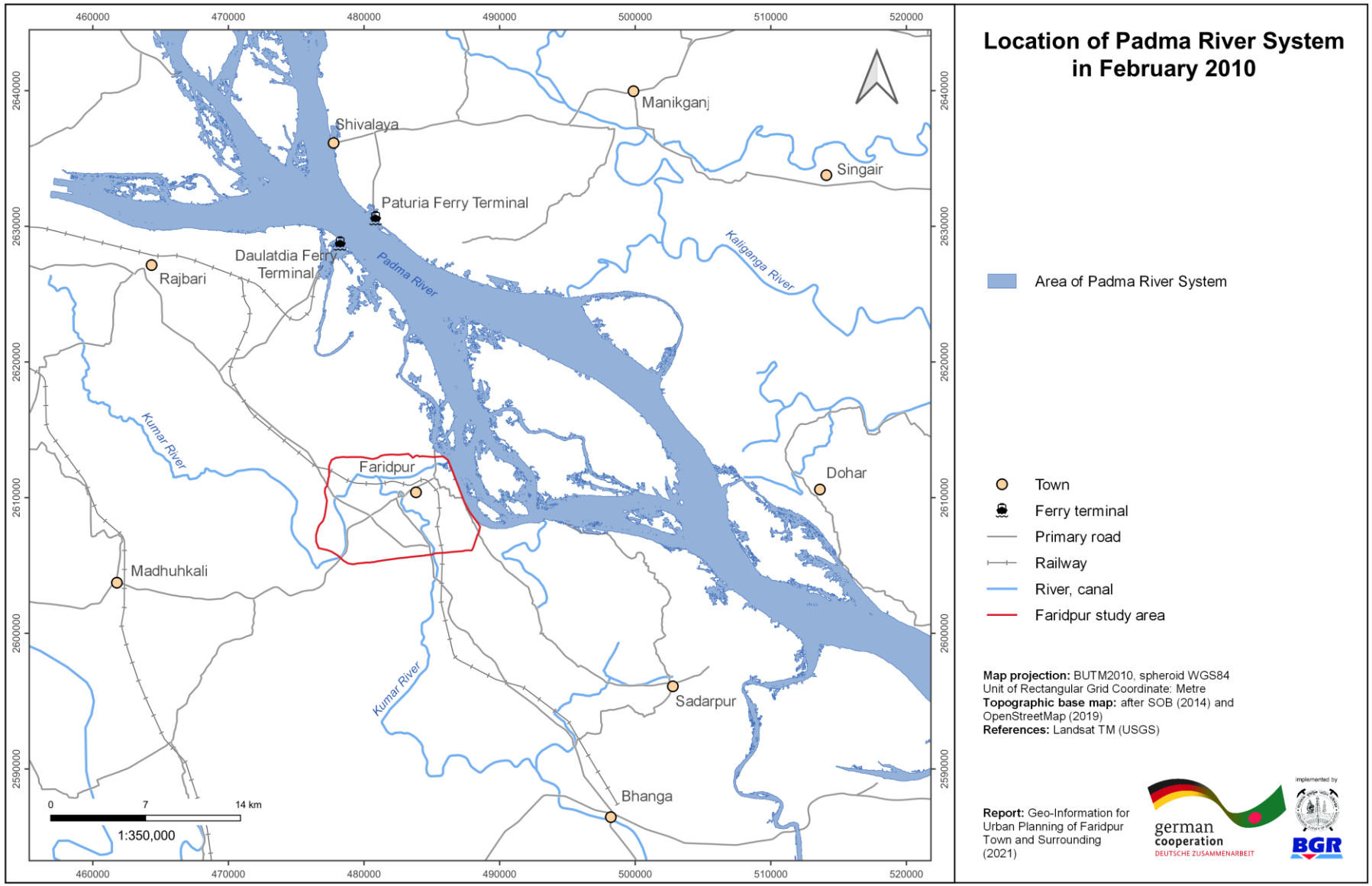

Figure A12: *Location of the Padma River System based on NDWI from 2010.*

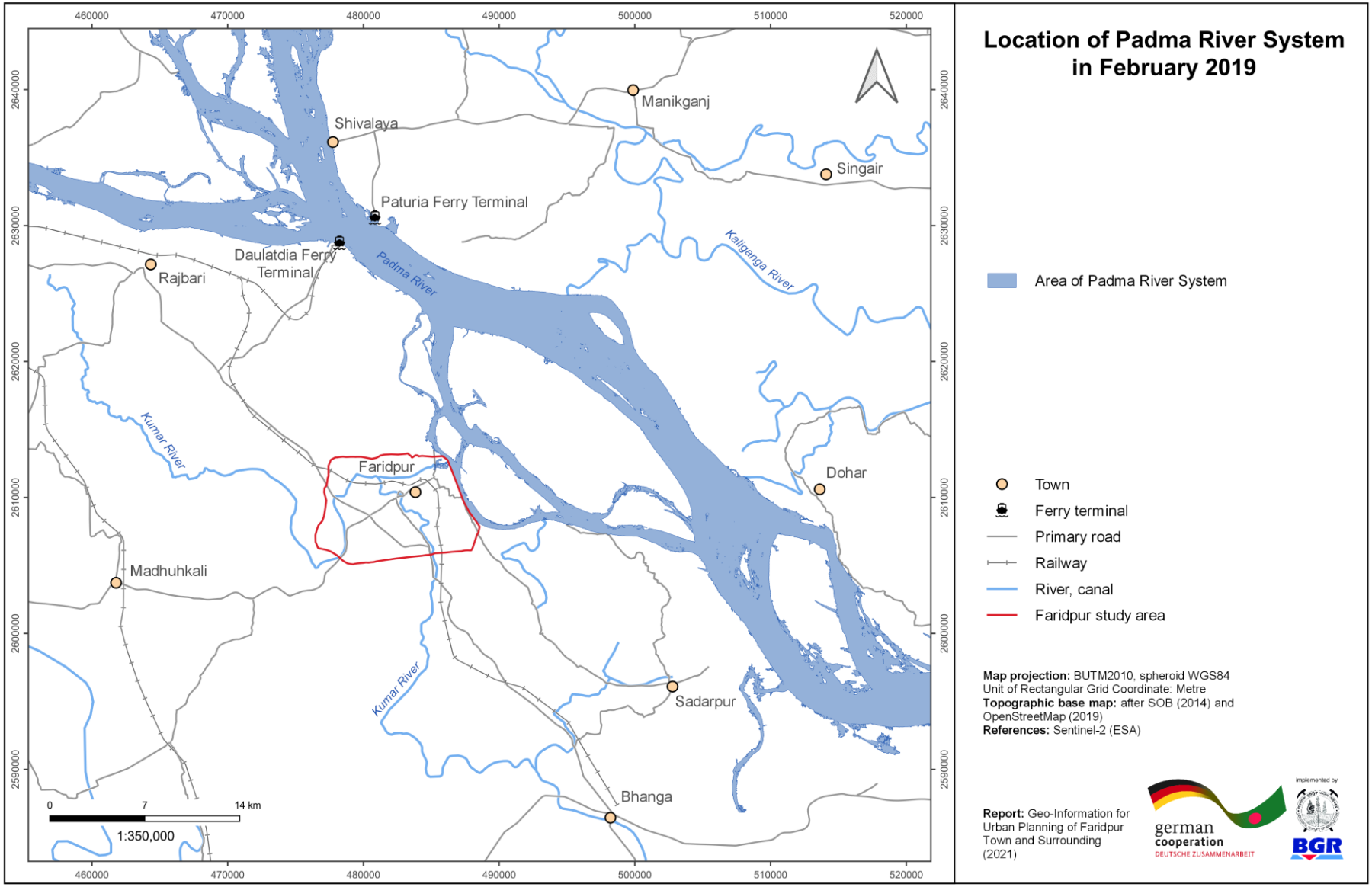

Figure A13: *Location of the Padma River System based on NDWI from 2019.*

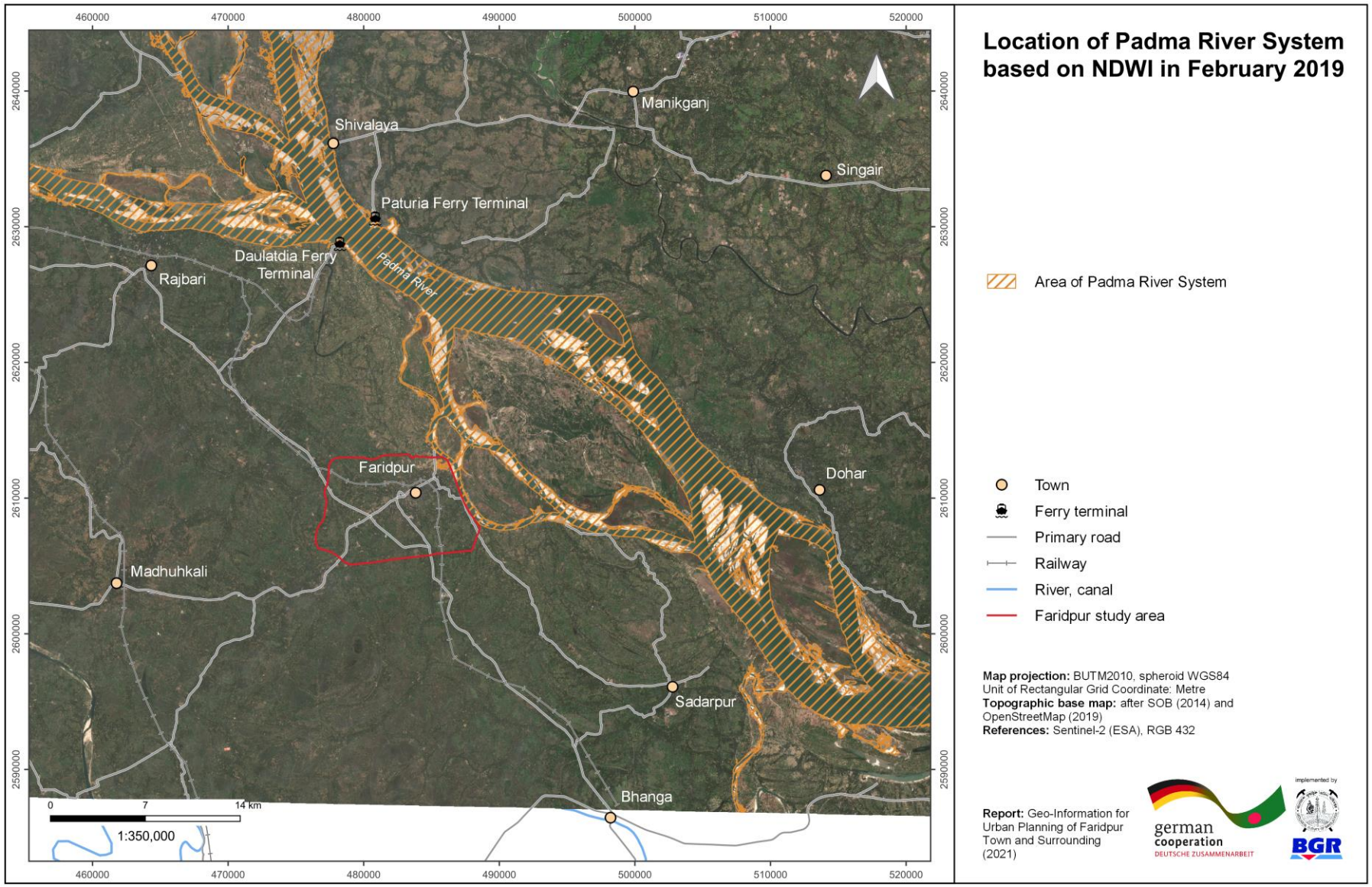

Figure A14: *Location of the Padma River System based on NDWI from 2019.*

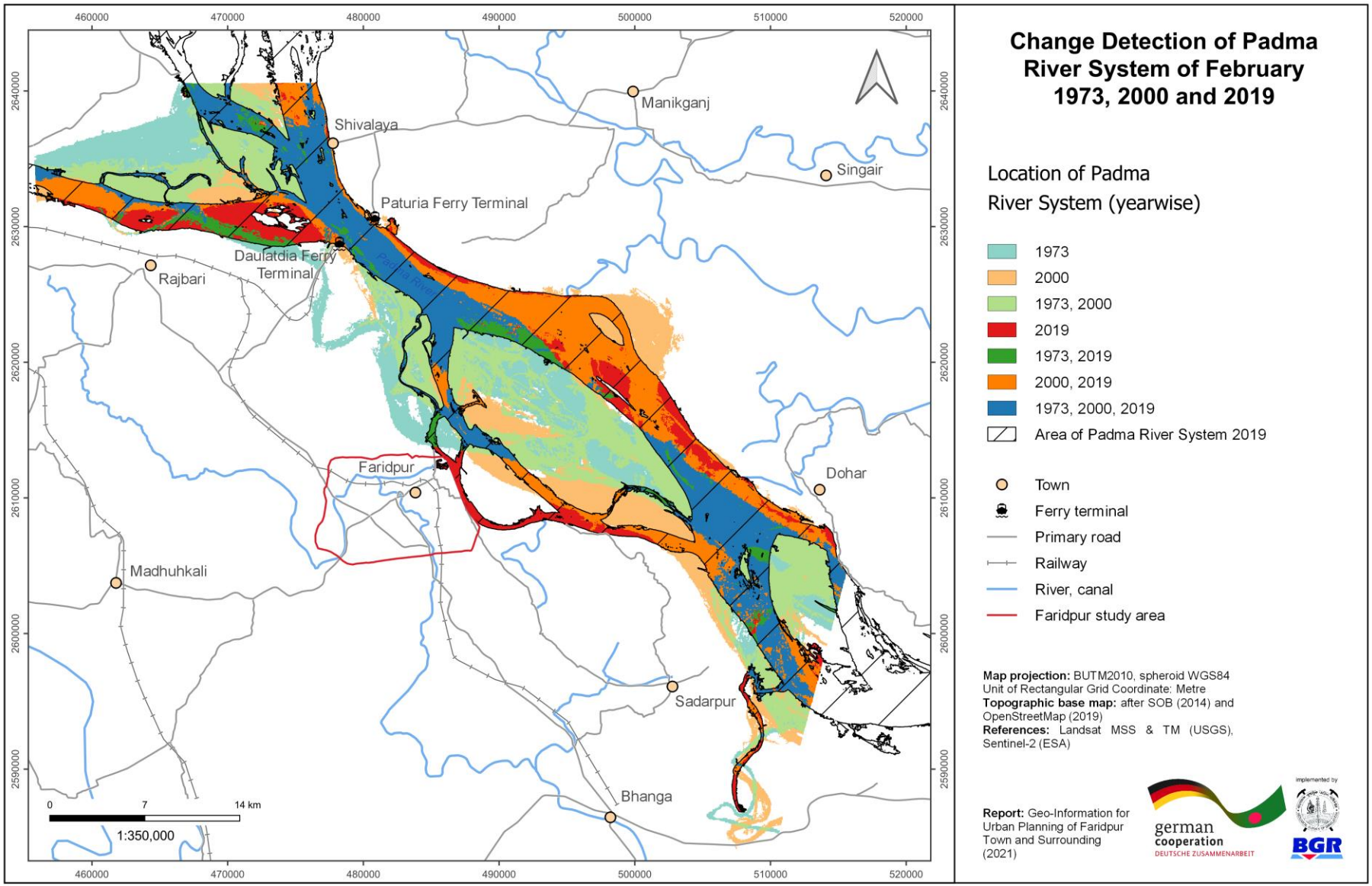

Figure A15: *Change Detection of Padma River System of February 1973, 2000 and 2019.*

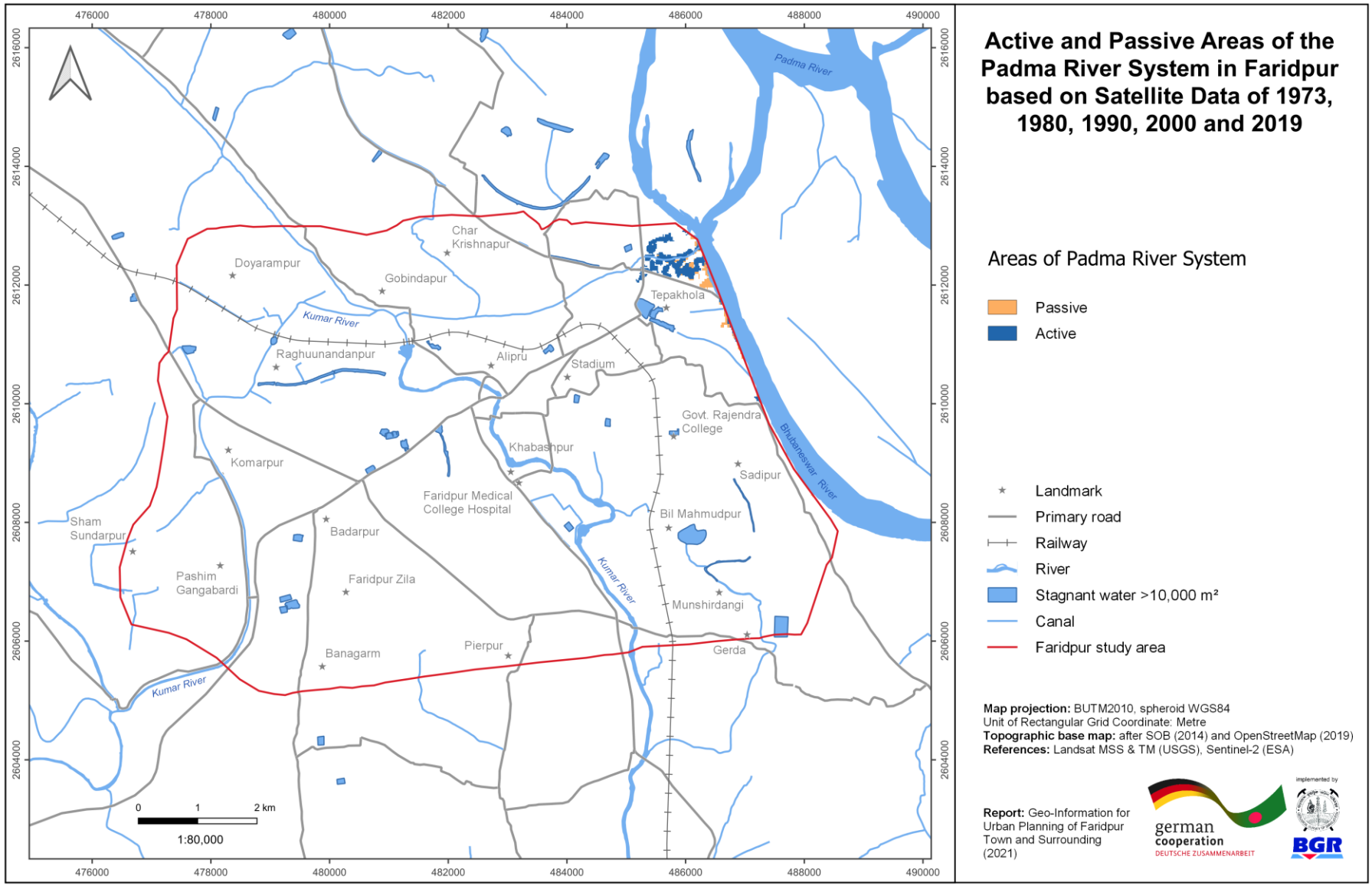

Figure A16: *Active and Passive Areas of the Padma River System in Faridpur, based on Satellite Data of 1973, 1980, 1990, 2000, 2010 and 2019.*

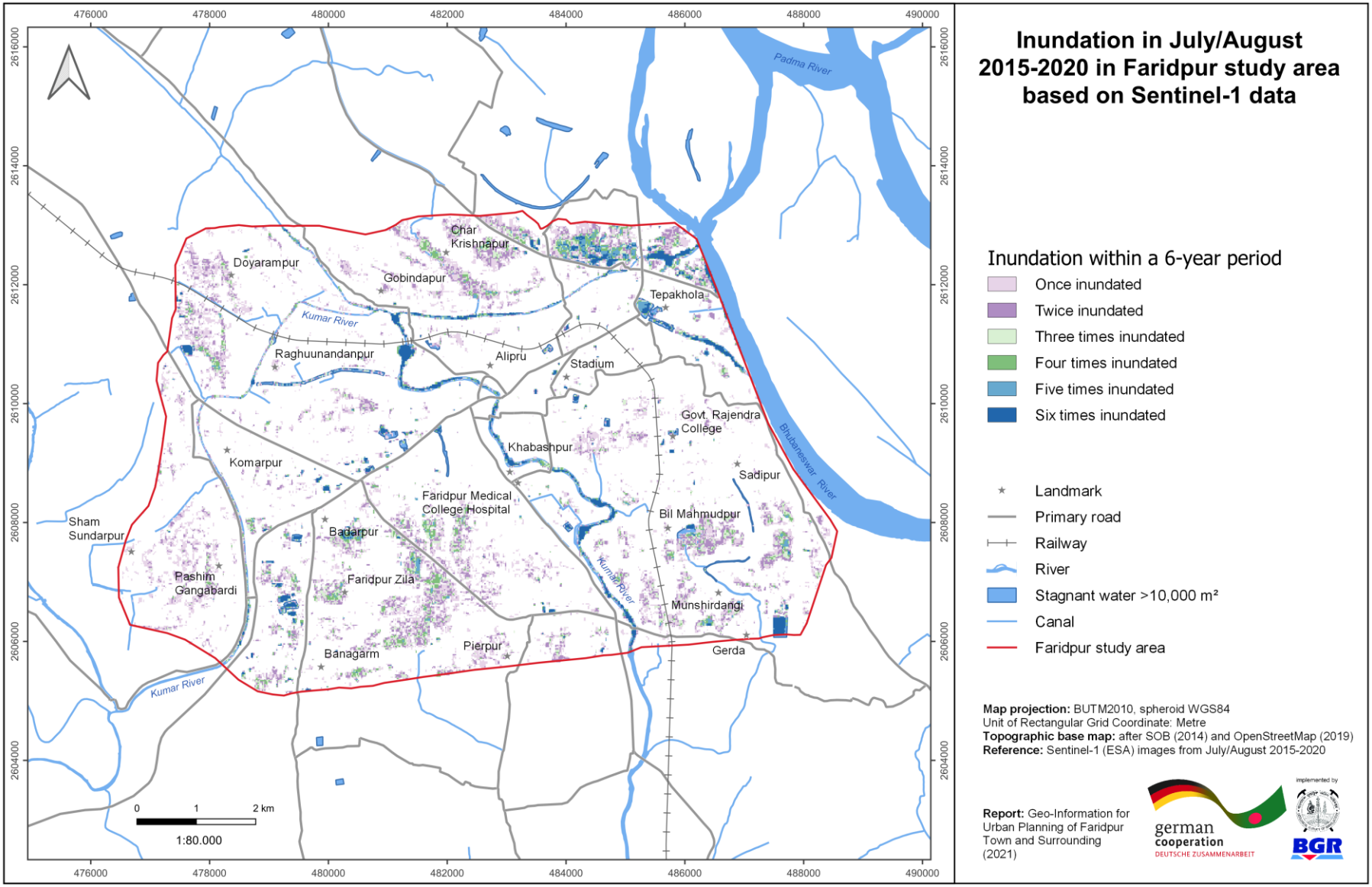

Figure A17: *Inundation in July/August 2015-2020 in Faridpur study area.*

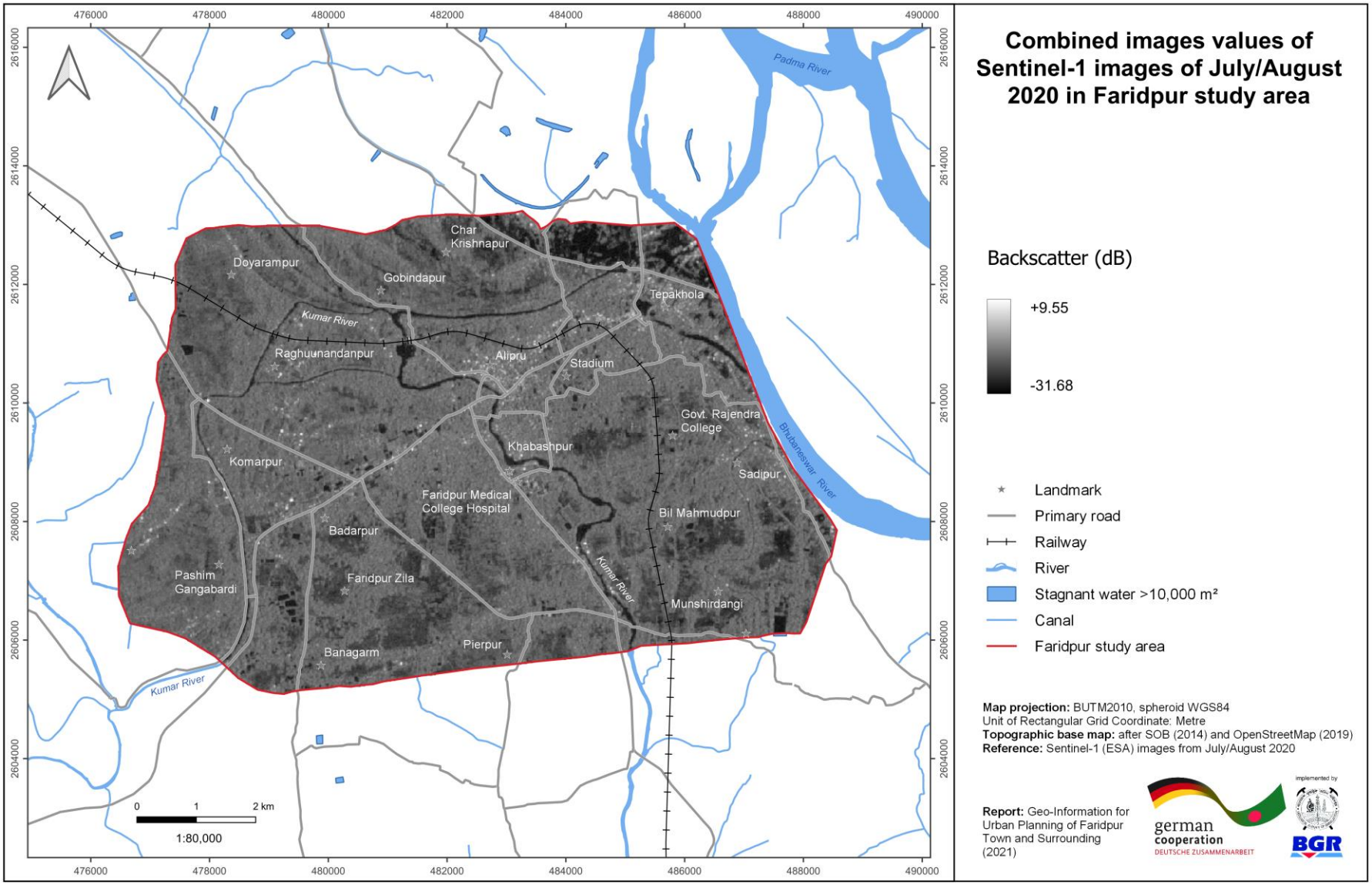

Figure A18: *Combined Sentinel-1 image of July/August 2020 in Faridpur study area.*

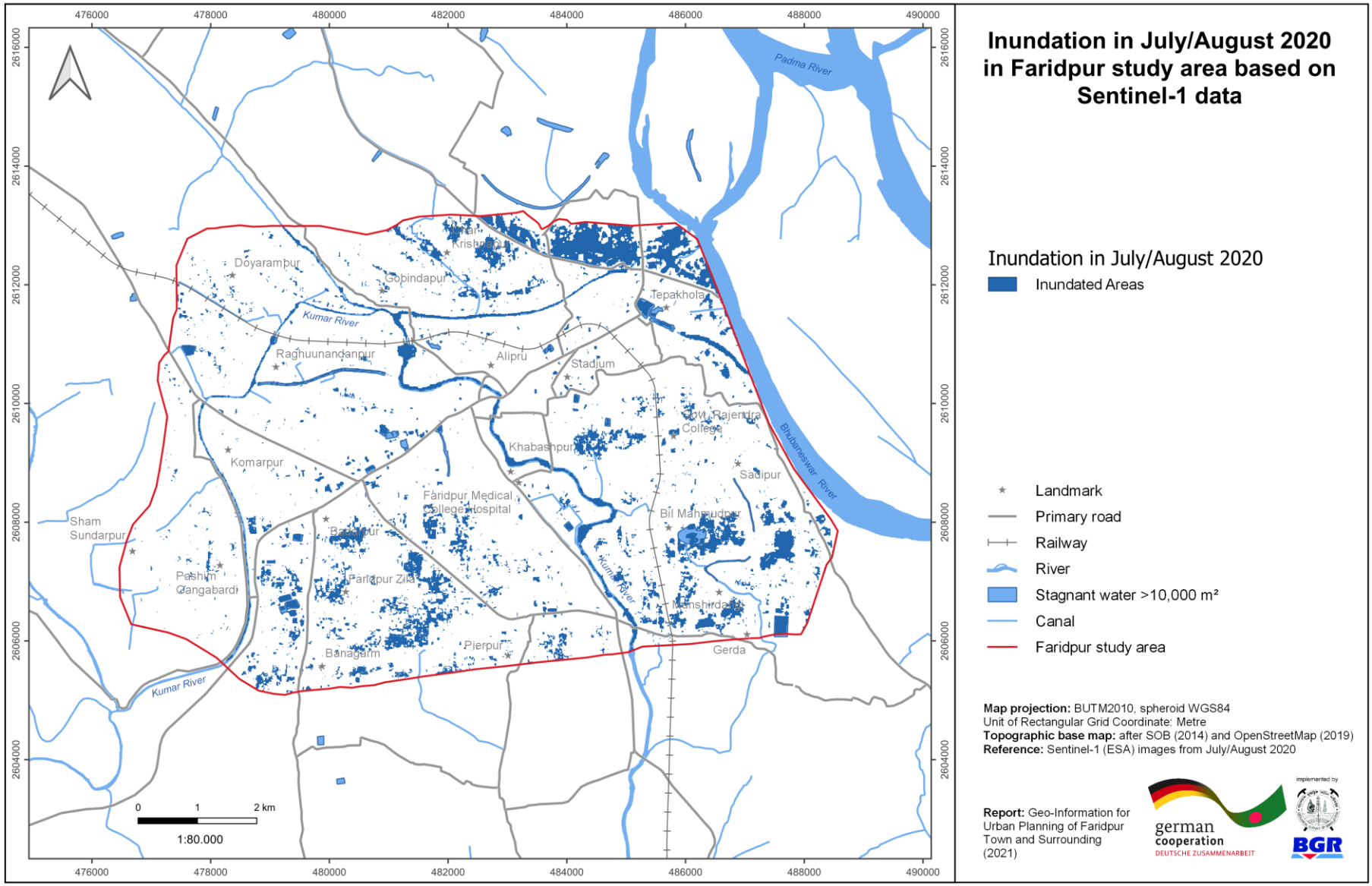

Figure A19: *Inundation in July/August 2020 in Faridpur study area.*

Annexure B: Google Earth Engine Code

```
// Select Area of Interest (pa = uploaded SHP of Faridpur study area)
pa = pa.geometry();
// Center the map with focus on the study area
Map.centerObject(pa);


// 2015
// Define start and end date of the study period
var start_wet = '2015-07-01';
var end_wet = '2015-08-31';

// Load the Sentinel-1 image collection
var S1_wet15 = ee.ImageCollection('COPERNICUS/S1_GRD')
// Filter: Return only Vertical-Horizontal (VH) polarization images
.filter(ee.Filter.listContains('transmitterReceiverPolarisation', 'VH'))
// Filter: Return only images with the main acquisition mode IW
.filter(ee.Filter.eq('instrumentMode', 'IW'))
// Filter: Return only descending orbit images
.filter(ee.Filter.eq('orbitProperties_pass', 'DESCENDING'))
// Filter: Return only images with a 10 m resolution
.filterMetadata('resolution_meters','equals',10)
// Filter: Return only images within the study period
.filterDate(start_wet, end_wet)
// Filter: Return only images within the study area
.filterBounds(KSpa)
// Calculate the mean of all remaining images
.reduce(ee.Reducer.mean())
// Clip the mean-image to the study area
.clip(KSpa);
// Print the image information to the console
print(S1_wet15)


// 2016
var start_wet = '2016-07-01';
var end_wet = '2016-08-31';

var S1_wet16 = ee.ImageCollection('COPERNICUS/S1_GRD')
```

```
39  .filter(ee.Filter.listContains('transmitterReceiverPolarisation', 'VH'))
40  .filter(ee.Filter.eq('instrumentMode', 'IW'))
41  .filter(ee.Filter.eq('orbitProperties_pass', 'DESCENDING'))
42  .filterMetadata('resolution_meters','equals',10)
43  .filterDate(start_wet, end_wet)
44  .filterBounds(KSpa)
45  .reduce(ee.Reducer.mean())
46  .clip(KSpa);
47  print(S1_wet16)
48
49  // 2017
50  var start_wet = '2017-07-01';
51  var end_wet = '2017-08-31';
52
53  var S1_wet17 = ee.ImageCollection('COPERNICUS/S1_GRD')
54  .filter(ee.Filter.listContains('transmitterReceiverPolarisation', 'VH'))
55  .filter(ee.Filter.eq('instrumentMode', 'IW'))
56  .filter(ee.Filter.eq('orbitProperties_pass', 'DESCENDING'))
57  .filterMetadata('resolution_meters','equals',10)
58  .filterDate(start_wet, end_wet)
59  .filterBounds(KSpa)
60  .reduce(ee.Reducer.mean())
61  .clip(KSpa);
62  print(S1_wet17)
63
64  //2018
65  var start_wet = '2018-07-01';
66  var end_wet = '2018-08-31';
67
68  var S1_wet18 = ee.ImageCollection('COPERNICUS/S1_GRD')
69  .filter(ee.Filter.listContains('transmitterReceiverPolarisation', 'VH'))
70  .filter(ee.Filter.eq('instrumentMode', 'IW'))
71  .filter(ee.Filter.eq('orbitProperties_pass', 'DESCENDING'))
72  .filterMetadata('resolution_meters','equals',10)
73  .filterDate(start_wet, end_wet)
74  .filterBounds(KSpa)
75  .reduce(ee.Reducer.mean())
76  .clip(KSpa);
77  print(S1_wet18)
78
79  //2019
80  var start_wet = '2019-07-01';
```

```
var end_wet = '2019-08-31';

var S1_wet19 = ee.ImageCollection('COPERNICUS/S1_GRD')
.filter(ee.Filter.listContains('transmitterReceiverPolarisation', 'VH'))
.filter(ee.Filter.eq('instrumentMode', 'IW'))
.filter(ee.Filter.eq('orbitProperties_pass', 'DESCENDING'))
.filterMetadata('resolution_meters','equals',10)
.filterDate(start_wet, end_wet)
.filterBounds(KSpa)
.reduce(ee.Reducer.mean())
.clip(KSpa);
print(S1_wet19)

//2020
var start_wet = '2020-07-01';
var end_wet = '2020-08-31';

var S1_wet20 = ee.ImageCollection('COPERNICUS/S1_GRD')
.filter(ee.Filter.listContains('transmitterReceiverPolarisation', 'VH'))
.filter(ee.Filter.eq('instrumentMode', 'IW'))
.filter(ee.Filter.eq('orbitProperties_pass', 'DESCENDING'))
.filterMetadata('resolution_meters','equals',10)
.filterDate(start_wet, end_wet)
.filterBounds(KSpa)
.reduce(ee.Reducer.mean())
.clip(KSpa);
print(S1_wet20)

// Set threshold to distinguish between water and non-water
var threshold = -20

// Filter every image collection to the defined threshold
var S1_wet_threshold15 = S1_wet15.select('VH_mean').lt(threshold);
var S1_wet_threshold16 = S1_wet16.select('VH_mean').lt(threshold);
var S1_wet_threshold17 = S1_wet17.select('VH_mean').lt(threshold);
var S1_wet_threshold18 = S1_wet18.select('VH_mean').lt(threshold);
var S1_wet_threshold19 = S1_wet19.select('VH_mean').lt(threshold);
var S1_wet_threshold20 = S1_wet20.select('VH_mean').lt(threshold);

// Combining all images to get one image with six classes
```

```
var final_img =
S1_wet_threshold15.add(S1_wet_threshold16).add(S1_wet_threshold17).add(S1_w
et_threshold18).add(S1_wet_threshold19).add(S1_wet_threshold20);

// Visualize the final result
Map.addLayer(final.updateMask(final_img),{palette:"0000FF"},'Water
extent',1);

// Export the image to the Drive
Export.image.toDrive({
// Definition of the image
  image: final_img,
// Description
  description: 'Faridpur_Inun_Map',
// Resolution in meter
  scale: 20,
// Study area
  region: pa,
// Format of the raster
  fileFormat: 'GeoTIFF'
});

Export.image.toDrive({
  image: S1_wet20.select("VH_mean"),
  description: 'Faridpur_2020_image',
  scale: 10,
  region: pa,
  fileFormat: 'GeoTIFF'
});

Export.image.toDrive({
  image: S1_wet_threshold20,
  description: 'Faridpur_2020_inundation',
  scale: 10,
  region: pa,
  fileFormat: 'GeoTIFF'
});
```

Annexure C: Data

Optical satellite images

Landsat naming convention

Image name (Level-1): LXSS_LLLL_PPPRRR_YYYYMMDD_yyyymmdd_CC_TX

Image name (Level-2): LXSSPPPRRRYYYYMMDDCCTX

Group	**Meaning**		
LXSS	L: Landsat	X: Sensor “M” (MSS), “T” (TM)	SS: Satellite “01” (Landsat 1), “03” (Landsat 3), “05” (Landsat 5)
LLLL	Processing correction level: “L1TP”, “L1GT”, “L1GS”		
PPPRRR	PPP: WRS path		RRR: WRS row
YYYYMMDD	Acquisition year, month, day		
yyyymmdd	Processing year, month, day		
CC	Collection number: “01”, “02”, …		
TX	Collection category: “RT” (Real-Time), “T1” (Tier 1), “T2” (Tier 2)		

Source: usgs.gov/faqs/how-can-i-tell-difference-between-landsat-collections-data-and-landsat-data-i-have-downloaded (Accessed on 20-07-2020).

Data (Landsat MSS, Level-1)

Year	Image name	Product
1973	LM01_L1TP_148044_19730221_20180427_01_T2	River Shifting Change Detection Analysis
1980	LM03_L1TP_148043_19800116_20180416_01_T2	River Shifting Change Detection Analysis
	LM03_L1TP_148044_19800116_20180416_01_T2	River Shifting Change Detection Analysis

Data (Landsat TM, Level-2)

Year	Image name	Product
1990	LT05137044l990010701T1	River Shifting Change Detection Analysis
2000	LT05137044200002001T1	River Shifting Change Detection Analysis
2010	LT05137044201002l501T1	River Shifting Change Detection Analysis

Sentinel-2 naming convention

Image name: MMM_MSIXXX_YYYYMMDDHHMMSS_Nxxyy_ROOO_Txxxxx_<Product Discriminator>

Group	Meaning
MMM	Mission ID: “S2A”, “S2B”
MSIXXX	Product level: “Level-1C”, “Level-2A”
YYYYMMDDTHHMMSS	Sensing start time, date and time separated by character “T”
Nxxyy	PDGS processing baseline number
ROOO	Relative orbit number
Txxxxx	Tile number

Source: sentinel.esa.int/web/sentinel/user-guides/sentinel-2-msi/naming-convention (Accessed on 20-07-2020).

Data

Year	Image name	Product
2019	S2A_MSIL2A_20190211T042921_N0211_R133_T45QYG_20190211T083914	River Shifting Change Detection Analysis
	S2A_MSIL2A_20190211T042921_N0211_R133_T45QZG_20190211T083914	River Shifting Change Detection Analysis
	S2B_MSIL2A_20191014T042729_N0213_R133_T45QYG_20191014T084037	Land-Use Classification
	S2B_MSIL2A_20191014T042729_N0213_R133_T45QZG_20191014T084037	Land-Use Classification

RADAR satellite images

Sentinel-1 naming convention

Image name: MMM_BB_TTTR_LFPP_YYYYMMDDTHHMMSS_ YYYYMMDDTHHMMSS_OOOOOO_DDDDDD_CCCC

Group	Meaning		
MMM	Mission Identifier: “S1A”, S1B”		
BB	Mode/Beam: “S1/S2/S3/S4/S5/S6”, “IW/EW/WV”		
TTTR	TTT: Product Type “RAW”, “SLC”, “GRD”, “OCN”	R: Resolution Class “F” (Full), “H” (High), “M” (Medium)	
LFPP	L: Processing Level “0”, “1”, “2”	F: Product Class “S” (Standard), “A” (Annotation)	PP: Polarization “SH” (single HH) “SV” (single VV)

			“DH” (dual HH+HV) “DV” (dual VV+VH)
YYYYMMDDTHHMMSS	Product start time, separated by the character “T”		
YYYYMMDDTHHMMSS	Product end time, separated by the character “T”		
OOOOOO	Absolute orbit number at product start time		
DDDDDD	Mission data-take identifier		
CCCC	Product unique identifier		

Source: sentinel.esa.int/web/sentinel/user-guides/sentinel-1-sar/naming-conventions (Accessed on 20-07-2020).

Data: Inundation Mapping

Year	Image Name
2015	S1A_IW_GRDH_1SDV_20150706T235524_20150706T235549_006697_008F55_E0E4
	S1A_IW_GRDH_1SDV_20150823T235527_20150823T235552_007397_00A2D6_99F8
2016	S1A_IW_GRDH_1SDV_20160724T235529_20160724T235554_012297_013213_0790
	S1A_IW_GRDH_1SDV_20160817T235531_20160817T235556_012647_013DA7_714D
2017	S1A_IW_GRDH_1SDV_20170731T235557_20170731T235622_017722_01DAEC_A475
	S1A_IW_GRDH_1SDV_20170812T235557_20170812T235622_017897_01E03B_D81A
	S1A_IW_GRDH_1SDV_20170824T235558_20170824T235623_018072_01E586_FF38
2018	S1A_IW_GRDH_1SDV_20180714T235602_20180714T235627_022797_0278AA_BFC4
	S1A_IW_GRDH_1SDV_20180726T235603_20180726T235628_022972_027E33_0CE9
	S1A_IW_GRDH_1SDV_20180807T235604_20180807T235629_023147_0283AC_6EDB

	S1A_IW_GRDH_1SDV_20180819T235604_20180819T235629_023322_028959_14CB
2019	S1A_IW_GRDH_1SDV_20190709T235608_20190709T235633_028047_032AE1_EBE3
	S1A_IW_GRDH_1SDV_20190721T235609_20190721T235634_028222_033027_D84D
	S1A_IW_GRDH_1SDV_20190802T235609_20190802T235634_028397_03357D_AEEC
	S1A_IW_GRDH_1SDV_20190826T235611_20190826T235636_028747_03414E_B972
2020	S1A_IW_GRDH_1SDV_20200703T235614_20200703T235639_033297_03DB97_BBB1
	S1A_IW_GRDH_1SDV_20200715T235615_20200715T235640_033472_03E0EC_97C8
	S1A_IW_GRDH_1SDV_20200727T235616_20200727T235641_033647_03E64C_C629
	S1A_IW_GRDH_1SDV_20200808T235616_20200808T235641_033822_03EBE2_0A06
	S1A_IW_GRDH_1SDV_20200820T235617_20200820T235642_033997_03F204_62E3
	S1B_IW_GRDH_1SDV_20200721T235523_20200721T235548_022576_02AD94_45A2

Data: Ground Motion Map

Descending Sentinel-1 scenes for InSAR analyses

S1A_IW_SLC__1SDV_20141015T235522_20141015T235549_002847_003367_F5C6
S1A_IW_SLC__1SDV_20141108T235521_20141108T235548_003197_003AF2_6EA3
S1A_IW_SLC__1SDV_20141202T235521_20141202T235548_003547_0042D9_67A6
S1A_IW_SLC__1SDV_20150119T235519_20150119T235546_004247_0052B2_7043
S1A_IW_SLC__1SDV_20150212T235518_20150212T235545_004597_005A90_4D92
S1A_IW_SLC__1SDV_20150308T235519_20150308T235546_004947_0062FA_5343
S1A_IW_SLC__1SDV_20150401T235519_20150401T235546_005297_006B3E_D9D8
S1A_IW_SLC__1SDV_20150425T235519_20150425T235547_005647_0073D9_C0A1
S1A_IW_SLC__1SDV_20150519T235521_20150519T235549_005997_007BAF_BEEA
S1A_IW_SLC__1SDV_20150612T235522_20150612T235550_006347_0085AA_6E0A
S1A_IW_SLC__1SDV_20150706T235523_20150706T235550_006697_008F55_B0EB
S1A_IW_SLC__1SDV_20150823T235525_20150823T235553_007397_00A2D6_A5C0
S1A_IW_SLC__1SDV_20151010T235527_20151010T235555_008097_00B5A9_8AEF
S1A_IW_SLC__1SDV_20151127T235522_20151127T235548_008797_00C8C8_ABA7
S1A_IW_SLC__1SDV_20151127T235546_20151127T235613_008797_00C8C8_D70F
S1A_IW_SLC__1SDV_20160207T235519_20160207T235546_009847_00E6BD_9DD0
S1A_IW_SLC__1SDV_20160207T235544_20160207T235611_009847_00E6BD_03C9
S1A_IW_SLC__1SDV_20160302T235519_20160302T235546_010197_00F0DB_6CA4
S1A_IW_SLC__1SDV_20160302T235544_20160302T235611_010197_00F0DB_8369
S1A_IW_SLC__1SDV_20160419T235521_20160419T235548_010897_010539_3AC0
S1A_IW_SLC__1SDV_20160419T235545_20160419T235612_010897_010539_088B
S1A_IW_SLC__1SDV_20160513T235525_20160513T235552_011247_01104B_7655
S1A_IW_SLC__1SDV_20160513T235550_20160513T235616_011247_01104B_2228
S1A_IW_SLC__1SDV_20160525T235544_20160525T235613_011422_011608_FEB3
S1A_IW_SLC__1SDV_20160606T235526_20160606T235553_011597_011B95_9FBF
S1A_IW_SLC__1SDV_20160606T235551_20160606T235618_011597_011B95_C5E0
S1A_IW_SLC__1SDV_20160630T235527_20160630T235554_011947_0126A4_63BF
S1A_IW_SLC__1SDV_20160630T235552_20160630T235619_011947_0126A4_34F5
S1A_IW_SLC__1SDV_20160724T235529_20160724T235556_012297_013213_2F37
S1A_IW_SLC__1SDV_20160724T235553_20160724T235620_012297_013213_D33D
S1A_IW_SLC__1SDV_20160817T235530_20160817T235557_012647_013DA7_1834
S1A_IW_SLC__1SDV_20160817T235555_20160817T235622_012647_013DA7_5BED
S1A_IW_SLC__1SDV_20160910T235531_20160910T235558_012997_014938_242A
S1A_IW_SLC__1SDV_20160910T235556_20160910T235623_012997_014938_C7AF
S1A_IW_SLC__1SDV_20161004T235531_20161004T235558_013347_015498_06EA
S1A_IW_SLC__1SDV_20161004T235556_20161004T235623_013347_015498_69D0
S1A_IW_SLC__1SDV_20161028T235532_20161028T235559_013697_015F8B_1FA0

S1A_IW_SLC__1SDV_20161028T235556_20161028T235623_013697_015F8B_8AC5
S1A_IW_SLC__1SDV_20161121T235531_20161121T235558_014047_016A65_4879
S1A_IW_SLC__1SDV_20161121T235556_20161121T235623_014047_016A65_9A39
S1A_IW_SLC__1SDV_20161215T235530_20161215T235557_014397_017565_3F58
S1A_IW_SLC__1SDV_20161215T235555_20161215T235622_014397_017565_ACD4
S1A_IW_SLC__1SDV_20170108T235528_20170108T235555_014747_018021_6610
S1A_IW_SLC__1SDV_20170108T235553_20170108T235620_014747_018021_AF78
S1A_IW_SLC__1SDV_20170201T235528_20170201T235555_015097_018AE8_4BF3
S1A_IW_SLC__1SDV_20170201T235553_20170201T235620_015097_018AE8_0CF1
S1A_IW_SLC__1SDV_20170225T235531_20170225T235558_015447_0195C3_B0AE
S1A_IW_SLC__1SDV_20170309T235531_20170309T235558_015622_019B0F_B2C5
S1A_IW_SLC__1SDV_20170321T235524_20170321T235551_015797_01A044_2D23
S1A_IW_SLC__1SDV_20170321T235549_20170321T235616_015797_01A044_AD43
S1A_IW_SLC__1SDV_20170402T235525_20170402T235552_015972_01A572_00F3
S1A_IW_SLC__1SDV_20170402T235549_20170402T235616_015972_01A572_992C
S1A_IW_SLC__1SDV_20170414T235525_20170414T235552_016147_01AACB_547C
S1A_IW_SLC__1SDV_20170414T235550_20170414T235617_016147_01AACB_13E9
S1A_IW_SLC__1SDV_20170426T235525_20170426T235552_016322_01B021_2E81
S1A_IW_SLC__1SDV_20170426T235550_20170426T235617_016322_01B021_7E02
S1A_IW_SLC__1SDV_20170508T235526_20170508T235553_016497_01B575_5C45
S1A_IW_SLC__1SDV_20170508T235551_20170508T235618_016497_01B575_76BA
S1A_IW_SLC__1SDV_20170520T235527_20170520T235554_016672_01BACE_7E91
S1A_IW_SLC__1SDV_20170520T235552_20170520T235619_016672_01BACE_6198
S1A_IW_SLC__1SDV_20170601T235528_20170601T235555_016847_01C031_1AD0
S1A_IW_SLC__1SDV_20170601T235552_20170601T235619_016847_01C031_6EC0
S1A_IW_SLC__1SDV_20170731T235531_20170731T235558_017722_01DAEC_8ECD
S1A_IW_SLC__1SDV_20170731T235556_20170731T235623_017722_01DAEC_BC55
S1A_IW_SLC__1SDV_20170812T235532_20170812T235559_017897_01E03B_7BF4
S1A_IW_SLC__1SDV_20170812T235556_20170812T235624_017897_01E03B_C961
S1A_IW_SLC__1SDV_20170824T235532_20170824T235559_018072_01E586_27C2
S1A_IW_SLC__1SDV_20170824T235557_20170824T235624_018072_01E586_6B60
S1A_IW_SLC__1SDV_20170905T235533_20170905T235600_018247_01EAD9_6A53
S1A_IW_SLC__1SDV_20170905T235557_20170905T235625_018247_01EAD9_E6E0
S1A_IW_SLC__1SDV_20170917T235533_20170917T235600_018422_01F04D_6BB5
S1A_IW_SLC__1SDV_20170917T235558_20170917T235625_018422_01F04D_E95C
S1A_IW_SLC__1SDV_20170929T235533_20170929T235601_018597_01F5A4_7C8B
S1A_IW_SLC__1SDV_20170929T235558_20170929T235625_018597_01F5A4_7C21
S1A_IW_SLC__1SDV_20171011T235534_20171011T235601_018772_01FAF6_C9EB
S1A_IW_SLC__1SDV_20171011T235558_20171011T235626_018772_01FAF6_3ACA
S1A_IW_SLC__1SDV_20171023T235534_20171023T235601_018947_020056_F588
S1A_IW_SLC__1SDV_20171023T235559_20171023T235626_018947_020056_346F

S1A_IW_SLC__1SDV_20171104T235534_20171104T235601_019122_0205AC_5241
S1A_IW_SLC__1SDV_20171104T235558_20171104T235626_019122_0205AC_472A
S1A_IW_SLC__1SDV_20171116T235533_20171116T235600_019297_020B23_C089
S1A_IW_SLC__1SDV_20171116T235558_20171116T235625_019297_020B23_DE86
S1A_IW_SLC__1SDV_20171128T235533_20171128T235600_019472_0210AA_359C
S1A_IW_SLC__1SDV_20171128T235558_20171128T235625_019472_0210AA_99B1
S1A_IW_SLC__1SDV_20171210T235533_20171210T235600_019647_021620_6652
S1A_IW_SLC__1SDV_20171210T235557_20171210T235625_019647_021620_6CF7
S1A_IW_SLC__1SDV_20171222T235532_20171222T235559_019822_021B82_C9CF
S1A_IW_SLC__1SDV_20171222T235557_20171222T235624_019822_021B82_B5BC
S1A_IW_SLC__1SDV_20180103T235531_20180103T235559_019997_022104_00F5
S1A_IW_SLC__1SDV_20180103T235556_20180103T235623_019997_022104_DB50
S1A_IW_SLC__1SDV_20180115T235531_20180115T235558_020172_022695_10B6
S1A_IW_SLC__1SDV_20180115T235556_20180115T235623_020172_022695_AA91
S1A_IW_SLC__1SDV_20180127T235531_20180127T235558_020347_022C20_B1D4
S1A_IW_SLC__1SDV_20180127T235556_20180127T235623_020347_022C20_FB07
S1A_IW_SLC__1SDV_20180208T235531_20180208T235558_020522_0231B8_E9B9
S1A_IW_SLC__1SDV_20180208T235556_20180208T235623_020522_0231B8_3F2E
S1A_IW_SLC__1SDV_20180220T235530_20180220T235557_020697_023749_B314
S1A_IW_SLC__1SDV_20180220T235555_20180220T235622_020697_023749_BCAD
S1A_IW_SLC__1SDV_20180304T235530_20180304T235557_020872_023CD2_E827
S1A_IW_SLC__1SDV_20180304T235555_20180304T235622_020872_023CD2_4558
S1A_IW_SLC__1SDV_20180316T235531_20180316T235558_021047_024260_3EA3
S1A_IW_SLC__1SDV_20180316T235555_20180316T235622_021047_024260_8DE5
S1A_IW_SLC__1SDV_20180328T235531_20180328T235558_021222_0247EE_1C16
S1A_IW_SLC__1SDV_20180328T235556_20180328T235623_021222_0247EE_905E
S1A_IW_SLC__1SDV_20180409T235531_20180409T235558_021397_024D6E_5EF3
S1A_IW_SLC__1SDV_20180409T235556_20180409T235623_021397_024D6E_EF65
S1A_IW_SLC__1SDV_20180421T235532_20180421T235559_021572_0252DF_F2FD
S1A_IW_SLC__1SDV_20180421T235556_20180421T235624_021572_0252DF_6606
S1A_IW_SLC__1SDV_20180503T235532_20180503T235559_021747_02585F_F993
S1A_IW_SLC__1SDV_20180503T235557_20180503T235624_021747_02585F_B3B1
S1A_IW_SLC__1SDV_20180515T235533_20180515T235600_021922_025DFC_519E
S1A_IW_SLC__1SDV_20180515T235558_20180515T235625_021922_025DFC_9AD2
S1A_IW_SLC__1SDV_20180527T235534_20180527T235601_022097_02638A_8603
S1A_IW_SLC__1SDV_20180527T235558_20180527T235625_022097_02638A_95F7
S1A_IW_SLC__1SDV_20180608T235534_20180608T235601_022272_026907_0EEB
S1A_IW_SLC__1SDV_20180608T235559_20180608T235626_022272_026907_10A3
S1A_IW_SLC__1SDV_20180714T235536_20180714T235603_022797_0278AA_2EB6
S1A_IW_SLC__1SDV_20180714T235601_20180714T235628_022797_0278AA_12E8
S1A_IW_SLC__1SDV_20180726T235537_20180726T235604_022972_027E33_0920

S1A_IW_SLC__1SDV_20180726T235602_20180726T235629_022972_027E33_EC23
S1A_IW_SLC__1SDV_20180807T235538_20180807T235605_023147_0283AC_5422
S1A_IW_SLC__1SDV_20180807T235603_20180807T235630_023147_0283AC_F0A5
S1A_IW_SLC__1SDV_20180819T235538_20180819T235606_023322_028959_5659
S1A_IW_SLC__1SDV_20180819T235603_20180819T235630_023322_028959_796F
S1A_IW_SLC__1SDV_20180831T235539_20180831T235606_023497_028EE7_ADFE
S1A_IW_SLC__1SDV_20180831T235604_20180831T235631_023497_028EE7_24DD
S1A_IW_SLC__1SDV_20180912T235540_20180912T235607_023672_02947F_3C60
S1A_IW_SLC__1SDV_20180912T235604_20180912T235631_023672_02947F_0912
S1A_IW_SLC__1SDV_20180924T235540_20180924T235607_023847_029A32_847A
S1A_IW_SLC__1SDV_20180924T235605_20180924T235632_023847_029A32_0C6B
S1A_IW_SLC__1SDV_20181006T235540_20181006T235607_024022_029FEB_6F73
S1A_IW_SLC__1SDV_20181006T235605_20181006T235632_024022_029FEB_02A9
S1A_IW_SLC__1SDV_20181018T235540_20181018T235608_024197_02A59F_6EBB
S1A_IW_SLC__1SDV_20181018T235605_20181018T235632_024197_02A59F_2825
S1A_IW_SLC__1SDV_20181030T235540_20181030T235607_024372_02AB43_DBD0
S1A_IW_SLC__1SDV_20181030T235605_20181030T235632_024372_02AB43_2052
S1A_IW_SLC__1SDV_20181111T235540_20181111T235607_024547_02B19F_2D4C
S1A_IW_SLC__1SDV_20181111T235605_20181111T235632_024547_02B19F_4583
S1A_IW_SLC__1SDV_20181123T235540_20181123T235607_024722_02B811_BB6F
S1A_IW_SLC__1SDV_20181123T235605_20181123T235632_024722_02B811_0A84
S1A_IW_SLC__1SDV_20181217T235539_20181217T235606_025072_02C446_6D03
S1A_IW_SLC__1SDV_20181217T235604_20181217T235631_025072_02C446_FE20
S1A_IW_SLC__1SDV_20181229T235539_20181229T235606_025247_02CAA0_D8B6
S1A_IW_SLC__1SDV_20181229T235603_20181229T235630_025247_02CAA0_5DE8
S1A_IW_SLC__1SDV_20190110T235538_20190110T235605_025422_02D0E9_20D1
S1A_IW_SLC__1SDV_20190110T235603_20190110T235630_025422_02D0E9_6482
S1A_IW_SLC__1SDV_20190122T235538_20190122T235605_025597_02D74F_AA50
S1A_IW_SLC__1SDV_20190122T235603_20190122T235630_025597_02D74F_CB2A
S1A_IW_SLC__1SDV_20190203T235537_20190203T235604_025772_02DDAA_E09E
S1A_IW_SLC__1SDV_20190203T235602_20190203T235629_025772_02DDAA_BF65
S1A_IW_SLC__1SDV_20190215T235537_20190215T235604_025947_02E3DD_8768
S1A_IW_SLC__1SDV_20190215T235602_20190215T235629_025947_02E3DD_2230
S1A_IW_SLC__1SDV_20190227T235537_20190227T235604_026122_02EA16_754C
S1A_IW_SLC__1SDV_20190227T235602_20190227T235629_026122_02EA16_344C
S1A_IW_SLC__1SDV_20190311T235537_20190311T235604_026297_02F071_ACEF
S1A_IW_SLC__1SDV_20190311T235602_20190311T235629_026297_02F071_A7C3
S1A_IW_SLC__1SDV_20190323T235537_20190323T235604_026472_02F6E8_B0AB
S1A_IW_SLC__1SDV_20190323T235602_20190323T235629_026472_02F6E8_C7A2
S1A_IW_SLC__1SDV_20190404T235537_20190404T235604_026647_02FD61_7474
S1A_IW_SLC__1SDV_20190404T235602_20190404T235629_026647_02FD61_0D75

S1A_IW_SLC__1SDV_20190416T235538_20190416T235605_026822_0303BE_9B60
S1A_IW_SLC__1SDV_20190416T235603_20190416T235630_026822_0303BE_FD64
S1A_IW_SLC__1SDV_20190428T235538_20190428T235605_026997_030A0E_9826
S1A_IW_SLC__1SDV_20190428T235603_20190428T235630_026997_030A0E_71B0
S1A_IW_SLC__1SDV_20190510T235539_20190510T235606_027172_031023_6717
S1A_IW_SLC__1SDV_20190510T235603_20190510T235631_027172_031023_B369
S1A_IW_SLC__1SDV_20190522T235604_20190522T235631_027347_03159F_656C
S1A_IW_SLC__1SDV_20190603T235540_20190603T235607_027522_031B0C_D45C
S1A_IW_SLC__1SDV_20190603T235605_20190603T235632_027522_031B0C_0E08
S1A_IW_SLC__1SDV_20190615T235540_20190615T235608_027697_032055_A465
S1A_IW_SLC__1SDV_20190615T235605_20190615T235632_027697_032055_B4A2
S1A_IW_SLC__1SDV_20190627T235541_20190627T235608_027872_03258C_1FCA
S1A_IW_SLC__1SDV_20190627T235606_20190627T235633_027872_03258C_E519
S1A_IW_SLC__1SDV_20190709T235542_20190709T235609_028047_032AE1_0264
S1A_IW_SLC__1SDV_20190709T235607_20190709T235634_028047_032AE1_824D
S1A_IW_SLC__1SDV_20190721T235543_20190721T235610_028222_033027_A32E
S1A_IW_SLC__1SDV_20190721T235608_20190721T235635_028222_033027_8101
S1A_IW_SLC__1SDV_20190802T235544_20190802T235611_028397_03357D_F66A
S1A_IW_SLC__1SDV_20190802T235608_20190802T235636_028397_03357D_725B
S1A_IW_SLC__1SDV_20190826T235545_20190826T235612_028747_03414E_D125
S1A_IW_SLC__1SDV_20190826T235610_20190826T235637_028747_03414E_9533
S1A_IW_SLC__1SDV_20190907T235546_20190907T235613_028922_034767_56DE
S1A_IW_SLC__1SDV_20190907T235610_20190907T235638_028922_034767_D1FF
S1A_IW_SLC__1SDV_20190919T235546_20190919T235613_029097_034D72_7BDC
S1A_IW_SLC__1SDV_20190919T235611_20190919T235638_029097_034D72_7397
S1A_IW_SLC__1SDV_20191001T235547_20191001T235614_029272_035378_C182
S1A_IW_SLC__1SDV_20191001T235611_20191001T235639_029272_035378_8DF3
S1A_IW_SLC__1SDV_20191013T235547_20191013T235614_029447_03597F_0EC5
S1A_IW_SLC__1SDV_20191013T235611_20191013T235638_029447_03597F_D86F
S1A_IW_SLC__1SDV_20191025T235547_20191025T235614_029622_035F7E_CD3E
S1A_IW_SLC__1SDV_20191025T235611_20191025T235638_029622_035F7E_4762
S1A_IW_SLC__1SDV_20191106T235547_20191106T235614_029797_0365AF_0A7F
S1A_IW_SLC__1SDV_20191106T235611_20191106T235639_029797_0365AF_DDB9
S1A_IW_SLC__1SDV_20191118T235546_20191118T235614_029972_036BC0_6597
S1A_IW_SLC__1SDV_20191118T235611_20191118T235638_029972_036BC0_69B0
S1A_IW_SLC__1SDV_20191130T235546_20191130T235613_030147_0371D0_AEE1
S1A_IW_SLC__1SDV_20191130T235611_20191130T235638_030147_0371D0_0EE6
S1A_IW_SLC__1SDV_20191212T235610_20191212T235637_030322_0377DC_A727
S1A_IW_SLC__1SDV_20191224T235610_20191224T235637_030497_037DE8_42E1
S1A_IW_SLC__1SSV_20150916T235534_20150916T235601_007747_00AC4E_D0B9
S1B_IW_SLC__1SDV_20190504T235513_20190504T235543_016101_01E49E_CBB0

Ascending Sentinel-1 scenes for InSAR analyses

S1A_IW_SLC__1SSV_20141025T120356_20141025T120424_002986_003658_DC50
S1A_IW_SLC__1SSV_20141118T120356_20141118T120424_003336_003DDF_E74E
S1A_IW_SLC__1SSV_20141212T120355_20141212T120423_003686_0045F2_FE49
S1A_IW_SLC__1SSV_20150105T120354_20150105T120422_004036_004DD9_398B
S1A_IW_SLC__1SSV_20150129T120353_20150129T120421_004386_0055A6_B4EA
S1A_IW_SLC__1SSV_20150222T120353_20150222T120421_004736_005DC5_A383
S1A_IW_SLC__1SSV_20150318T120353_20150318T120421_005086_006644_437F
S1A_IW_SLC__1SSV_20150411T120354_20150411T120422_005436_006EC8_7864
S1A_IW_SLC__1SSV_20150529T120357_20150529T120424_006136_007F72_4D82
S1A_IW_SLC__1SSV_20150622T120347_20150622T120417_006486_00899A_8350
S1A_IW_SLC__1SSV_20150716T120348_20150716T120418_006836_009359_AE44
S1A_IW_SLC__1SSV_20150809T120349_20150809T120419_007186_009D11_5734
S1A_IW_SLC__1SSV_20150902T120350_20150902T120420_007536_00A6A1_4D37
S1A_IW_SLC__1SSV_20150914T120351_20150914T120420_007711_00AB50_798D
S1A_IW_SLC__1SSV_20150926T120351_20150926T120421_007886_00B001_DA4A
S1A_IW_SLC__1SSV_20151020T120351_20151020T120421_008236_00B984_602E
S1A_IW_SLC__1SSV_20151113T120413_20151113T120440_008586_00C2D9_E798
S1A_IW_SLC__1SSV_20151207T120412_20151207T120440_008936_00CCB5_6803
S1A_IW_SLC__1SSV_20151231T120411_20151231T120439_009286_00D687_412D
S1A_IW_SLC__1SSV_20160217T120410_20160217T120438_009986_00EAD5_A960
S1A_IW_SLC__1SSV_20160312T120410_20160312T120438_010336_00F4E4_3997
S1A_IW_SLC__1SSV_20160405T120411_20160405T120439_010686_00FEDE_FBC6
S1A_IW_SLC__1SSV_20160429T120412_20160429T120440_011036_010995_6600
S1A_IW_SLC__1SSV_20160523T120413_20160523T120441_011386_0114D5_3E67
S1A_IW_SLC__1SDV_20160604T120400_20160604T120425_011561_011A73_6686
S1A_IW_SLC__1SSV_20160803T120418_20160803T120446_012436_0136AE_2276
S1A_IW_SLC__1SSV_20160827T120419_20160827T120447_012786_014257_E98A
S1A_IW_SLC__1SSV_20160920T120420_20160920T120447_013136_014DD6_E54A
S1A_IW_SLC__1SSV_20161014T120420_20161014T120448_013486_0158F9_6B9B
S1A_IW_SLC__1SSV_20161107T120420_20161107T120448_013836_0163E0_EAD0
S1A_IW_SLC__1SSV_20161201T120419_20161201T120447_014186_016EB0_2C58
S1A_IW_SLC__1SSV_20161225T120418_20161225T120446_014536_0179B2_DC49
S1A_IW_SLC__1SSV_20170118T120416_20170118T120444_014886_018479_18F2
S1A_IW_SLC__1SSV_20170211T120416_20170211T120444_015236_018F45_977B
S1A_IW_SLC__1SDV_20170223T120416_20170223T120444_015411_0194AE_2614
S1A_IW_SLC__1SDV_20170307T120416_20170307T120444_015586_0199F9_F15F
S1A_IW_SLC__1SDV_20170319T120401_20170319T120427_015761_019F2B_09B2
S1A_IW_SLC__1SDV_20170331T120401_20170331T120428_015936_01A461_982E
S1A_IW_SLC__1SDV_20170412T120401_20170412T120428_016111_01A9AE_E705
S1A_IW_SLC__1SDV_20170424T120402_20170424T120429_016286_01AF0F_9832

S1A_IW_SLC__1SDV_20170506T120403_20170506T120430_016461_01B453_D99A
S1A_IW_SLC__1SDV_20170518T120403_20170518T120430_016636_01B9AB_57BF
S1A_IW_SLC__1SDV_20170530T120404_20170530T120431_016811_01BF0F_9B44
S1B_IW_SLC__1SDV_20170605T120333_20170605T120354_005915_00A5F6_834E
S1A_IW_SLC__1SDV_20170611T120405_20170611T120432_016986_01C47D_B7DE
S1A_IW_SLC__1SDV_20170623T120405_20170623T120432_017161_01C9D6_89CC
S1A_IW_SLC__1SDV_20170705T120406_20170705T120433_017336_01CF21_3926
S1A_IW_SLC__1SDV_20170717T120407_20170717T120434_017511_01D472_0B09
S1A_IW_SLC__1SDV_20170729T120407_20170729T120434_017686_01D9CD_3B78
S1A_IW_SLC__1SDV_20170810T120408_20170810T120435_017861_01DF21_3CEE
S1A_IW_SLC__1SDV_20170822T120409_20170822T120436_018036_01E472_E062
S1A_IW_SLC__1SDV_20170903T120409_20170903T120436_018211_01E9B7_897D
S1A_IW_SLC__1SDV_20170915T120410_20170915T120436_018386_01EF2B_7F53
S1A_IW_SLC__1SDV_20170927T120410_20170927T120437_018561_01F486_5E01
S1A_IW_SLC__1SDV_20171009T120410_20171009T120437_018736_01F9D6_21DA
S1A_IW_SLC__1SDV_20171021T120410_20171021T120437_018911_01FF3B_958E
S1A_IW_SLC__1SDV_20171102T120410_20171102T120437_019086_02048A_137C
S1A_IW_SLC__1SDV_20171114T120410_20171114T120437_019261_0209FF_A58A
S1A_IW_SLC__1SDV_20171126T120410_20171126T120437_019436_020F89_F124
S1A_IW_SLC__1SDV_20171208T120409_20171208T120436_019611_0214FC_4E43
S1A_IW_SLC__1SDV_20171220T120409_20171220T120436_019786_021A70_4DC4
S1A_IW_SLC__1SDV_20180101T120408_20180101T120435_019961_021FE1_7335
S1A_IW_SLC__1SDV_20180113T120408_20180113T120435_020136_022569_A56A
S1A_IW_SLC__1SDV_20180125T120407_20180125T120434_020311_022AF6_E636
S1A_IW_SLC__1SDV_20180206T120407_20180206T120434_020486_02308C_3DCD
S1A_IW_SLC__1SDV_20180218T120407_20180218T120434_020661_023622_A0BB
S1A_IW_SLC__1SDV_20180302T120407_20180302T120434_020836_023BAE_47A7
S1A_IW_SLC__1SDV_20180314T120407_20180314T120434_021011_02413B_F032
S1A_IW_SLC__1SDV_20180326T120407_20180326T120434_021186_0246CB_B6C6
S1A_IW_SLC__1SDV_20180407T120407_20180407T120434_021361_024C46_60AE
S1A_IW_SLC__1SDV_20180419T120408_20180419T120435_021536_0251BB_F4DE
S1A_IW_SLC__1SDV_20180501T120408_20180501T120435_021711_02573C_3055
S1A_IW_SLC__1SDV_20180513T120409_20180513T120436_021886_025CD7_4F3C
S1A_IW_SLC__1SDV_20180525T120410_20180525T120437_022061_02625F_1C03
S1A_IW_SLC__1SDV_20180606T120410_20180606T120437_022236_0267DF_6356
S1A_IW_SLC__1SDV_20180618T120411_20180618T120438_022411_026D46_66BB
S1A_IW_SLC__1SDV_20180630T120412_20180630T120439_022586_02725D_DBBE
S1A_IW_SLC__1SDV_20180712T120413_20180712T120440_022761_02778E_1AD6
S1A_IW_SLC__1SDV_20180724T120413_20180724T120440_022936_027D11_FAF0
S1A_IW_SLC__1SDV_20180805T120414_20180805T120441_023111_028289_C248
S1A_IW_SLC__1SDV_20180817T120415_20180817T120442_023286_028835_6AB4

S1A_IW_SLC__1SDV_20180829T120416_20180829T120443_023461_028DC3_C5A2
S1A_IW_SLC__1SDV_20180910T120416_20180910T120443_023636_02935F_DB01
S1A_IW_SLC__1SDV_20180922T120416_20180922T120443_023811_02990F_7A61
S1A_IW_SLC__1SDV_20181004T120416_20181004T120443_023986_029EC8_3E96
S1A_IW_SLC__1SDV_20181016T120417_20181016T120444_024161_02A47A_A5E7
S1A_IW_SLC__1SDV_20181028T120417_20181028T120444_024336_02AA1D_92F0
S1A_IW_SLC__1SDV_20181109T120417_20181109T120443_024511_02B04D_6567
S1A_IW_SLC__1SDV_20181121T120416_20181121T120443_024686_02B6BF_B0A2
S1A_IW_SLC__1SDV_20181203T120416_20181203T120443_024861_02BCD8_ECEB
S1A_IW_SLC__1SDV_20181215T120415_20181215T120442_025036_02C2FF_93CD
S1A_IW_SLC__1SDV_20181227T120415_20181227T120442_025211_02C956_696A
S1A_IW_SLC__1SDV_20190108T120414_20190108T120441_025386_02CFA8_7D0D
S1A_IW_SLC__1SDV_20190120T120414_20190120T120441_025561_02D602_9704
S1A_IW_SLC__1SDV_20190201T120414_20190201T120441_025736_02DC62_021C
S1A_IW_SLC__1SDV_20190213T120413_20190213T120440_025911_02E292_BD08
S1A_IW_SLC__1SDV_20190225T120413_20190225T120440_026086_02E8D9_02A3
S1A_IW_SLC__1SDV_20190309T120413_20190309T120440_026261_02EF29_A576
S1A_IW_SLC__1SDV_20190321T120413_20190321T120440_026436_02F598_B734
S1A_IW_SLC__1SDV_20190402T120414_20190402T120441_026611_02FC10_0EA6
S1A_IW_SLC__1SDV_20190414T120414_20190414T120441_026786_030276_E623
S1A_IW_SLC__1SDV_20190426T120415_20190426T120442_026961_0308C7_5030
S1A_IW_SLC__1SDV_20190508T120415_20190508T120442_027136_030F08_4CA8
S1A_IW_SLC__1SDV_20190520T120416_20190520T120443_027311_031480_2A1C
S1A_IW_SLC__1SDV_20190601T120416_20190601T120443_027486_0319F2_B66E
S1A_IW_SLC__1SDV_20190613T120417_20190613T120444_027661_031F43_E989
S1A_IW_SLC__1SDV_20190625T120418_20190625T120445_027836_03247A_3E0C
S1A_IW_SLC__1SDV_20190707T120418_20190707T120445_028011_0329CD_13EC
S1A_IW_SLC__1SDV_20190719T120419_20190719T120446_028186_032F14_6D40
S1B_IW_SLC__1SDV_20190725T120356_20190725T120426_017290_020841_D34F
S1A_IW_SLC__1SDV_20190731T120420_20190731T120447_028361_03346D_3D1E
S1A_IW_SLC__1SDV_20190812T120421_20190812T120448_028536_033A08_9BBE
S1A_IW_SLC__1SDV_20190824T120421_20190824T120448_028711_034010_1952
S1A_IW_SLC__1SDV_20190905T120422_20190905T120449_028886_03462C_B5FD
S1A_IW_SLC__1SDV_20190929T120423_20190929T120450_029236_035242_2DC8
S1A_IW_SLC__1SDV_20191011T120423_20191011T120450_029411_035844_9D7A
S1A_IW_SLC__1SDV_20191023T120423_20191023T120450_029586_035E44_C549
S1A_IW_SLC__1SDV_20191104T120423_20191104T120450_029761_036465_C31D
S1A_IW_SLC__1SDV_20191116T120423_20191116T120450_029936_036A8A_7DAC
S1A_IW_SLC__1SDV_20191128T120423_20191128T120449_030111_03709C_118E
S1A_IW_SLC__1SDV_20191210T120422_20191210T120449_030286_0376A1_FF67
S1A_IW_SLC__1SDV_20191222T120422_20191222T120449_030461_037CAA_AC06

Annexure D: SARscape processing parameters

SBAS processing parameters from parameters.sml file generated by ENVI SARscape:

**Parameter settings used for the process **

Min Normal Baseline is 0.000000 ** Max Normal Baseline is 2.000000 ** Min Temporal Baseline is 0 ** Max Temporal Baseline is 90 ** Redundancy is high ** Criteria is min_normal ** Only Forward Pairs is FALSE ** Allow Disconnected Blocks is TRUE ** Delaunay 3D is FALSE

Initialization From Orbit is TRUE ** Estimate From Amplitude is TRUE ** Estimate From Coherence is TRUE ** Range Looks is 4 ** Azimuth Looks is 1 ** Range Dependency is 3 ** Azimuth Dependency is 3 ** Range Res Dependency is 2 ** Azimuth Res Dependency is 1 ** Range Window Number is 12 ** Azimuth Window Number is 3 ** Range Window Size is 256 ** Azimuth Window Size is 128 ** Cross Correlation Threshold is 0.250000 ** Fine Range Window Number is 25 ** Fine Azimuth Window Number is 8 ** Fine Range Window Size is 32 ** Fine Azimuth Window Size is 32 ** SNR Threshold is 3.200000 ** Coregistration with DEM is TRUE

Spectral Shift Filter is TRUE ** Doppler Filter is FALSE ** Range Looks is 4 ** Azimuth Looks is 1

Orbit Interpolation is 100 ** Optimal Resolution Approach is TRUE ** Window Size Mean Filter size is 5 ** Window Size Interpolation is 11 ** DEM Resampling Factor is -1.000000

Goldstein filter ** Interferogram Window Size is 64 ** Window Overlap Percentage is 80.000000 ** Low Pass Percentage is 5.000000 ** Intensity Window Size is 5 ** Alpha Min Value is 0.300000 ** Alpha Max Value is 2.500000 ** Coherence from Fint is TRUE ** Coherence Rg Window Size is 5 ** Coherence Az Window Size is 5 ** Low Frequency Removal Rg is 0 ** Low Frequency Removal Az is 0

EMPTY

Unwrapping Method is MCF_DELAUNAY ** Unwrapping Coherence Threshold is 0.300000 ** Decomposition Levels is 1 ** Range Scale Factor Decomposition is 3 ** Azimuth Scale Factor Decomposition is 3 ** Use 3D Unwrapping FALSE ** 3D Velocity Step Nr is 200 ** 3D Height Step Nr is 200 ** 3D Velocity Step Size is 5.000000 ** 3D Height Step Size is 10.000000 ** 3D Interferogram Valid Percentage is 60.000000 ** Tile Size in Range is 800 ** Tile Size in Azimuth is 800 ** Range Overlap is 300 ** Azimuth Overlap is 200 ** Minimum Cost Coherence is -1.000000

** Refinement Method is RemoveResidualPhase ** Residual Phase Poly Degree is 3

Estimate residual height is OK ** Displacement model type is linear ** Weighted Solution is TRUE ** Inversion SVD type is jacobi ** Min Valid Interf Percentage is 60.000000% ** Interpolate Disconnected Blocks is TRUE ** Reject outliars H [m] is -1.000000% ** Reject outliars D [mm] is -1.000000% ** Coherence Threshold is 0.300000 ** Wavelet LP size is 1200.000000

Unwrapping Method is MCF_DELAUNAY ** Unwrapping Coherence Threshold is 0.200000 ** Decomposition Levels is 1 ** Range Scale Factor Decomposition is 3 ** Azimuth Scale Factor Decomposition is 3 ** Use 3D Unwrapping FALSE ** 3D Velocity Step Nr is 200 ** 3D Height Step Nr is 200 ** 3D Velocity Step Size is 5.000000 ** 3D Height Step Size is 10.000000 ** 3D Interferogram Valid Percentage is 60.000000 ** Tile Size in Range is 800 ** Tile Size in Azimuth is 800 ** Range Overlap is 300 ** Azimuth Overlap is 200 ** Minimum Cost Coherence is -1.000000

Refinement Method is RemoveResidualPhase ** Residual Phase Poly Degree is 3

Refinement poly degree is 3 ** Estimate residual height is OK ** Displacement model type is linear ** Weighted Solution is TRUE ** Inversion SVD type is jacobi ** Min Valid Interf Percentage is 60.000000% ** Interpolate Disconnected Blocks is TRUE ** Min Valid Image Percentage is 80.000000% ** Reject outliars H [m] is -1.000000% ** Reject outliars D [mm] is -1.000000% ** Coherence Threshold is 0.300000

Refinement poly degree is 3 ** Atmosphere Low Pass Size is 1200.000000 ** Atmosphere High Pass Size is 365.000000

X Dimension is 15.000000 ** Y Dimension is 15.000000 ** Precision Height threshold is 5.000000 ** Precision Velocity threshold is 8.000000 ** Temporal coherence threshold is 0.100000 ** Water body mask threshold [dB] is -10.000000 ** Generate results in raster format is TRUE ** Generate results in shape format is TRUE ** Add time series in shape is TRUE ** Max number of points in shape is 200000 ** Interpolation Window Size is 3 ** Mean Window Size is 3 ** Generate Vertical Direction Results is FALSE ** Generate Max Slope Direction Results is FALSE ** Max Slope Direction Files is NotOK ** Generate User Direction Results is FALSE ** Azimuth Angle is 0.000000 ** Inclination Angle is 0.000000

PSI processing parameters from parameters.sml file generated by ENVI SARscape:

**This Tool Implemet the PS Module ** First Version 10.02.2011 AC ** Copyright by Sarmap SA ** Based on F.Rocca, A.Ferretti ** A New Algorithm for Surface Deformation Monitoring Based on persistent scatterers **

Initialization From Orbit is TRUE ** Orbit Accuracy is TRUE ** Estimate From Amplitude is TRUE ** Estimate From Coherence is TRUE ** Range Dependency is 3 ** Azimuth Dependency is 3 ** Range Window Number is 12 ** Azimuth Window Number is 3 ** Range Window Size is 256 ** Azimuth Window Size is 128 ** Cross Correlation Threshold is 0.250000 ** Fine Range Window Number is 25 ** Fine Azimuth Window Number is 8 ** Fine Range Window Size is 32 ** Fine Azimuth Window Size is 32 ** SNR Threshold is 3.200000

Range Looks is -2 ** Azimuth Looks is 1 ** spectral Shift Filter is FALSE ** Doppler Filter is FALSE

Sub-Area size(sqkm) is 25.000000 ** Overlap(%) is 30 ** Coherence used for Merging all Sub-Areas is 0.660000 ** min velocity[mm/year] is -100.000000 ** max velocity[mm/year] is 100.000000 ** sampling rate velocity[mm/year] is 1.000000 ** min height[m] is -70.000000 ** max height[m] is 70.000000 ** sampling rate height[m] is 2.000000

Low Pass Filter Size[m] is 1200.000000 ** High Pass Filter Size[days] is 365.000000 ** min velocity[mm/year] is -100.000000 ** max velocity[mm/year] is 100.000000 ** sampling rate velocity[mm/year] is 1.000000 ** min height[m] is -70.000000 ** max height[m] is 70.000000 ** sampling rate height[m] is 2.000000

Coherence Threshold is 0.700000 ** Geocode using Mu/Sigma Threshold is FALSE ** Mu/Sigma Threshold is 0.000000 ** Water Body Mask is 0.000000 ** Refinement GCP File Is NotOK ** Geocoded Shape Products is TRUE ** Geocoded Raster Products is TRUE ** X Dimension is 15.000000 ** Y Dimension is 15.000000